

DISSERTATION

**INVESTIGATING CAUSES OF REGIONAL
VARIATIONS IN ATMOSPHERIC CO₂
CONCENTRATIONS**

Submitted by

Katherine D. Corbin

Department of Atmospheric Science

In partial fulfillment of the requirements

For the Degree of Doctor of Philosophy

Colorado State University

Fort Collins, Colorado

Summer 2008

UMI Number: 3332706

INFORMATION TO USERS

The quality of this reproduction is dependent upon the quality of the copy submitted. Broken or indistinct print, colored or poor quality illustrations and photographs, print bleed-through, substandard margins, and improper alignment can adversely affect reproduction.

In the unlikely event that the author did not send a complete manuscript and there are missing pages, these will be noted. Also, if unauthorized copyright material had to be removed, a note will indicate the deletion.

UMI[®]

UMI Microform 3332706

Copyright 2008 by ProQuest LLC.

All rights reserved. This microform edition is protected against unauthorized copying under Title 17, United States Code.

ProQuest LLC
789 E. Eisenhower Parkway
PO Box 1346
Ann Arbor, MI 48106-1346

COLORADO STATE UNIVERSITY

June 13, 2008

WE HEREBY RECOMMEND THAT THIS DISSERTATION PREPARED UNDER OUR SUPERVISION BY KATHERINE D. CORBIN ENTITLED INVESTIGATING CAUSES OF REGIONAL VARIATIONS IN ATMOSPHERIC CO₂ CONCENTRATIONS BE ACCEPTED AS FULFILLING IN PART REQUIREMENTS FOR THE DEGREE OF DOCTOR OF PHILOSOPHY.

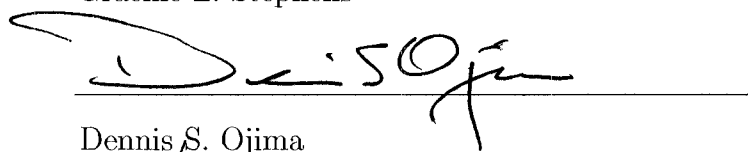
Committee on Graduate Work



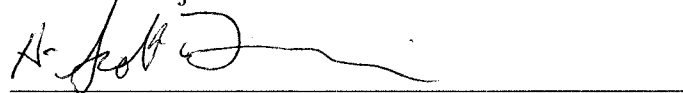
Sonia M. Kreidenweis



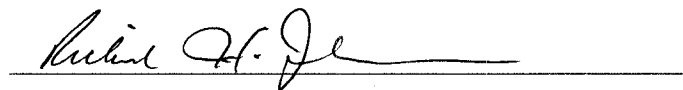
Graeme L. Stephens



Dennis S. Ojima



A. Scott Denning, Adviser



Richard H. Johnson, Department Head

ABSTRACT OF DISSERTATION

INVESTIGATING CAUSES OF REGIONAL VARIATIONS IN
ATMOSPHERIC CO₂ CONCENTRATIONS

Atmospheric CO₂ concentrations are rapidly increasing due to anthropogenic activities; however, only about half of the emissions have accumulated in the atmosphere, and the fate of the remaining half remains uncertain. Since atmospheric CO₂ concentrations contain information regarding carbon sources and sinks, it is important to understand CO₂ variability. This study investigated causes of atmospheric CO₂ variability, focusing on the relationship between CO₂ concentrations and clouds, the impact of heterogeneous land cover and agricultural production, and the effect of redistributing fossil fuel emissions.

Due to global coverage and sheer data volume, satellite CO₂ concentrations will be used in inverse models to improve carbon source and sink estimates. Satellite concentrations will only retrieve CO₂ measurements in clear conditions, and it is important to understand how CO₂ concentrations vary with cloud cover in order to optimally utilize these data. This study evaluated differences between clear-sky and mean concentrations on local, regional, and global scales. Analyses of in situ data, regional model simulations, and global model output all revealed clear-sky differences that were regionally coherent on sub-continental scales and that varied both with time and location. In the mid-latitudes, clear-sky CO₂ concentrations were systematically lower than on average, and these differences were not due to biology, but rather to frontal convergence of large-scale gradients that were covered by clouds. Instead of using satellite data to represent temporal averages, inverse models and data assimilation systems that use satellite data to calculate carbon

sources and sinks must be sampled consistently with the observations, including precise modeling of winds, clouds, fronts, and frontal timing.

Just as CO₂ concentrations vary with cloud cover, variability in atmospheric CO₂ concentrations is also caused by heterogeneity in land cover and surface fluxes. This study focused on the impacts of land-cover heterogeneity and the effects of agricultural production on regional variations of atmospheric CO₂ concentrations. Including sub-grid scale land cover heterogeneity improved simulated atmospheric CO₂ concentrations by ~ 1 ppm. Implementing a crop-phenology model that explicitly simulated corn and soybeans into a coupled ecosystem-atmosphere model dramatically improved CO₂ fluxes and concentrations over the mid-continent, with reductions in CO₂ concentration root mean square errors of nearly 50% (over 10 ppm at some locations). Both the model and observations showed concentrations as low as 340 ppm over central Iowa, and a regional gradient of over 30 ppm in ~ 200 km occurred due to a combination of fluxes and meteorology. Since corn and soybeans have such a significant impact on both carbon fluxes and atmospheric concentrations, it is essential to model these crops accurately.

In addition to biological surface fluxes, surface emissions due to fossil fuel combustion also cause variability in regional atmospheric CO₂ concentrations. Using high-resolution fossil fuel emissions caused differences of over 10 ppm near the surface; and including temporal variability in the emissions impacted regional CO₂ concentrations on monthly timescales, causing seasonal differences of more than 20 ppm in some locations. Using coarse spatial distributions and unaccounting for temporal variability in fossil fuel emissions created biases in the atmospheric CO₂ concentrations and thus may cause significant errors in source and sink estimates from atmospheric inversions.

Katherine D. Corbin
Department of Atmospheric Science
Colorado State University
Fort Collins, CO 80523
Summer 2008

ACKNOWLEDGMENTS

I would like to thank my advisor, Scott Denning, for his tremendous help and guidance. His discussions and explanations were invaluable in helping me to put my research into perspective rather than focusing on the details of the model. My graduate committee, Kevin Gurney, Sonia Kreidenweis, Dennis Ojima, and Graeme Stephens, also deserve thanks.

Thanks to the members in the Denning Group. Ian Baker patiently explained SiB3 to me and pointed me in the right direction when I was at a loss to understand what was wrong. I am indebted to Erandi Lokupitiya for developing the crop phenology model used in this study. Help from Andrew Schuh and Lixin Lu was essential in running SiB3-RAMS.

I sincerely thank all the data providers, as without them this research would not be possible. Thank you to Ken Davis, Natasha Miles, Scott Richardson and Keith Paustian for the data collected during the Mid-Continent Intensive Campaign and during the Ring of Towers I. Thank you to Matt Hansen for providing the crop map. Thanks to all the principal investigators of the flux and CO₂ towers: Arlyn Andrews, Larry Flanagan, Doug Worthy, Sonia Wharton, Russ Monson, Shashi Verma, Margaret Torn, Marc Fischer, Ankur Desai, Gaby Katul, Ram Oren, William Munger, Stephen Wofsy, David Hollinger, and Roser Matamala.

Thanks also, of course, to my family and friends for their support throughout my time here in the Department of Atmospheric Science.

This research was funded by a NASA Earth System Science Fellowship 53-1970; NASA contracts NNG0SGD15G, NNX06AC75G, and NNG05GF41G; NASA subcontract 521-0438-01 from Purdue University; and the Department of Energy contract DE-FG02-06ER64317.

Contents

Abstract	iii
List of Figures	xix
List of Tables	xxi
1 Introduction	1
1.1 Why Study Atmospheric CO ₂ ?	1
1.2 The Global Carbon Cycle	2
1.3 Monitoring the Atmospheric CO ₂ Concentration	4
1.4 The Missing Carbon Sink and Atmospheric Inversions	8
1.5 Atmospheric CO ₂ Variability	10
1.6 Objectives	13
2 Using Continuous Data to Estimate Clear-Sky Errors in Inversions of Satellite CO₂ Measurements	16
2.1 Introduction	17
2.2 Methods	19
2.3 Results	23
2.4 Conclusions	27
3 Possible Representation Errors in Inversions of Satellite CO₂ Retrievals	29
3.1 Introduction	31
3.2 Methods	35
3.2.1 Model Description, SiB2-RAMS	35
3.2.2 Input Data	38
3.2.3 Case Descriptions	39
3.2.4 Model Evaluation	41

3.2.5	Simulating Satellite Measurements Using SiB2-RAMS Output	46
3.3	Results	47
3.3.1	Total Column CO ₂ Concentrations	47
3.3.2	Spatial Representation Errors	52
3.3.3	Local Clear-Sky Errors	55
3.3.4	Temporal Sampling Errors	58
3.4	Conclusions	63
4	Assessing Temporal Clear-Sky Errors in Assimilation of Satellite CO₂ Retrievals Using A Global Transport Model	67
4.1	Introduction	68
4.2	Model and Methods	70
4.3	Results	73
4.4	Conclusions	77
5	An Evaluation of SiB3-RAMS and an Analysis of the Impact of Sub-Grid Land Cover Heterogeneity	79
5.1	Introduction	80
5.2	Methods	84
5.2.1	Model Description SiB3-RAMS	84
5.2.2	Model Initialization and Input Data	87
5.2.3	Case Descriptions	90
5.2.4	Observations	93
5.2.5	Modeled Vegetation Cover at the Tower Sites	98
5.3	Results	100
5.3.1	NEE Tower Comparisons	100
5.3.2	CO ₂ Tower Comparisons	105
5.3.3	Distribution of the Net Ecosystem Exchange	107
5.3.4	CO ₂ Maps	113
5.3.5	Sources of Atmospheric CO ₂ Concentrations	116
5.4	Conclusions	119
6	Effects of Agricultural Production on Regional Variations of Atmospheric CO₂ Concentrations	123
6.1	Introduction	124
6.2	Methods	129
6.2.1	Model Description	129

6.2.2	Model Initialization and Input Data	130
6.2.3	Case Descriptions	133
6.2.4	Observations	138
6.3	Results	140
6.3.1	Impacts of the Crop Phenology Model on LAI, FPAR, and NEE	140
6.3.2	Distribution of the 2007 NEE	147
6.3.3	Analysis and Evaluation of Atmospheric CO ₂ Concentrations	148
6.4	Conclusions	163
7	A Preliminary Analysis on the Effects of Fossil Fuel Emissions on Regional Atmospheric CO₂ Concentrations	166
7.1	Introduction	167
7.2	Methods	169
7.2.1	Model Description, Initialization, and Input Data	169
7.2.2	Case Descriptions	170
7.2.3	Observations	171
7.3	Results	172
7.3.1	Evaluation of Atmospheric CO ₂ Concentrations	172
7.3.2	Annual Mean CO ₂ Distribution	176
7.3.3	Impacts of Spatial Redistribution	178
7.3.4	Impacts of Temporal Redistribution	180
7.4	Conclusions and Future Work	185
8	Conclusions and Recommendations	189
8.1	Conclusions	189
8.2	Recommendations for Future Work	194
	References	198

List of Figures

1.1	The global carbon cycle for the 1990s, showing the main annual fluxes in Gt C yr ⁻¹ : pre-industrial 'natural' fluxes in black and 'anthropogenic' fluxes in red. Atmospheric carbon content and all cumulative fluxes since 1750 are as of end 1994. From Denman et al. (2007).	3
1.2	Time series of atmospheric CO ₂ concentration at Mauna Loa, Hawaii, since 1958.	6
1.3	The global network of CO ₂ observations in 2007.	7
1.4	Variations of atmospheric CO ₂ concentration by time and latitude based on samples collected by the NOAA flask network.	11
2.1	The clear-sky CO ₂ sampling bias at WLEF (black) and at HF (gray), in ppm. Solid lines depict the 1100-1600 bias and dashed lines show the 1300 bias.	23
2.2	The NEE clear-sky bias, in $\mu\text{mol m}^2 \text{s}^{-1}$	24
2.3	PBL depth clear-sky bias, in m.	25
3.1	Grid setup over North America, with the nested grids outlined in red. The vegetation classifications for the coarse grid column (grid 3) and the fine grid column (grid 4) are shown in the bottom left and right images, respectively. The red cross indicates the location of the WLEF tower.	36

3.2 Grid setup in the South American simulation. The four grids in the simulation are outlined in red. The red cross displays the Tapajos Km 67 tower. 37

3.3 Observed (solid) and modeled (shaded, sampled from the grid cells including the towers) NEE, in $\mu\text{mol m}^{-2} \text{s}^{-1}$, versus radiation, in W m^{-2} . Evaluation at NA (top) and results from SA (bottom). For NA, the radiation includes longwave, and the values have been subtracted by 200 W m^{-2} for easier comparison. The SA radiation is shortwave only. A two-harmonic fit to each time series has been overlaid. Mean NA and SA model/data NEE values for radiation $> 650 \text{ W m}^{-2}$ are $-9.7/-10.1$ and $-13.8/-13.1 \mu\text{mol m}^{-2} \text{s}^{-1}$, respectively. For moderate radiation values between 300 and 650 W m^{-2} the resulting NA and SA model/data NEE means are $-8.5/-6.7$ and $-14.9/-7.3$, respectively. Finally, for radiation $< 300 \text{ W m}^{-2}$ the NA and SA model/data NEE mean values are $0.2/2.8$ and $-4.2/2.3 \mu\text{mol m}^{-2} \text{s}^{-1}$, respectively. 43

3.4	Observed (black) and modeled (grey, sampled from the grid cells including the towers) CO ₂ anomalies (ppm) versus radiation (W m ⁻²). NA results (top) and SA results (bottom). The anomalies are calculated by subtracting the mean CO ₂ concentration over each case from the corresponding series. Mean NA and SA model/data CO ₂ values for radiation > 650 W m ⁻² are -1.6/-1.1 and -4.3/-3.1 ppm, respectively. For moderate radiation values between 300 and 650 W m ⁻² the resulting NA and SA model/data CO ₂ mean anomalies are 3.5/1.6 and -2.9/-4.0 ppm, respectively. Finally, for radiation < 300 W m ⁻² the NA and SA model/data CO ₂ mean values are -0.4/-0.2 and 0.7/1.9 ppm, respectively.	45
3.5	Simulated total column CO ₂ concentrations at the WLEF tower (black line) and the sky conditions (grey line), where 0 indicates clear sky and 1 indicates the tower was cloud covered. The vertical dashed lines indicate the three frontal passages.	48
3.6	Simulated total column CO ₂ concentrations at the Tapajos tower (solid line) and the modeled sky conditions (shaded line), where 0 indicates clear-sky and 1 indicates the tower was cloud covered. . .	51

3.7	Sampling distributions of the spatial representativeness errors in NA (solid) and SA (shaded) at 1300 LST compiled from all days of the simulations. The x axis is the difference between the simulated satellite concentration and the domain mean concentration, and the y axis is the number of satellite tracks that correspond to each difference. Negative values indicate an underestimation by the simulated satellite measurements and positive values indicate an overestimation. Results from the fine grid columns (top) and distribution of the errors from the coarse grid columns (bottom).	54
3.8	Local clear-sky total column CO ₂ errors for NA (solid) and SA (shaded), which are the differences between the simulated satellite concentrations at 1300 LST using only clear-sky pixels and the simulated satellite concentrations at the same time using all the pixels in the satellite track. Errors from the fine grid (top) and results from the coarse grid (bottom).	57
3.9	Diurnal sampling errors for NA (solid) and SA (shaded), which are the differences between the simulated satellite concentrations from each track using only clear-sky pixels and the diurnal mean CO ₂ concentration from the entire domain, from 0000 to 0000 UT. . . .	59
3.10	Temporal sampling errors for NA (solid) and SA (shaded), which are the differences between the simulated satellite concentrations from each track using only clear-sky pixels and the 10-d domain average. Fine grid column (top) and coarse grid column (bottom) results.	62

4.1	Annual mean temporal sampling errors, obtained by subtracting the annual mean at each grid cell from the annual mean in the OCO subset.	74
4.2	Top) Zonal averages of the annual mean temporal sampling errors. The black line indicates the total zonal mean, the green line shows the zonally-averaged errors over land and the blue line shows the zonally-averaged errors over ocean. Bottom) Zonal standard deviations of the annual mean temporal sampling errors.	74
4.3	Seasonal temporal sampling errors, calculated by subtracting the grid cell mean for each season from the grid cell mean in the OCO subset.	75
4.4	Seasonal zonally-averaged temporal sampling errors.	76
4.5	Seasonal zonally-averaged standard deviations of the temporal sampling errors.	76
5.1	Percent land cover classifications using only C3 vegetation classes. Fractions < 1. are due to the presence of surface water.	91
5.2	Percent land cover classifications including both C3 and C4 vegetation classes.	92
5.3	Percent land cover classifications including C3 and C4 vegetation and patches.	94
5.4	The locations of the tower sites used in this study.	95
5.5	Monthly diurnal composites of the NEE at boreal forest sites. . . .	102
5.6	Monthly diurnal composites of the NEE at needleleaf forest sites. .	103
5.7	Monthly diurnal composites of the NEE at mixed forest sites. In the third row at the Duke Forest sites, the solid line displays the fluxes from DPP while the dashed line shows the NEE at DHD. . .	104

5.7	Monthly diurnal composites of the NEE at mixed forest sites. In the third row at the Duke Forest sites, the solid line displays the fluxes from DPP while the dashed line shows the NEE at DHD. . . .	104
5.8	Monthly diurnal composites of the NEE at crop and grassland sites.	105
5.9	Root mean square errors at each of the tower sites for the mean daytime concentrations (top panel) and the mean nighttime concentrations (bottom panel). Daytime hours are from 1800 UT to 0000 UT and nighttime hours are from 0300 UT to 1200 UT. Red=C3 simulation, Green=C4 simulation, Blue=Patches simulation.	106
5.10	Taylor plot of the daytime mean CO ₂ concentrations.	108
5.11	Map of the mean NEE from May through August, 2004. The results shown are from the PAT simulation, using both C4 vegetation and patches.	109
5.12	Maps of the differences between the mean NEE between simulations. The left hand panel shows the differences between the C4 simulation and the C3 simulation, and the right hand panel displays NEE differences between the PAT and C4 simulations.	110
5.13	Maps of the monthly mean NEE for each simulation.	111
5.14	Total column CO ₂ concentrations due only to biological fluxes. . . .	113
5.15	Differences between the total column CO ₂ concentrations. The left hand panel shows the differences between C4 and C3 simulations. The right hand panel shows the differences between PAT and C4 simulations.	114

5.16	Maps of the differences between the simulations for each month. The left hand column shows the differences between the C4 and C3 simulations, while the right hand column shows the differences between the PAT and C4 simulations. May is in the top row and August is in the bottom row.	115
5.17	Maps of the May through August mean contribution of individual sources to the total atmospheric CO ₂ concentration, at 30 m. The top left panel shows the initial CO ₂ concentration on May 1. All maps have units of ppm and use the concentrations from the PAT case.	117
6.1	The Mid-Continent Intensive Campaign (MCI) Study Region. . . .	128
6.2	Map of corn (green) and soybean (purple) coverage over the MCI region. Provided by M. Hansen.	132
6.3	Percent land cover classifications for the BASE simulation, which does not include corn and soybean crops explicitly.	134
6.4	Grid setup for the NEST simulation. The interior grid is outlined in red on the coarse domain. The six red crosses indicate the towers in the MCI region that measure continuous CO ₂ concentrations, and the purple crosses show the flux towers in the region.	135
6.5	Percent land cover classifications including corn and soybeans from the Hansen (2008) crop map.	136
6.6	Percent land cover classifications for the interior grid of the NEST case, which includes corn and soybeans from the Hansen (2008) crop map.	137

6.7	Leaf area index (LAI) of crops in rotation in Bondville. Corn in 1999 is displayed in the top panel and soybeans in 2000 are displayed in the bottom panel. The drop of LAI towards the end of the growing season represents the field drying and harvest events (from Lokupitiya et al. (2008)).	141
6.8	Leaf area index (LAI, left panel) and fraction of photosynthetically active radiation (FPAR, right panel) from the BASE simulation without the crop model (blue) and from the CROP simulation (red). The values plotted are the means from all of the gridcells that have corn (solid) and soybeans (dotted). In the BASE case, since these crops are not included, we plotted the mean MODIS LAI and FPAR for the corresponding gridcells.	142
6.9	Monthly means of net ecosystem exchange (NEE) for Bondville site. Observed and predicted NEE from SiB before any modification (top), and simulation results from the new crop phenology model (bottom). Even years are soybeans and odd years are corn (from Lokupitiya et al. (2008)).	144
6.10	Mean NEE for corn (top) and soybeans (bottom) for both the BASE (blue) and CROP (red) simulations. Since the BASE simulation does not include corn and soybean explicitly, we calculated the mean NEE from the corresponding gridcells where the vegetation cover was C4 crops for corn and C3 grass/crop for soybean.	145
6.11	NEE observed at the Fermi National Accelerator Agricultural Site over a soybean field (black) and modeled NEE at the nearest soybean gridcell in the CROP simulation (red).	146

6.12	Map of the mean NEE from June through August, 2007, for both the BASE (left) and CROP (right) simulations.	148
6.13	The mean June through August total column concentration difference between CROP and BASE, calculated by subtracting the mean BASE concentrations from the CROP concentrations.	149
6.14	Mean CO ₂ concentrations at 120 m from June through August from the CROP simulation. The mean wind vectors at 120 m are overlaid.	150
6.15	Mean CO ₂ concentrations at 120 m from June through August from the interior grid in the NEST case. The mean wind vectors at 120 m are overlaid. The black dots represent the towers.	151
6.16	Root mean square errors (RMSE) for daytime (1800 - 0000 UT, top) and nighttime (0300 - 1200 UT, bottom) for the three cases: BASE=blue, NEST=green, and CROP=red.	152
6.17	Taylor diagram of the daytime minimum concentrations for the BASE (blue), NEST (green), and CROP (red) cases. Daytime minima are used to remove the diurnal cycle of CO ₂ to investigate the model's ability to capture the synoptic variability. The contours indicate a fitness score based on a combination of the normalized standard deviation and the correlation (Taylor, 2001). The towers are labeled A-F as in Table 6.1. The gradient between the towers is also calculated for the both observations and the simulations, and is represented by G. The gradient is the highest daytime minimum concentration across all towers minus the lowest daytime minimum concentration on the same day.	154

6.18	Daytime minima at all the towers for the CROP simulation (top) and the observations (bottom). Each tower is a different color: MEAD=black, RL=purple, CEN=blue, WBI=green, GV=yellow, and KW=red.	156
6.19	The measured gradient between the towers (black) and the simulated gradient in the CROP case (red). The gradient is the difference between the lowest and highest daytime minimum values across the towers.	158
6.20	Mean daytime (1800 - 0000 UT) concentrations on 16 July, 2007 at 120 m for the CROP case with the mean wind vectors overlaid. . .	159
6.21	Mean daytime concentrations on 16 July at 120 m over the MCI region in interior grid of the NEST case.	160
6.22	Mean daytime concentrations on 19 July at 120 m for the CROP case.	161
6.23	Mean daytime concentrations on 19 July at 120 m for the interior grid of the NEST simulation.	162
7.1	Fossil fuel fluxes from the Andres et al. (1996) distribution (left panel) and the Vulcan inventory by Gurney et al. (2008) (right panel). The Andres et al. (1996) flux was calculated from the annual emissions estimates and is emitted every timestep in the model. The flux from Vulcan shown is the annual mean emissions for comparison. In the model the Vulcan emissions change hourly.	171

7.2	Root mean square errors at each of the tower sites for January through April (top left), May through August (top right), and September through December (bottom center). The blue bars show the results from the FF95 case and the red bars show the results from the HRFF case.	173
7.3	Taylor diagrams of the daytime minimum concentrations for the FF95 (blue) and HRFF (red) cases. The towers are labeled A-K as in Table 7.1. The missing towers during both JFMA and SOND are due to missing data.	175
7.4	Annual mean 30 m CO ₂ concentrations due only to fossil fuel emissions for the HRFF case. Annual mean wind vectors at 396 m are overlaid.	177
7.5	Difference between the annual mean fossil fuel emissions estimates by Andres et al. (1996) and Gurney et al. (2008), calculated by subtracting the Andres et al. (1996) emissions from the annual mean flux in the Vulcan inventory.	179
7.6	Annual mean CO ₂ concentration differences at 30 m between the FF95 and HRFF cases (HRFF - FF95).	180
7.7	Monthly total fossil fuel emissions over the United States from the Vulcan inventory.	181
7.8	Seasonal cycle of the Vulcan fossil fuel emissions estimates. The fluxes shown are the differences between the monthly mean emissions and the annual mean emissions.	182
7.9	Monthly differences in the 30 m concentrations between the FF95 and the HRFF cases (HRFF - FF95).	184

List of Tables

2.1	NEE and PBL Height (z_i) Values Used in the Box Model and the Resulting CO ₂ Biases.	26
3.1	Range and Standard Deviation (σ) of the Simulated Grid Columns at 1300 LST. Both the mean values over the entire simulation and the maximum values are displayed. Units are in ppm.	49
3.2	Mean (μ) and Standard Deviation (σ) of the Sampling Distributions of the Spatial Representation Errors, the Local Clear-Sky Errors, the Diurnal Sampling Errors, and the Temporal Sampling Errors for All Four Cases. Units are in ppm.	53
5.1	Vegetation classification at each of the towers, in percent land cover. The first number is the percentage of coverage for the C3 run, the second number is the percent coverage for C4, and the final column is the coverage for the PAT case. The cover at the actual tower is depicted by an x. The remaining coverage not depicted is water. . .	99
6.1	Location and sampling height of each of the towers measuring continuous CO ₂ concentrations in the MCI region. The sampling heights are in meters above ground level.	138
7.1	List of the towers that collected 2004 CO ₂ concentrations and that were used in this study.	172

8.1 Total column variability due to the three causes investigated in this study: clear-sky concentrations from satellites, agricultural production, and fossil fuel redistribution. The values shown are the maximum total column differences, in ppm. 194

Permission to Include Excerpts Published in Scholarly Journals

- The article “Using Continuous Data to Estimate Clear-Sky Errors in Inversions of Satellite CO₂ Measurements” is included as Chapter 2 in this dissertation and is reproduced by permission of the American Geophysical Union. An edited version of this paper was published by AGU. Copyright 2006 American Geophysical Union.

Corbin, K. D. and A. S. Denning, (2006), Using Continuous Data to Estimate Clear-Sky Errors in Inversions of Satellite CO₂ Measurements, *Geophysical Research Letters*, **33**, L12810, doi:10/1029/2006GL025910.

- The article “Possible Representation Errors in Inversions of Satellite CO₂ Retrievals” is included as Chapter 3 in this dissertation and is reproduced by permission of the American Geophysical Union. An edited version of this paper was published by AGU. Copyright 2008 American Geophysical Union.

Corbin, K. D., A. S. Denning, L. Lu, J. -W. Wang, and I. T. Baker, (2008), Possible Representation Errors in Inversions of Satellite CO₂ Retrievals, *Journal of Geophysical Research*, **113**, D02301, doi:10.1029/2007JD008716.

- The article “Assessing Temporal Clear-Sky Errors in Assimilation of Satellite CO₂ Retrievals Using a Global Transport Model” is included as Chapter 4 in this dissertation and is reproduced by permission of the European Geosciences Union and Copernicus Publications.

Corbin, K. D., A. S. Denning, and N. C. Parazoo, (2008), Assessing Temporal Clear-Sky Errors in Assimilation of Satellite CO₂ Retrievals Using a Global Transport Model, *Atmospheric Chemistry and Physics Discussion*.

1 Introduction

1.1 Why Study Atmospheric CO₂?

The basic reason why the amount of CO₂ in the atmosphere is important can be formulated as the English physicist Tyndall stated in the 1860s: “How does the content of CO₂ in the atmosphere affect its radiation balance and consequently the heat balance at the Earth’s surface?” (Bach et al., 1983). CO₂ is transparent to shortwave radiation, but not to the infrared wavelengths re-radiated back to space. Since CO₂ absorbs longwave radiation and re-emits it to Earth, the temperature at the surface must increase for the Earth to radiate to space all the energy received from the sun, which is called the “greenhouse effect”. Since increasing atmospheric CO₂ concentrations will impact the Earth’s climate, it is essential to understand the carbon cycle. The importance of atmospheric CO₂ is stated by the National Research Council in 1977: “At the heart of the concern is the anthropogenic climate change that may be too gradual to detect until it is well advanced, too advanced to stop by the time it is detected, and capable of inducing profound changes in

the delicate environmental balances that determine whether global breadbaskets will produce adequate food supplies and whether coastal areas will be affected by rising sea levels” (NRC, 1977).

1.2 The Global Carbon Cycle

Carbon is exchanged among the atmosphere, oceans, terrestrial biosphere and sedimentary rocks (Figure 1.1). Prior to the industrial revolution, the carbon cycle can be assumed to have been in balance, with the large ocean ($\sim 90 \text{ Gt C yr}^{-1}$) and biosphere ($\sim 120 \text{ Gt C yr}^{-1}$) sources approximately equal to the sinks. Over land, the amount of CO_2 fixed from the atmosphere and taken up by plants during photosynthesis is known as gross primary production (GPP). Annual plant growth is the difference between photosynthesis and autotrophic respiration, and is referred to as net primary production (NPP). Most dead biomass enters the detritus and soil organic matter pools, where it is respired (R_h) at a rate that depends on the chemical composition of the dead tissues and on environmental conditions. In the absence of disturbance, the net carbon flux is the difference between R_h and NPP, which is referred to as the net ecosystem exchange (NEE).

Humans have been perturbing the carbon cycle for the past 250 years, primarily through the combustion of fossil fuels and through land use change. Fossil fuel and cement emissions have increased to $7.2 \pm 0.3 \text{ Gt C yr}^{-1}$ based on international energy statistics for the 1980 to 2003 period (Marland et al., 2005). Land

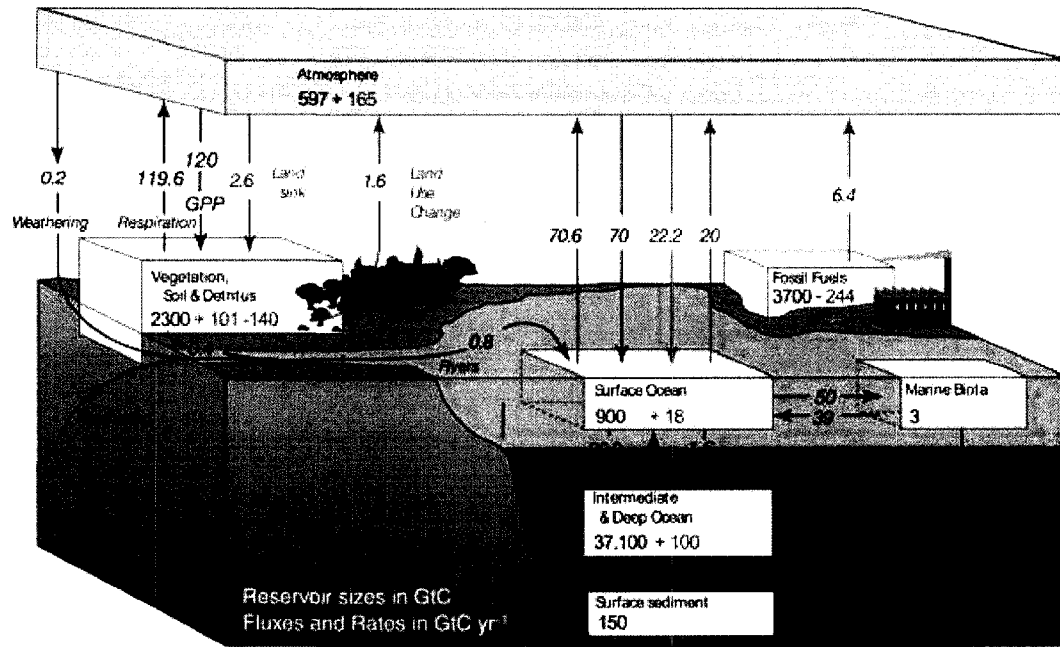


Figure 1.1: The global carbon cycle for the 1990s, showing the main annual fluxes in Gt C yr⁻¹: pre-industrial 'natural' fluxes in black and 'anthropogenic' fluxes in red. Atmospheric carbon content and all cumulative fluxes since 1750 are as of end 1994. From Denman et al. (2007).

use change has also altered the CO₂ flux. Deforestation in the tropics releases a significant amount carbon to the atmosphere, causing a global source of ~ 1.6 Gt C yr⁻¹ (Denman et al., 2007).

Due to the anthropogenic sources, atmospheric CO₂ concentrations are increasing, with an accumulation of ~ 4.1 ± 1. Gt C yr⁻¹ (Denman et al., 2007). Natural sinks of carbon take up the remainder of the emitted CO₂. Most recent estimates suggest that the net ocean-to-atmosphere flux is -2.2 ± 0.5 Gt C yr⁻¹ and that the net land-to-atmosphere flux is -0.9 ± 0.6 Gt C yr⁻¹. The location and mechanisms of the natural sinks is currently a topic of research.

1.3 Monitoring the Atmospheric CO₂ Concentration

In the late nineteenth century, Arrhenius and Chamberlain first presented the theory that climate changes are related to fluctuations in atmospheric CO₂ (Arrhenius, 1896; Chamberlain, 1899). Nearly fifty years later, Callendar (1940) concluded from available CO₂ measurements that the atmospheric CO₂ concentration at the turn of the century averaged 290 ppm and has been steadily increasing due to man's increased burning of fossil fuel. Callendar (1940) found a 10% increase in CO₂ concentrations from 1890 to 1935.

Discussion of atmospheric CO₂ ceased until after World War II, when Plass (1956) and Revelle and Suess (1957) used ¹⁴C in tree rings to show that the increase in atmospheric CO₂ was not consistent with Callendar's estimates. This discrepancy led Rossby to argue for more systematic monitoring of the atmospheric CO₂ concentrations around the globe at a chemistry conference in 1954. As a result of the conference, the first network of CO₂ monitoring stations was established using wet chemistry methods (Bach et al., 1983). Data from the stations confirmed the increase in CO₂ advocated by Callendar (1958), although the measurements were clearly influenced by vegetation.

At the same time in history, the infrared gas analyzer was invented, which measures the extinction of infrared radiation in a column of dry air. This new measurement technique allowed continuous monitoring of CO₂ in the atmosphere and rendered an accuracy much higher than the wet chemistry techniques.

Since the atmospheric CO₂ concentrations remained uncertain, Wexler of the U. S. Weather Bureau proposed to measure CO₂ in non-polluted air during the International Geophysical Year 1956-1958. Under the supervision of C. D. Keeling of the Scripps Institute of Oceanography, continuous CO₂ monitoring began in early 1958 at the Mauna Loa Observatory on Hawaii. Measurements have continued at this site ever since. In addition to the measurements at Mauna Loa, continuous measurements at Antarctica began in 1960, observations were taken from aircraft en route from Stockholm to Los Angeles and in the Arctic and North Pacific, measurements were made from ships in the Pacific, and occasional monitoring occurred at Point Barrow.

The first publication using these data focused on large-scale mixing deduced from variations in atmospheric CO₂ (Bolin and Keeling, 1963), concluding that CO₂ was an excellent atmospheric tracer and that land vegetation north of 45°N was responsible for net consumption of CO₂ during the northern summer.

During the 1960s, little interest was shown in expanding the monitoring of atmospheric CO₂, and most of the research involving CO₂ was focused on studying the general circulation of the atmosphere using CO₂ as a tracer. The aircraft data were organized by Bolin and Bischof (1970); and their analysis focused on the seasonal cycle in the northern hemisphere, which reflected the influence of the biosphere, and on the 5.7 ppm increase in CO₂ from 1960-1968.

Following this study, concern was raised about how rapidly CO₂ could build up in the atmosphere. During the 1970s, recognition of a growing world popula-

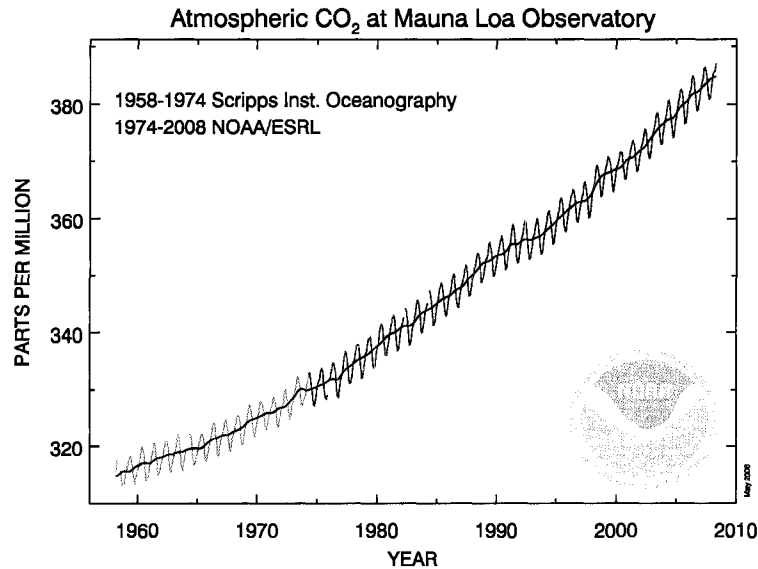


Figure 1.2: Time series of atmospheric CO₂ concentration at Mauna Loa, Hawaii, since 1958.

tion, the rising per capita use of energy, and the concomitant growth in the rate of fossil fuel CO₂ emissions focused attention on the atmospheric CO₂ increases being documented. Keeling et al. (1976) published a more complete picture of the fluctuations in atmospheric CO₂ (see Figure 1.2). Seasonal fluctuations at Mauna Loa were very stable with an annual maximum in spring and a minimum in early summer, in agreement with Bolin and Bischof (1970). The long term trend in CO₂ was also analyzed, confirming the increasing atmospheric CO₂ concentrations.

Over the past three decades the measuring network of CO₂ has dramatically expanded. In 1980, nine stations around the globe measured continuous CO₂ and approximately ten flask sites, where CO₂ was sampled once a week, were being operated by the National Oceanic and Atmospheric Administration (NOAA) (Trabalka, 1985). Flask and continuous CO₂ measurements are now being made not

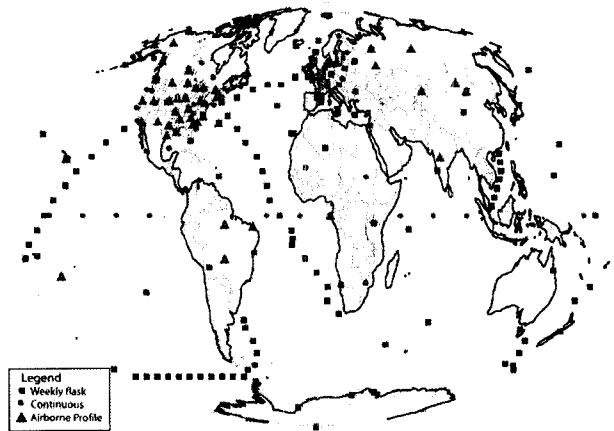


Figure 1.3: The global network of CO₂ observations in 2007.

only in remote environments characterized by background concentrations of CO₂, but also in continental locations influenced by both biospheric and anthropogenic fluxes. Currently, over 100 surface flask sites are stationed around the world, CO₂ is being measured continuously at more than sixty towers throughout the world, and airborne profiles are made regularly at over 20 sites (see Figure 1.3, Denning et al. (2007)). To complement the existing ground-based CO₂ network, two satellite missions designed specifically to retrieve global measurements of the total column dry air mole fraction X_{CO_2} with precisions of ~ 1 ppm are scheduled to launch in December 2008 (Crisp et al., 2004; NIES, 2006). In addition to measurements of atmospheric CO₂ concentrations, fluxes of carbon dioxide, water vapor, and energy between the biosphere and the atmosphere are measured over a network of tower sites, called FLUXNET (Baldocchi, 2006). FLUXNET is a global network of over 150 micrometeorological flux measurement sites that use eddy covariance techniques to calculate the surface fluxes.

1.4 The Missing Carbon Sink and Atmospheric Inversions

While concern over the increasing CO₂ concentration grew and the network of CO₂ monitoring stations began expanding to provide data for research, ocean modelers first began to express the inability of known ocean sinks to account for all the carbon released to the atmosphere from fossil fuel burning and land-use changes (Broecker et al., 1979; Siegenthaler and Oeschger, 1978). The unaccounted for difference between the growth rate of atmospheric concentrations, the anthropogenic release rate of CO₂, and the uptake rate by known sinks has been dubbed the “missing sink”, since only approximately half of the emissions have remained in the atmosphere. Atmospheric measurements confirmed the existence of a missing sink and suggested that the sink is in the northern hemisphere, as the north-south gradient of CO₂ is substantially smaller than expected if carbon sinks were evenly distributed around the world (Tans et al., 1990). Understanding the missing sink, including the location of the sink and the processes involved, became a research focus that is still being actively pursued.

A branch of research in the scientific community has focused on understanding the carbon sink using inverse modeling. Inversions use atmospheric CO₂ concentrations and transport models to calculate surface sources and sinks of carbon. This method is also referred to as the “top-down” approach since source and sink distributions are estimated without knowledge of details regarding finer-scale variability or underlying processes that cause the fluxes.

In the early 1990s, two different hypotheses were proposed to explain the northern hemisphere sink. Keeling et al. (1989) stated that the sink reflected a natural source/sink pattern of oceanic CO₂ fluxes, postulating that the North Atlantic takes up CO₂ and transports it south as part of the large-scale ocean circulation. In contrast, Tans et al. (1990) showed the sink must be on land using observations of air-sea differences in partial pressure of CO₂ as constraints in an atmospheric inversion. Investigating the two strongly diverging hypotheses dominated much of the carbon cycle research in the 1990s.

Using sixteen different transport models and model variants, the TransCom 3 project investigated estimates of surface CO₂ fluxes from an inter-comparison of atmospheric CO₂ inversion models. Gurney et al. (2002) found a northern land carbon sink evenly distributed across the northern hemisphere. This result agreed with direct observations (Baldocchi et al., 2001) and inventory estimates (Houghton, 1999; Pacala et al., 2001b); however, estimates of its magnitude vary widely from -0.6 to -2.3 Gt C yr⁻¹ (Heimann, 2001). Large uncertainties in the flux estimates exist because of the sparsity of available observations, numerical inaccuracy and limited spatial resolution of transport models, representation errors between the data and the model, errors in the prior constraint on source/sink strengths, and observation errors (Gurney et al., 2002; Bakwin et al., 1998; Engelen et al., 2002).

As the atmospheric measurement network expands and more computer resources become available, inversions are incorporating more sources of data and

shifting to higher spatial and temporal resolutions on regional domains. Continuous CO₂ concentrations can be used in both global and regional inversions to reduce the data constraint (Law et al., 2003, 2002; Peters et al., 2007; Schuh et al., 2008), and assimilation systems are being developed to incorporate satellite data (Baker et al., 2006a; Chevallier et al., 2007). Methods have also been developed to perform regional inversions to infer fluxes at high temporal and spatial resolution (Peylin et al., 2005; Peters et al., 2007; Zupanski et al., 2007). Although advances have been made in data assimilation techniques, the missing sink of carbon still remains uncertain and a topic of much research.

1.5 Atmospheric CO₂ Variability

In addition to investigating the missing sink, considerable research has been done to understand the underlying causes of variability in the atmospheric CO₂ concentrations on annual, seasonal, and diurnal timescales. Since Keeling et al. (1976) first discussed interannual variability in atmospheric CO₂ concentrations, research has investigated changes in the growth rate of CO₂. The dominant cause of interannual variability in the rate of increase of atmospheric CO₂ is atmospheric circulation anomalies and associated changes in temperature and precipitation. Links have been found between the interannual growth rate and the El Niño - Southern Oscillation (ENSO) (Sarmiento and Gruber, 2002; Keeling et al., 1989; Bacastow, 1976), the Northern Annular Mode (NAM) (Barnston and Livezey, 1987; Russell

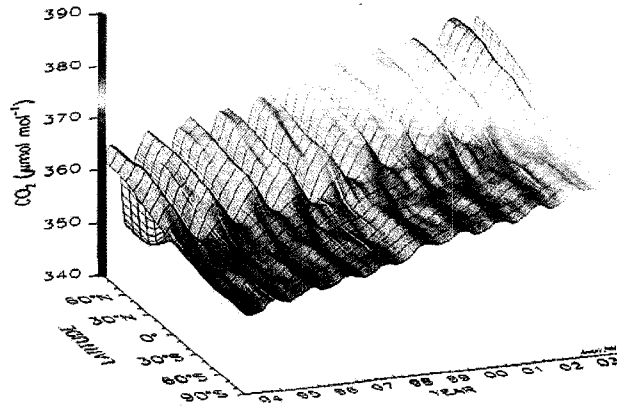


Figure 1.4: Variations of atmospheric CO₂ concentration by time and latitude based on samples collected by the NOAA flask network.

and Wallace, 2004), and volcanic eruptions (Sarmiento, 1993; Battle et al., 2000; Jones and Cox, 2001).

Keeling et al. (1976) also began a series of studies investigating the seasonal cycle of atmospheric CO₂. Systematic variations on the order of 10% are now known to occur both seasonally and regionally (see Figure 1.4, Conway et al. (1994, 1988)). The northern hemisphere has a pronounced seasonal cycle of CO₂ that follows the seasonal growth and decay of the terrestrial biosphere. Tropical ecosystems experience a much weaker amplitude in the seasonal cycle, and in the southern hemisphere the seasonal cycle is out of phase with that in the northern hemisphere and is much weaker due to the larger areal fraction of ocean.

Atmospheric CO₂ concentrations are also known to vary on diurnal timescales (Keeling et al., 1976; Bakwin et al., 1998; Denning et al., 2003). The diurnal cycle of CO₂ near the land surface is driven by the diurnally varying biological fluxes and the covariance between the dynamics of the planetary boundary layer (PBL)

and the surface fluxes, which is called the rectifier effect (Denning et al., 1996a,b). During the day, low concentrations exist in the deep well-mixed PBL, while at night high concentrations build up under the shallow and stably stratified PBL.

As our understanding of the carbon cycle increases and as our modeling tools advance, more of the variability in the atmospheric CO₂ concentrations is being explained. While fifteen years ago the atmospheric CO₂ concentrations were regarded as well-mixed and synoptic variability was considered noise, those same synoptic changes in the concentrations are now being analyzed to further our knowledge about atmospheric CO₂ and its sources and sinks.

Atmospheric variability of over 30 ppm at the surface has been shown to be due to mid-latitude synoptic weather systems and fronts, and the mechanisms behind the variability are being discovered (Parazoo et al., 2008; Geels et al., 2004; Chan et al., 2004). Over North America, frontal systems cause large horizontal gradients in CO₂ due to deformational flow that is associated with cloud cover. Large gradients in CO₂ have also been shown to be due to topography and meso-scale features such as land-water surface roughness changes and sea breezes (e.g. Nicholls et al., 2004; Lu et al., 2005; van der Molen and Dolman, 2007). While studies have begun to investigate the influence of synoptic and meso-scale features on atmospheric CO₂ concentrations, future work is required to investigate additional causes of the high-frequency variability.

1.6 Objectives

To interpret high frequency CO₂ changes, we need to understand the mechanisms controlling the variability. Forward models are valuable tools to help enhance our understanding of the processes driving the atmospheric CO₂ variability. We have constructed a high-resolution self-consistent, mechanistic model of land-atmosphere CO₂ exchange and transport by coupling an ecosystem model to a regional atmospheric model. This coupled model utilizes numerous datasets: meteorological fields, soil type, biome type, leaf area index (LAI) and fraction of photosynthetically active radiation (FPAR), atmospheric CO₂ concentrations, atmospheric CO concentrations, OH concentrations, sea-surface pCO₂, fossil fuel fluxes, and fire emissions. By using these observational constraints, the model produces realistic fields that reflect our current understanding of the carbon cycle.

The main objective of this research is this tool to further our knowledge of the carbon cycle. In a series of three studies, this research will investigate causes of regional variations in atmospheric CO₂ concentrations. While numerous studies have investigated CO₂ variability due to synoptic systems and meso-scale features, little work has been done to investigate the variability of both surface and total column concentrations in clear-sky conditions only. In addition, the influence of land cover heterogeneity, specific biome classifications, crops and agricultural ecosystems, and fossil fuel emissions on atmospheric CO₂ concentrations is also not well understood.

The first study focuses on analyzing the implications of measuring CO₂ concentrations in clear-sky conditions only, as well as the spatial and temporal variability of total column CO₂ concentrations, to understand representation errors that may be introduced into inversions that use total column satellite retrievals. Satellite X_{CO₂} data will soon be available, and it is essential to correctly implement this data into atmospheric inversions to avoid biasing flux estimates. Since satellite data will only be available in clear conditions, it is important to understand how CO₂ concentrations on clear days compare with average conditions. Chapter 2 compares clear-sky concentrations to mean concentrations including all sky conditions at two mid-latitude forests in a first look at clear-sky differences using observations. Chapter 3 expands the local clear-sky analysis by investigating clear-sky simulated total column satellite measurements using a high-resolution cloud-resolving model that simulates concentrations over a mid-latitude region and a tropical region. Chapter 4 further expands the clear-sky total column CO₂ analysis by evaluating global clear-sky sampling differences.

The second study focuses on analyzing the impact of different vegetation coverage on the atmospheric CO₂ concentrations. Chapter 5 evaluates the impact of sub-grid heterogeneity on both carbon fluxes and CO₂ concentrations using a coupled ecosystem-atmosphere model. Chapter 6 implements a crop phenology model into the regional model and analyzes the impacts of crops on the atmospheric CO₂ concentrations. The resulting atmospheric concentrations and gradients in the model are compared with an intensive measurement campaign in the Midwest.

The final study investigates the sensitivity of atmospheric CO₂ concentrations to changes in fossil fuel emissions, focusing on analyzing the impacts of spatially and temporally redistributing these emissions. Chapter 7 presents a preliminary evaluation of a new fossil fuel inventory with high spatial and temporal resolution and analyzes the resulting changes in the atmospheric CO₂ concentrations. Conclusions from the studies are presented in Chapter 8.

2 Using Continuous Data to Estimate Clear-Sky Errors in Inversions of Satellite CO₂ Measurements

An edited version of this chapter was published by AGU. Copyright 2006 American Geophysical Union. Reproduced by permission of American Geophysical Union. Figure numbers, equation numbers, and citation styles have been changed for integration into the dissertation.

Corbin, K. D. and A. S. Denning, (2006), Using Continuous Data to Estimate Clear-Sky Errors in Inversions of Satellite CO₂ Measurements, *Geophysical Research Letters*, **33**, L12810, doi:10/1029/2006GL025910.

Abstract

We used continuous measurements of atmospheric CO₂ at two stations to investigate potential errors in inversions of temporal averages of satellite clear-sky column retrievals. Compared to the complete data sets, the mid-day CO₂ on clear days was systematically lower with a larger winter difference. Net ecosystem exchange (NEE) of CO₂ was enhanced on clear vs. all days, the summer boundary layer was deeper, and the CO concentration was systematically lower. During winter these

differences cannot account for the CO₂ bias, which must be caused by advection. Summertime errors reflect a tradeoff between deeper mixing and enhanced NEE on clear days. If these sites represent mid-latitude forests and if the CO₂ difference is confined to the bottom 15% column mass, then inversions of temporally-averaged satellite column data products will incur a -0.2 to -0.4 ppm bias. CO₂ concentrations must therefore be assimilated at the time and place observed.

2.1 Introduction

An important method to help quantify the large-scale surface exchanges of carbon is by tracer transport inversion, which uses atmospheric CO₂ concentrations and a transport model to infer information about surface sources and sinks (Gurney et al., 2002; Rodenbeck et al., 2003; Baker et al., 2006b); however, flux estimates are still highly uncertain in many regions due to sparse data coverage (Gurney et al., 2003). Due to their global spatial sampling and data volume, satellite CO₂ measurements may help improve the inverse modeling constraint, particularly in regions that are poorly sampled by existing ground-based CO₂ monitoring networks. Global simulations with source-sink synthesis inversion models indicate that uncertainties in the atmospheric CO₂ balance could be reduced substantially if data from the existing in situ network were augmented by spatially-resolved, global measurements of the column-integrated dry air mole fraction (X_{CO_2}) with precisions of ~ 1 ppm (Rayner and O'Brien, 2001; Houweling et al., 2004).

The Orbiting Carbon Observatory (OCO), scheduled to launch in early 2009, is designed specifically to observe X_{CO_2} with $\sim 0.3\%$ (1 ppm) precision on regional scales (Crisp et al., 2004). OCO will fly in a polar, sun-synchronous orbit just ahead of the Earth Observing System (EOS) Aqua Platform with a 13:15 equator crossing time and a 16-day repeat cycle; and it will collect high-resolution spectra of reflected sunlight in the $0.76 \mu\text{m}$ O₂ A-band and the CO₂ bands at $1.61 \mu\text{m}$ and $2.06 \mu\text{m}$. To maintain an adequate number of soundings even in the presence of patchy clouds, OCO will have a 10 km-wide cross-track field of view that is divided into eight 1.25 km-wide samples with a 2.25 km down-track resolution at nadir.

To obtain near-surface information, retrievals of total column CO₂ concentrations from near-IR spectra measured by space-borne instruments will require clear-sky conditions. Systematic differences in atmospheric CO₂ in clear vs. cloudy conditions might be expected because of the dependence of the photosynthesis rate on the directional character of solar radiation. NEE is strongest on slightly cloudy days due to greater light-use efficiency for diffuse relative to direct beam radiation, which may lead to lower than average CO₂ mixing ratios on partly cloudy days (e.g. Freedman et al., 2001; Gu et al., 2002). Differences in atmospheric concentrations arising from differences in NEE depend on the spatial scale of the differences in radiative forcing: small-scale cloudy patches are expected to have less effect on concentrations than large-scale perturbations because of horizontal mixing by winds. In winter, since vegetation is not actively photosynthesizing, the a priori expectation is that CO₂ mixing ratios would not depend on cloud conditions.

In addition to differences arising from biology, clouds are frequently associated with fronts, changes of air masses and convection with strong vertical motion, so atmospheric transport may be systematically different on clear vs. cloudy days.

Systematic differences in atmospheric CO₂ concentrations between clear and cloudy conditions would introduce sampling errors into tracer transport inversions that use satellite CO₂ products to represent temporal averages. Satellite retrievals of only clear pixels might overestimate spatial or temporal averages of CO₂ because they will not see conditions with enhanced uptake. Alternatively, heavy overcast conditions are expected to suppress NEE due to strongly reduced radiation and could lead to systematic underestimation from space-borne measurements during the growing season. Sampling errors could also be caused by advection associated with cloud cover. Depending on the treatment of the observations in the models, this sampling error could potentially introduce a bias; however, if modelers use satellite data at the same time and location and with the same atmospheric situation as the retrievals, these sampling errors would be eliminated. This study investigates clear-sky effects using continuous measurements of CO₂ concentrations from two tower sites over a period of several years.

2.2 Methods

We analyzed continuous data from two towers: a tall television tower near Park Falls, WI (WLEF 45.95°N, 90.27°W) and the Environmental Monitoring Site at

Harvard Forest, located in north-central MA (HF 42.54°N, 72.18°W). The WLEF tower is in a heavily forested zone of low relief, and mixed evergreen and deciduous forests dominate the area surrounding the tower (see Davis et al. (1997, 2003) for a description of the site and measurements). The CO₂ is measured at 396 m with two independent Licor CO₂ analyzers, which have a mean absolute value difference of 0.25 ppm. To reduce data gaps, we used the average between the two measurements when available and a single analyzer when one had missing data. Photosynthetically active radiation (PAR) is also measured; and the net ecosystem exchange of CO₂ (NEE, defined as the net flux out of the ecosystem) has been computed using eddy covariance methods. The WLEF CO₂ and PAR measurements are available from 1995 through 2003, and we used NEE values from 1997 through 2001. The HF tower is also in a mixed forest that contains oak, maple, hemlock, and spruce (see Wofsy et al. (1993); Goulden et al. (1996) for further details). Groups from the Atmospheric Sciences Research Center (ASRC) and Harvard University measure nearly continuous CO₂ concentrations, CO concentrations, PAR, turbulent CO₂ flux at 29 m, and the rate of change in canopy carbon storage below 29 m. All variables are available from 1993 through 2002. We calculated NEE at HF by subtracting the storage measurements from the turbulent CO₂ flux.

We sampled the continuous record of near-surface CO₂ at mid-day corresponding to the OCO planned overpass time. We analyzed two time periods: measurements at 1300 local time and the average value measured from 1100 through 1600 (the mean of six hours). The first represents individual nadir pixels and the

second represents the average of retrievals across an atmospheric transport model grid cell, which will be the basis of inversions using satellite CO₂ products. At a mean wind speed of 10 m/s, a six-hour average is equivalent to a 216 km swath of retrievals and comparable to global transport model grid scales. We chose to average six hours each day from 1100 to 1600 LST to avoid rapid variations in concentration associated with the morning and evening transitions between stable and mixed conditions.

Since long-term boundary layer (PBL) depth data are not available at either tower, we analyzed PBL heights from the European Centre for Medium Range Forecasts (ECMWF) 40-year Re-Analysis (ERA-40), which has a six-hour time-step. To capture the daytime PBL depth, we used values at 1800 UTC from the grid cells that included the towers.

We estimated the average difference in CO₂, NEE, CO, and PBL depth between clear and cloudy days by (1) creating clear-sky subsets of the time-series of each variable, (2) fitting separate analytical (harmonic) functions to the clear-sky subset and to the entire time-series, and (3) subtracting the two analytical functions to obtain a seasonal climatology of the clear-sky minus all-sky difference in each variable. Clear-sky subsets were defined by selecting the mid-day values of each variable for days on which measured PAR was greater than a threshold value defined by month for each site. The threshold PAR values were set by ranking measurements from all years at each site, then selecting the value corresponding to the percentage of clear days for each month at the nearest city recorded by the

National Climatic Data Center (NCDC). The NCDC monthly climatology of clear days is based on at least 40 years of data and is determined by human observers who categorize each daytime hour as clear if the average cloud cover was less than 30%. For WLEF, the nearest stations in the NCDC database are Green Bay, WI (232 km away); Duluth, MN (175 km); and Minneapolis/St. Paul, MN (262 km away). We used an average of the monthly clear-sky days from all three stations. At HF, the closest station is Worcester, MA (45 km). Since the NCDC clear-sky criterion is likely less stringent than satellite requirements, we decreased the reported percentages of clear days by 5% to ensure that the clear-sky differences are not overestimated by including partly cloudy days with enhanced NEE that will not be captured by satellites. The PBL depth clear-sky subsets included the same days as the clear-sky CO₂ subsets.

We separately fit seasonally-varying harmonic functions of each variable to the entire time-series and to the clear-sky subset using a linear least squares method. We removed data for February 29, de-trended the CO₂ concentration, and required both the variable being investigated and the PAR measurement to be valid at each hour. We found that two harmonics per year fit seasonal variations adequately, without introducing spurious noise. Differences between the harmonic fits to the clear-sky subsets and to the corresponding complete data sets are presented below and interpreted as the seasonal sampling error expected to occur in an average year by a satellite which only observes the atmosphere in clear conditions.

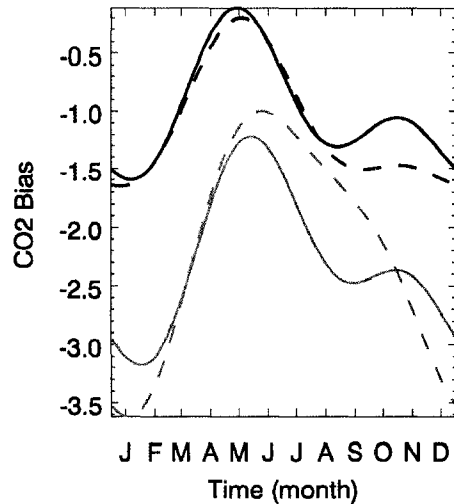


Figure 2.1: The clear-sky CO₂ sampling bias at WLEF (black) and at HF (gray), in ppm. Solid lines depict the 1100-1600 bias and dashed lines show the 1300 bias.

2.3 Results

Sampling the CO₂ concentration only on clear days resulted in underestimation of the mean concentrations at both towers at all times of year (Figure 2.1). The seasonal cycle of the sampling error is similar for all cases, with a greater near-surface difference in winter than during the summer months. At WLEF, the mean winter bias is -1.5 ppm and the mean summer bias is -0.8 ppm; and at HF the mean biases for winter and summer are -3.2 ppm and -1.5 ppm, respectively. The biases at the WLEF tower are smaller than at HF, which could reflect differences in vegetation or transport.

To explain the clear-sky CO₂ bias, we analyzed the clear-sky NEE bias (Figure 2.2). Both towers have a large negative summer bias due to increased photosynthesis on clear days and negligible to slightly positive differences in the winter.

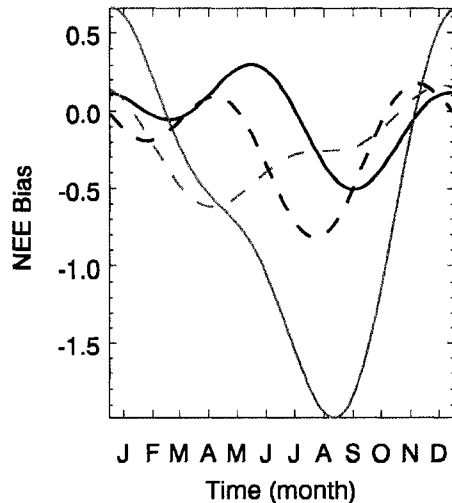


Figure 2.2: The NEE clear-sky bias, in $\mu\text{mol m}^2 \text{s}^{-1}$.

Meteorological factors such as increased temperature and water stress may contribute to the changes in magnitude and timing. We investigated the clear-sky temperature bias and found that the HF temperatures are greater on clear days than on average and that the summertime temperature bias is $\sim 0.4^\circ\text{C}$ greater at 1300 than from 1100-1600. The increased temperatures at 1300 could lead to increased respiration and decreased NEE, and these higher temperatures combined with the low solar zenith angle at 1300 may increase the water vapor pressure deficit, causing more stress on the vegetation and less CO_2 uptake.

Since the surface CO_2 concentration is dependent on both the surface fluxes and vertical mixing, we analyzed the PBL depth clear-sky bias (Figure 2.3). The clear-sky bias is positive in the summertime at both towers, with the PBL ~ 200 m deeper on clear days than on average. During the winter the magnitude of the bias is smaller and the PBL is slightly shallower on clear days.

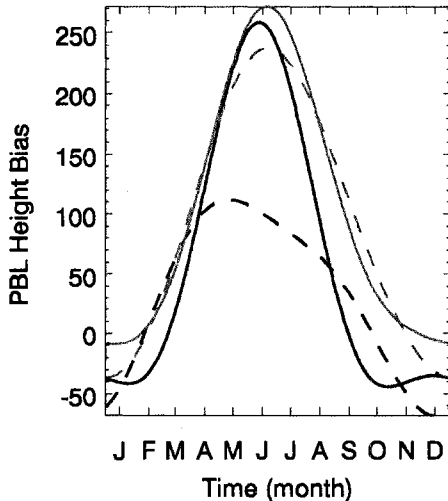


Figure 2.3: PBL depth clear-sky bias, in m.

We estimated the expected CO_2 bias from the mean differences in NEE and PBL height using a simple box model. We calculate a summer and winter estimate of the clear-sky effect on mixed-layer CO_2 concentration at both towers as

$$\Delta C = \Delta \left(\frac{NEE \Delta t}{\rho z_i / M_{air}} \right) \quad (1)$$

where ρ is the mean density of the mixed layer z_i is the mean depth of the daytime mixed layer, M_{air} is the molecular weight of dry air, and $\Delta t = 10$ hours is the duration over which the NEE difference was assumed to act. The NEE and z_i values and the resulting biases are summarized in Table 2.1. Although the box model is sensitive to the parameters used, it indicates that the summertime CO_2 bias is weak at the towers because the lower concentrations from enhanced photosynthesis are mixed into a deeper boundary layer, diluting the effect of the larger flux on clear days. In winter, the CO_2 biases are also weak, which is not surprising since

the PBL depth and NEE are nearly the same on clear days as they are on average. The box model suggests that the large winter CO₂ bias observed at both towers cannot be explained by differences in surface fluxes or vertical mixing, but instead likely results from non-local processes, such as advection.

	NEE $\mu\text{m}/\text{m}^2/\text{s}$	January/July z_i m	CO ₂ Bias ppm
		<i>WLEF</i>	
Clear	1./-8.	650/2100	0.1/-0.1
Total	1./-7.	700/1900	
		<i>HF</i>	
Clear	1.4/-13.5	925/2000	0.3/0.1
Total	1./-12.	950/1750	

Table 2.1: NEE and PBL Height (z_i) Values Used in the Box Model and the Resulting CO₂ Biases.

Finally, we calculated the bias in CO concentrations at HF (not shown). Since CO is a ubiquitous by-product of the same combustion processes as CO₂ and has an average lifetime of only 3 months, CO measurements can provide information on the intensity of anthropogenic activities (Palmer et al., 2003; Bakwin et al., 2004; Suntharalingam et al., 2004). The CO bias has a similar seasonal cycle to the CO₂ difference; and in both seasons the CO concentration is lower on clear days, indicating that the fossil fuel contribution is less. The mean clear-sky bias is -44 ppb and -18 ppb for January and July, respectively. Assuming that the primary source of CO is fossil fuel combustion and that the anthropogenic fluxes in the immediate vicinity of HF are negligible, the CO results indicate that part of the CO₂ bias is due to less advection of anthropogenic CO₂ on clear days. Using

an average combustion efficiency of 95% (Miller et al., 2003; Bakwin et al., 2004), the CO₂ bias resulting from reduced fossil fuel contributions on clear-sky days is ~ -0.5 ppm in the summer and ~ -1.2 ppm in the winter, or less than half the observed CO₂ difference at this site.

2.4 Conclusions

This study indicates that sampling only in clear conditions leads to a systematic underestimation of the mean CO₂ concentration at both WLEF and HF. In summer, the mean clear-sky bias in mixed-layer CO₂ is ~ -1.5 ppm at HF and -0.8 ppm at WLEF. A simple box model suggests that enhanced photosynthesis on clear days may be offset by a deeper boundary layer, mitigating some of the difference. During the winter, the clear-sky effects on NEE and boundary layer depth is weak, and the large observed CO₂ difference (~ -3 ppm at HF and -1.5 ppm at WLEF) cannot be explained in terms of local forcing. Seasonal patterns of mid-day differences in CO concentration at HF are similar to those of CO₂, with a greater difference in winter than summer, but are not sufficient to explain the CO₂ difference. Much of the clear-sky sampling error in CO₂ at these sites may be attributed to differential advection on clear vs. average days. Satellite retrievals of total column CO₂ concentrations are expected to be less affected by clear-sky sampling error than mixed-layer measurements. If these two sites are broadly representative of mid-latitude forested regions and if the CO₂ difference is confined to

a PBL occupying 15% of the column mass, then inversions of temporally-averaged satellite column data products will incur a -0.2 to -0.4 ppm bias. Therefore, satellite total-column CO₂ retrievals must be assimilated at the time and location of the observations.

Acknowledgements

We thank Steven Wofsy for the Harvard Forest data and Kenneth Davis for the data from the WLEF tower. This research was funded by NASA grant NCC5-621 and by NASA Earth System Science fellowship 53-1970. We gratefully acknowledge the constructive comments by two anonymous reviewers, which improved the quality of the manuscript.

3 Possible Representation Errors in Inversions of Satellite CO₂ Retrievals

An edited version of this chapter was published by AGU. Copyright 2006 American Geophysical Union. Reproduced by permission of American Geophysical Union. Figure numbers, equation numbers, and citation styles have been changed for integration into the dissertation.

Corbin, K. D., A. S. Denning, L. Lu, J. -W. Wang, and I. T. Baker, (2008), Possible Representation Errors in Inversions of Satellite CO₂ Retrievals, *Journal of Geophysical Research*, **113**, D02301, doi:10.1029/2007JD008716.

Abstract

Due to uniform spatial sampling and sheer data volume, satellite CO₂ concentrations can be used in inverse models to enhance our understanding of the carbon cycle. Using column measurements to represent a transport model grid column may introduce spatial, local clear-sky, and temporal sampling errors into inversions: the footprint is smaller than a grid-cell, total column concentrations are only retrieved in clear skies, and the mixing ratios are only sampled at one time. To investigate these errors, we used a coupled ecosystem-atmosphere cloud-resolving model to

create CO₂ fields over fine ($\sim 1^\circ \times 1^\circ$) and coarse ($\sim 4^\circ \times 4^\circ$) grid columns from 1 km² and 25 km² pixels that utilized explicit microphysics. We performed two simulations in August 2001: one in central North America and one in the Brazilian Amazon. Differences between satellite and grid column concentrations were calculated by subtracting the domain-mean column concentration from 10-km wide simulated satellite measurements. Spatial and local clear-sky errors were less than 0.5 ppm for the fine grid column; however, these errors became large and biased over the coarse grid column in North America. To avoid these errors, transport models should be run at high resolution. Using satellite measurements to represent bi-monthly averages created large (> 1 ppm) errors for all cases. The errors were negatively biased (~ -0.4 ppm) in the North American simulation, indicating that inverse models cannot use satellite measurements to represent temporal averages. Simulated representation errors did not arise because of differences in ecosystem metabolism in cloudy vs. sunny conditions; rather, they reflected large-scale CO₂ gradients in mid-latitudes that were organized along frontal boundaries and masked under regional cloud cover. Such boundaries were not found in the dry-season tropical simulation presented here and may be less prevalent in the tropics in general. To avoid incurring errors, inversions must accurately model synoptic-scale atmospheric transport and CO₂ concentrations must be assimilated at the time and place observed.

3.1 Introduction

Variations of atmospheric CO₂ concentrations contain information about sources and sinks which air interacts with as it is transported from place to place. Using atmospheric tracer transport models, inverse modelers can quantitatively estimate the strengths and spatial distribution of sources and sinks around the world from concentration data (Gurney et al., 2002; Rodenbeck et al., 2003; Baker et al., 2006a). These flux estimates are still highly uncertain in many regions due to sparse data coverage (Gurney et al., 2003). Satellite CO₂ measurements have the potential to help inverse modeling studies by improving the data constraint due to their global spatial sampling and sheer data volume. Previous studies have indicated that using spatially resolved, global measurements of the column-integrated dry air mole fraction (X_{CO_2}) with precisions of ~ 1 ppm will reduce the uncertainties in regional estimates of sources and sinks of atmospheric CO₂ (Rayner and O'Brien, 2001; Miller et al., 2007; Chevallier et al., 2007).

Two existing satellites, the Atmospheric Infrared Sounder (AIRS) and the SCanning Imaging Absorption spectroMeter for Atmospheric CHartographY (SCIAMACHY), provide information about CO₂ concentrations. AIRS, on the Aqua platform launched in May 2002, measures 2378 spectral channels in the infrared (IR) from 3.74 to 15.4 μm (Aumann et al., 2003). AIRS has a 1:30 AM/PM equator crossing time, nine 1.1° by 0.6° footprints in a single FOV, and scans $\pm 48.95^\circ$ from nadir, making 90 measurements per scan. A study by Engelen

et al. (2004) demonstrated the feasibility of global CO₂ estimation using AIRS data in a numerical weather prediction data assimilation system. Since AIRS measures IR radiances rather than reflected sunlight, it can be used to measure upper tropospheric-weighted CO₂ concentrations during the day and at night; however, atmospheric mixing makes the upper tropospheric CO₂ concentrations rather zonal, indicating that AIRS data can only inform about very broad features of the surface fluxes (Chevallier et al., 2005). SCIAMACHY, which embarked on board the European Space Agency (ESA) Envisat satellite in 2001, is a polar-orbiting nadir looking instrument that measures reflected sunlight in the UV, visible, and near IR regions from 240 to 2400 nm. SCIAMACHY has a 30 x 60 km² footprint that scans across a 960 km-wide swath and a 35 day repeat-cycle with global coverage in ~ 6 days. Studies by Houweling et al. (2004) and Buchwitz et al. (2005) indicate that SCIAMACHY measurements may be capable of detecting regional CO₂ surface sources/sinks regions; however, accurate SCIAMACHY CO₂ retrievals are limited to land regions due to low surface reflectivity over the ocean and are difficult because of calibration issues and spectral and spatial resolution (Houweling et al., 2004; Buchwitz et al., 2005).

Two satellites designed specifically to measure X_{CO_2} with ~ 0.3 - 0.5% (1-2 ppm) precision are scheduled to launch in late 2008: the Orbiting Carbon Observatory (OCO) (Crisp et al., 2004; Miller et al., 2007) and the Greenhouse gases Observing SATellite (GOSAT) (NIES, 2006). Both satellites will collect high-resolution spectra of reflected sunlight in the 0.76 μm O₂ A-band and the CO₂ bands at 1.61

μm and $2.06 \mu\text{m}$. A single sounding will consist of simultaneous observations from all three bands. OCO and GOSAT will fly in a polar sun-synchronous orbit to provide global coverage with an equator crossing time ~ 1300 LST. OCO will orbit just ahead of the Earth Observing System (EOS) Aqua platform in the A-train, which has a 16-day repeat cycle. To obtain an adequate number of soundings on regional scales even in the presence of patchy clouds, OCO will have a 10 km-wide cross-track field of view (FOV) that is divided into eight 1.25 km-wide samples with a 2.25 km down-track resolution at nadir. GOSAT will orbit at an altitude of 666 km with a 3-day recurrence. GOSAT is designed with cross-track pointing ability and will sample points with a variable width from 88 to 800 km.

CO₂ concentration fields retrieved from satellites will be used as inputs to synthesis inversion and data assimilation models to help reduce uncertainties in flux estimates; however, to utilize these measurements, care must be taken to sample the models following the satellite sampling strategy as closely as possible. Spatial representativeness errors may be introduced into inversions that compare CO₂ concentrations from a model grid column to satellite concentrations sampled over only a fraction of the domain. Local clear-sky errors may exist in inversions that compare concentrations in a grid column that may be partially cloudy to total-column CO₂ concentrations sampled at the same time but only over clear areas. Temporal sampling errors can result from comparing satellite measurements to temporally averaged concentrations. Incorrectly accounting for these errors could lead to errors in the flux estimates, particularly if they are biased. Spatially

coherent biases as small as 0.1 ppm will alter flux estimates and must be accounted for (Miller et al., 2007). Chevallier et al. (2007) simulated the impact of undetected biases and showed that regional biases of only a few tenths of a ppm in column averaged CO₂ can bias the inverted yearly sub-continental fluxes by a few tenths of a gigaton of carbon. To avoid incurring errors in inversions, the spatial, clear-sky, and temporal sampling errors need to be investigated and quantified.

Spatial representation errors are determined by the spatial variability: as horizontal spatial heterogeneity increases, observations characterize smaller areas and representation errors increase (Gerbig et al., 2004; Wofsy and Harriss, 2002). Gerbig et al. (2004) used aircraft data to investigate spatial representation errors of mixed layer averaged CO₂ mixing ratios and concluded that spatial representation errors reach 1-2 ppm for a typical 200-400 km horizontal resolution grid cell. Expanding on Gerbig's analysis, Lin et al. (2004) found column CO₂ spatial representation errors of $\sim 0.6 - 0.7$ ppm over North America and $\sim 0.2 - 0.3$ ppm over the Pacific Ocean. Consistent with the results from Lin et al. (2004), an analysis of regional X_{CO_2} variability using coarsely modeled ($5.5^\circ \times 5.5^\circ$) total column CO₂ shows that the spatial variability is smaller over oceans than over land and reveals that the spatial variability varies seasonally as well as geographically, with higher variability during the northern hemisphere summer and lower variability in winter (Miller et al., 2007).

Although studies have investigated the spatial variability and associated representation errors of total column CO₂, little research has been focused on clear-sky

and temporal representation errors. This study analyzes spatial, local clear-sky and temporal sampling errors using a cloud resolving, coupled ecosystem-atmosphere model, SiB2-RAMS. We performed simulations over a temperate forest region and a tropical region, and we investigated these errors for both fine ($\sim 1^\circ \times 1^\circ$) and coarse ($\sim 4^\circ \times 4^\circ$) grid columns by simulating CO_2 concentrations over these regions using explicit microphysics and grid-cell increments of 1 km and 5 km, respectively.

3.2 Methods

3.2.1 Model Description, SiB2-RAMS

The Simple Biosphere Model (SiB2) calculates the transfer of energy, mass, and momentum between the atmosphere and the vegetated surface of the earth (Sellers et al., 1996b,a). The coupled meteorological model is the Brazilian version of the Colorado State Regional Atmospheric Modeling System (RAMS) (Frietas et al., 2006). RAMS is a comprehensive mesoscale meteorological modeling system designed to simulate atmospheric circulations spanning in scale from hemispheric scales down to large eddy simulations of the planetary boundary layer (Pielke et al., 1992; Cotton et al., 2002). Details of the coupled model can be found in Denning et al. (2003); Nicholls et al. (2004); Lu et al. (2005); Wang et al. (2007).

This study focuses on two simulations, one in North America (NA) and one in South America (SA). Both simulations consist of four levels of nested grids down

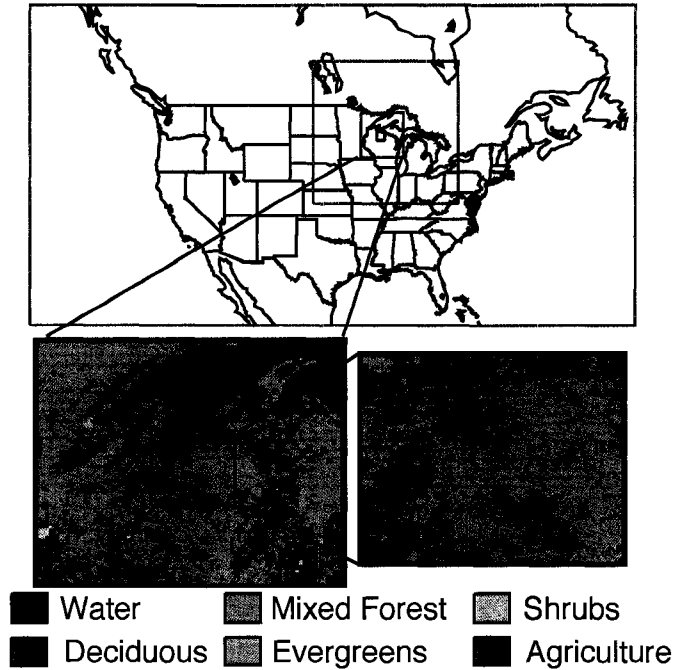


Figure 3.1: Grid setup over North America, with the nested grids outlined in red. The vegetation classifications for the coarse grid column (grid 3) and the fine grid column (grid 4) are shown in the bottom left and right images, respectively. The red cross indicates the location of the WLEF tower.

to a fine domain of 97 km by 97 km with a grid increment of 1 km (Figures 3.1 and 3.2). The NA simulation has 45 vertical levels extending up to 23.5 km, and the SA simulation has 32 vertical levels up to 24 km. To simulate cloud and precipitation processes explicitly, both simulations use the bulk microphysical parameterization in RAMS (Meyers et al., 1997; Walko et al., 1995). We use the Mellor and Yamada (1982) scheme for vertical diffusion, the Smagorinsky (1963) scheme for horizontal diffusion, and the two-stream radiation scheme developed by Harrington (1997). At the lateral boundaries we utilize the radiation condition discussed by Klemp and Wilhelmson (1978).

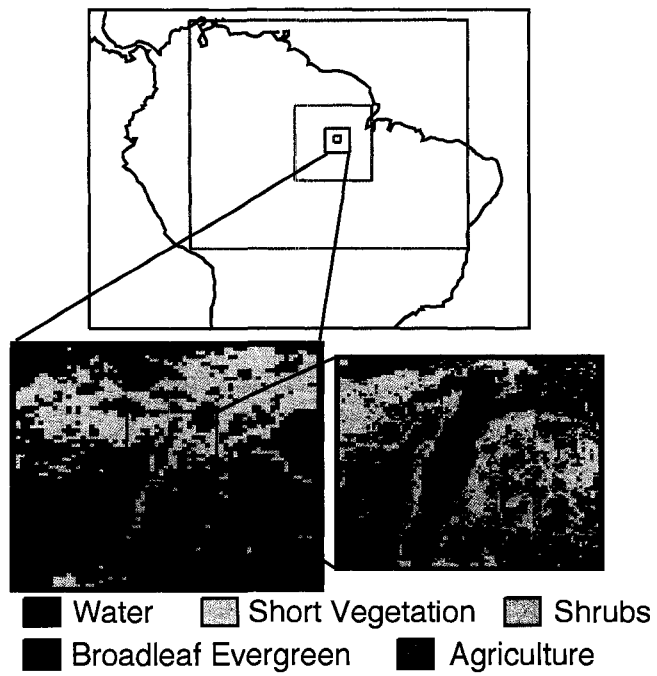


Figure 3.2: Grid setup in the South American simulation. The four grids in the simulation are outlined in red. The red cross displays the Tapajos Km 67 tower.

3.2.2 Input Data

The vegetation cover is derived from the 1-km AVHRR land cover classification data (Hansen et al., 2000), and this study used 1-km resolution Normalized Difference Vegetation Index (NDVI) data from SPOT-4 (Système Probatoire d’Observation de la Terre polar orbiting satellite; United States Department of Agriculture/Foreign Agriculture Service and Global Inventory Modeling and Mapping Studies). The meteorological fields in NA are initialized by and the lateral boundaries are nudged every three hours by the National Center for Environmental Prediction (NCEP) mesoscale Eta-212 grid reanalysis with 40-km horizontal resolution (AWIPS 40-km). The SA simulation is initialized and driven by 6-hourly lateral boundary conditions derived from Centro de Previsao de Tempo e Estudos Climaticos (CPTEC) analysis products.

Surface carbon fluxes due to fossil fuel combustion, cement production, and gas flaring are prescribed from the 1995 CO₂ emission estimates of Andres et al. (1996), with a 1.112 scaling factor applied to adjust the strength for August 2001 (Marland et al., 2005; Wang et al., 2007). The air-sea CO₂ fluxes are the monthly 1995 estimates from Takahashi et al. (2002). The initial CO₂ field and the lateral boundaries in SiB2-RAMS are set to 370 ppm for NA and 360 ppm for SA. A more detailed description of the input data and initialization can be found in Wang et al. (2007) and Lu et al. (2005) for NA and SA, respectively.

3.2.3 Case Descriptions

The NA simulation was centered on the WLEF tower in Wisconsin (Figure 3.1) (see Davis et al. (2003); Bakwin et al. (1998); Ricciuto et al. (2007) for a description of the site and measurements). We analyzed the third grid (lower left panel of Figure 3.1), which will be referred to as the coarse grid column and the fourth grid (lower right panel), which we denote as the fine grid column. The coarse grid column was 450 km by 450 km with a 5 km grid increment. The northeastern portion of the domain included Lake Superior, the upper and middle regions were dominated by mixed forest, and the southern third contained significant areas of agriculture and cropland. The fine grid column, which was 97 km x 97 km with a 1 km grid increment, was primarily mixed forest and broadleaf deciduous trees with a few patches of evergreens. This grid had several small lakes, with one of the larger lakes just north of the WLEF tower.

This case ran from 0000 UT August 11 to 0000 UT August 21, 2001. During this ten-day time period, three cold fronts passed over the WLEF tower. The first simulated front passed at 0200 local standard time (LST) on August 12, the second front passed at 2300 LST the night of the 15th, and the third front passed over the tower at 1800 LST on August 17th. During the simulation, the wind was light and southwesterly except during the frontal passages, when the wind strengthened and rotated clockwise to northerly flow. For a more complete description of this case and the meteorological conditions, see Wang et al. (2007).

This ten-day time period was chosen to capture the front on August 15-16, which caused the most significant CO₂ concentration variation seen at the WLEF tower that summer. Investigating the representation errors over a time period when the concentration at 396 m varied by more than 40 ppm in 36-hours provides an estimate of the errors during a significant synoptic event. Since the simulation is characterized by considerable CO₂ variability, the error estimates from this case are likely to be the maximum errors associated with this site.

The simulation in SA was centered over the Tapajos River in Brazil (Figure 3.2), and ran from 0000 UT August 1 to 0000 UT August 16, 2001. Similar to the NA case, we analyzed the third (lower left panel of Figure 3.2) and fourth (lower right panel) grids, denoted as the coarse and fine grid columns, respectively. The coarse column was 335 km by 335 km with a 5-km grid increment. The Tapajos River flowed northward through the center of the domain, and the region was covered primarily by broadleaf evergreen forest and short vegetation, which consisted of pasture and mixed farming. The fine domain was 97 x 97 km, with a 1-km grid increment. The dominant land type for this region was pasture and mixed farming, inland water comprised $\sim 30\%$ of the domain, and the remaining vegetation was broadleaf evergreen forest. On the east side of the Tapajos River, the Km-67 eddy covariance flux tower measured heat, moisture and trace gas fluxes, CO₂ concentrations, and radiation profiles (Saleska et al., 2003). This case occurred during the dry season and was characterized by calm conditions without fronts or squall lines. During the simulation, intense trade winds blew almost constantly,

little precipitation fell over most of the domain, and the clouds were predominantly cumulus. Lu et al. (2005) provide a further discussion of this simulation.

The unique physical setting of the SA case with respect to the topography and the Tapajos River produces a unique mesoscale and micrometeorological environment (Lu et al., 2005). This time-period was chosen to avoid squall lines and organized weather patterns, highlighting CO₂ variability due to the heterogeneous river and vegetation cover and mesoscale circulations. Analyzing this simulation will provide estimates of the representation errors expected from water-vegetation interactions including a low-level convergence line. The error estimates from this simulation represent estimates from local circulation patterns rather than from large-scale features, and these errors provide the expected maximum error of CO₂ due to surface heterogeneity.

3.2.4 Model Evaluation

The two simulations analyzed in this study are evaluated against observations in complementary publications. Wang et al. (2007) focused on the August 15 frontal passage in the North American simulation to analyze the impact of fronts and synoptic events on the CO₂ concentration. A high CO₂ air mass built up in the southern Great Plains on August 14-15 because of the slow photosynthesis rate caused by hot and dry air over Oklahoma and Texas and strong nighttime respiration in the southeast. This air mass traveled north and was primarily responsible for the high concentrations just prior to the front on August 15, although weak

local photosynthesis on August 15 and strong nighttime respiration under overcast sky conditions also contributed to the accumulation of CO₂. Wang et al. (2007) concluded that the atmospheric CO₂ variations during this time period were dominated by coherent regional anomalies that were advected by synoptic-scale systems. In the study, Wang et al. (2007) compared the near-surface meteorological fields between observations and SiB2-RAMS for the period 11 August 2001 through 20 August 2001, including evaluations of temperature, water vapor mixing ratio, wind speed, wind direction, net ecosystem exchange (NEE), and CO₂ concentration anomalies.

Lu et al. (2005) analyzed the SA simulation depicted here to investigate mesoscale circulations and atmospheric CO₂ variations over a heterogeneous landscape during the Santarem Mesoscale Campaign (SMC) of August 2001. They evaluated the modeled CO₂ concentrations and fluxes, sensible and latent heat fluxes, temperature, and winds compared to observations, showing that the model captured the temperatures, winds, NEE, and daytime CO₂ concentrations reasonably well. Lu et al. (2005) found that the topography, the differences in roughness length between water and land, the juxtaposition of the Amazon and Tapajos Rivers, and the resulting horizontal and vertical wind shears all facilitated the generation of local mesoscale circulations and a low-level convergence line.

To evaluate the effect of clouds on the carbon flux and CO₂ concentration, we compared modeled NEE and CO₂ to the observations sampled at the towers located in the domains (see section 3.2.3 for the tower descriptions). For the NA

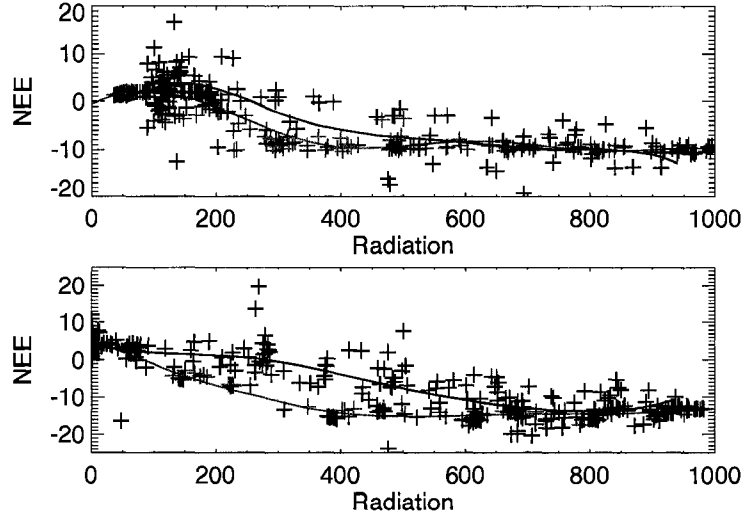


Figure 3.3: Observed (solid) and modeled (shaded, sampled from the grid cells including the towers) NEE, in $\mu\text{mol m}^{-2} \text{s}^{-1}$, versus radiation, in W m^{-2} . Evaluation at NA (top) and results from SA (bottom). For NA, the radiation includes longwave, and the values have been subtracted by 200 W m^{-2} for easier comparison. The SA radiation is shortwave only. A two-harmonic fit to each time series has been overlaid. Mean NA and SA model/data NEE values for radiation $> 650 \text{ W m}^{-2}$ are $-9.7/-10.1$ and $-13.8/-13.1 \mu\text{mol m}^{-2} \text{s}^{-1}$, respectively. For moderate radiation values between 300 and 650 W m^{-2} the resulting NA and SA model/data NEE means are $-8.5/-6.7$ and $-14.9/-7.3$, respectively. Finally, for radiation $< 300 \text{ W m}^{-2}$ the NA and SA model/data NEE mean values are $0.2/2.8$ and $-4.2/2.3 \mu\text{mol m}^{-2} \text{s}^{-1}$, respectively.

case, we sampled the model at the WLEF tower location and compared hourly net radiation, CO_2 concentrations at 396 m , and NEE over the 10-day simulation to the corresponding hourly observations at the WLEF tower. We performed a similar comparison for the SA simulation: we sampled the model at the location of the Km-67 tower and compared the modeled shortwave radiation, the CO_2 concentration sampled at 60 m , and NEE over the simulation to the corresponding hourly data sampled at the flux tower.

To investigate the response of the carbon flux to various cloud conditions, we compared the modeled and observed NEE to incoming radiation and overlaid a 2-harmonic function fit to both the model output and the tower observations (Figure 3.3). At both locations for conditions with radiation values higher than 650 W m^{-2} , which corresponds primarily to clear or mostly clear conditions, the fits to both the model and the in situ observations have a constant uptake of $\sim 10 \mu\text{mol m}^{-2} \text{ s}^{-1}$ and $\sim 13.5 \mu\text{mol m}^{-2} \text{ s}^{-1}$ for NA and SA, respectively. As the radiation decreases from 650 W m^{-2} the carbon uptake also decreases; however, the observed decrease occurs at higher radiation values than the modeled decrease. Simulated uptake remains relatively constant until the radiation decreases to $\sim 400 \text{ W m}^{-2}$, while the observed uptake has a higher light saturation and thus begins decreasing at higher radiation values. SiB2.5 calculates photosynthesis for a single sun-leaf and uses an empirical adjustment to extinction law in conjunction with satellite information to adjust carbon flux up to canopy scale (Baker et al., 2005). Using this technique is known to result in model photosynthesis reaching light saturation too soon, resulting in enhanced uptake for moderate radiation values (e.g. Dai et al., 2003; Dickinson et al., 1998). The enhanced uptake in the model could decrease the surface CO_2 concentrations during moderately cloudy to overcast conditions and just after sunrise and before sunset.

To investigate the relationship between cloud cover and CO_2 concentrations, we compared modeled and observed CO_2 concentrations to the corresponding radiation (Figure 3.4). Since the CO_2 concentration in the model has a prescribed

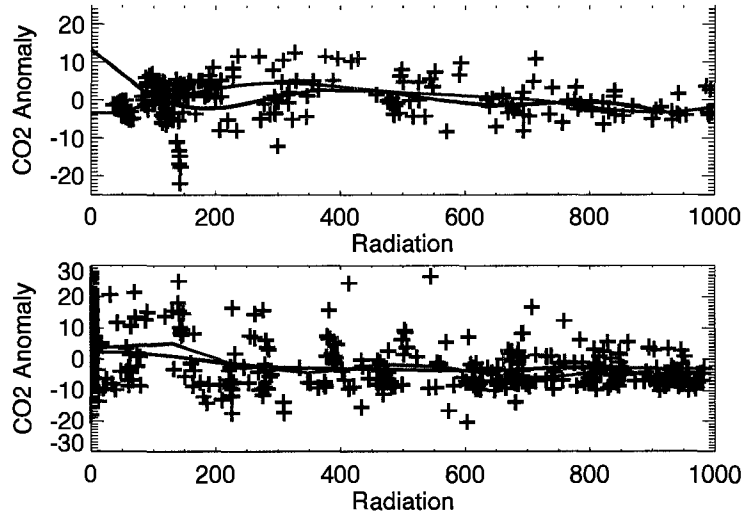


Figure 3.4: Observed (black) and modeled (grey, sampled from the grid cells including the towers) CO₂ anomalies (ppm) versus radiation (W m⁻²). NA results (top) and SA results (bottom). The anomalies are calculated by subtracting the mean CO₂ concentration over each case from the corresponding series. Mean NA and SA model/data CO₂ values for radiation > 650 W m⁻² are -1.6/-1.1 and -4.3/-3.1 ppm, respectively. For moderate radiation values between 300 and 650 W m⁻² the resulting NA and SA model/data CO₂ mean anomalies are 3.5/1.6 and -2.9/-4.0 ppm, respectively. Finally, for radiation < 300 W m⁻² the NA and SA model/data CO₂ mean values are -0.4/-0.2 and 0.7/1.9 ppm, respectively.

background, we compared the concentration anomalies, which are calculated by subtracting the mean of the CO₂ concentrations during the simulated time period from the data sets. In both NA and SA, the variability of the CO₂ concentration increases with decreasing radiation, and this characteristic is seen in both the model and the observations. For clear-sky conditions with radiation values above 650 W m⁻², the concentrations are lower than the mean. Over NA, the concentrations are highest for moderate radiation (between 650 and 300 W m⁻²), while over SA the concentrations increase as radiation decreases. Despite the model having enhanced uptake for moderate to low radiation, the mean values for these radiation bins remain within ~ 1 ppm. The relatively small differences between the modeled and observed concentrations indicate that the model does a reasonable job of capturing the overall behavior of the CO₂ concentration in various sky conditions.

3.2.5 Simulating Satellite Measurements Using SiB2-RAMS Output

To simulate satellite CO₂ retrievals over the two simulations, we mimic the OCO sampling strategy. Since OCO will estimate total column CO₂ concentrations, the modeled concentrations are vertically integrated by pressure weighting using a standard atmosphere. All simulated tracks are sampled at 1300 LST to approximate the satellite overpass time. Since we are investigating small domains that satellites will fly over very quickly, we assume that OCO travels due north and that all the footprints in a track will be averaged together to yield only one

concentration for the grid. We created a track width of 10 km by averaging the appropriate number of pixels in the x-direction, which corresponds to 10 pixels for the fine domain and 2 pixels for the coarse domain. To create one satellite value for each possible track, we meridionally averaged the pixels to create a single measurement. Using these criteria, the fine domains have 88 different possible satellite tracks: the first track is on the western edge of the domain ($x=1:10$), the second track is one pixel eastward ($x=2:11$), and the final track is along the eastern edge ($x=88:97$). The coarse domain in NA has 87 different tracks, and the SA coarse domain has 65 possible satellite tracks.

Since the satellite retrieval requires clear conditions, only pixels with clear-sky are included in the simulated satellite concentrations (unless otherwise specified). A pixel is considered clear if the cloud optical depth $\tau < 0.2$. This threshold was selected as it is the approximate threshold for which precise X_{CO_2} retrievals are possible (Miller et al., 2007; Crisp et al., 2004). In the NA simulation, two days are primarily clear, five days are partly cloudy, and two days are overcast. Over SA, six days are completely clear and nine days are partly cloudy.

3.3 Results

3.3.1 Total Column CO₂ Concentrations

In the NA simulation, the main driver of total column CO₂ temporal variability is synoptic scale systems (Figure 3.5). A Fourier analysis of the CO₂ concentrations

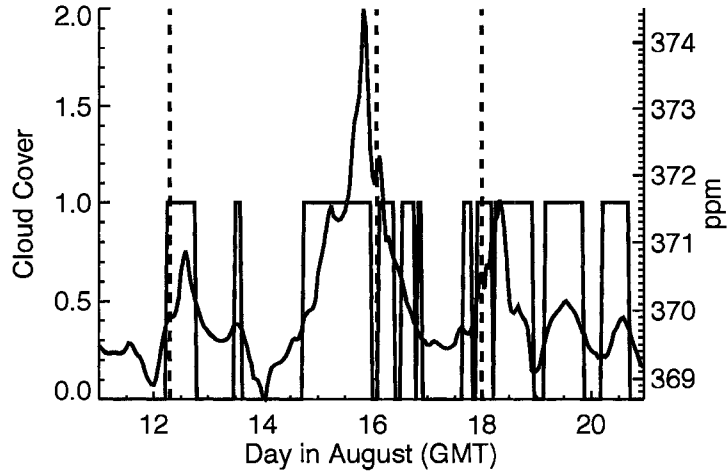


Figure 3.5: Simulated total column CO_2 concentrations at the WLEF tower (black line) and the sky conditions (grey line), where 0 indicates clear sky and 1 indicates the tower was cloud covered. The vertical dashed lines indicate the three frontal passages.

reveals a significant spectral peak at ~ 3.5 days (at the 95% confidence level using an F test), which indicates the dominant timescale of variability is the fronts in the simulation. The diurnal cycle also has a significant spectral peak, although it is much smaller. Rather than displaying a strong diurnal cycle, the simulated total column concentration sampled from the grid cell that includes the WLEF tower has three spikes associated with the three frontal passages. The column CO_2 range is ~ 6 ppm and the standard deviation is ~ 1 ppm. The fronts, which are associated with clouds, advect high concentrations from the southwest, where a heat wave reduces carbon uptake causing high CO_2 anomalies (Wang et al., 2007). The lowest concentrations during the simulation occur in clear conditions, when the main influence on CO_2 is the local vegetation rather than advection.

The NA total column CO₂ spatial variability is also predominantly affected by the weather via the frontal passages. The range of column CO₂ at 1300 LST over the fine grid column varies from 0.2 to 1.8 ppm, with an average of 0.8 ppm (Table 3.1). Over the coarse grid column, the CO₂ range at 1300 LST varies from 1 ppm to 13.7 ppm, with an average range of 3.5 ppm across the domain and a mean standard deviation of 0.6 ppm. Although the surface heterogeneity of the coarse domain contributes to increased CO₂ variability, the greatest concentration ranges occur when the southwestern portion of the domain has high concentrations from advection while the northeastern half of the domain has low concentrations. Optically thick clouds that are associated with the fronts contribute to higher concentrations by reducing photosynthesis due to light-limitation.

	Range	σ
	Mean/Max	Mean/Max
NA fine	0.76/1.81	0.15/0.4
NA coarse	3.53/13.71	0.64/1.9
SA fine	1.46/2.1	0.4/0.53
SA coarse	2.15/2.91	0.44/0.58

Table 3.1: Range and Standard Deviation (σ) of the Simulated Grid Columns at 1300 LST. Both the mean values over the entire simulation and the maximum values are displayed. Units are in ppm.

Ground-based measurements of total column CO₂ are being made at the WLEF tall tower site (Washenfelder et al., 2006). The observatory utilizes a similar technique as OCO, GOSAT, and SCIAMACHY to measure X_{CO₂} using an upward looking Fourier Transform Spectrometer (FTS). The observatory has been measuring X_{CO₂} since May 2004. At WLEF, X_{CO₂} is minimally influenced by the

diurnal rectifier effect. Washenfelder et al. (2006) present results from a validation study involving aircraft data where column observations were measured on five dates in July and August of 2004. The column-average concentration varies ~ 7 ppm between these samples, which is similar in magnitude to the column variations seen in the SiB-RAMS simulations due to the frontal passages. A plot of the seasonal cycle of daytime daily averaged X_{CO_2} shows day-to-day variability of $\sim 6-7$ ppm during the summer (Washenfelder et al., 2006).

The dominant cause of column CO_2 temporal variability in SA is the diurnal cycle and mesoscale circulations (Figure 3.6), since this simulation occurs in the dry season and is characterized by steady trade winds, nocturnal decoupling, river breezes, boundary layer cumulus clouds, and no airmasses or fronts. A power spectrum of this series shows the only significant spectral peak is at 1 day. The temporal CO_2 variability in SA is smaller than in NA, as the range and standard deviation of the simulated column concentrations sampled at the Tapajos tower is only 3.1 ppm and 0.7 ppm, respectively. The amplitude of the mean diurnal cycle is 1.1 ppm. Unlike in NA, there is no correlation between cloud cover and mixing ratios. Since this simulation was selected to isolate the influence of local vegetation and circulations, the clouds are mid-afternoon cumulus clouds primarily seen on the east bank of the Tapajos River due to the low-level convergence line (Lu et al., 2005).

Since the SA case has significant surface heterogeneity due to the rivers, the spatial variability in this simulation is larger for the fine grid column compared

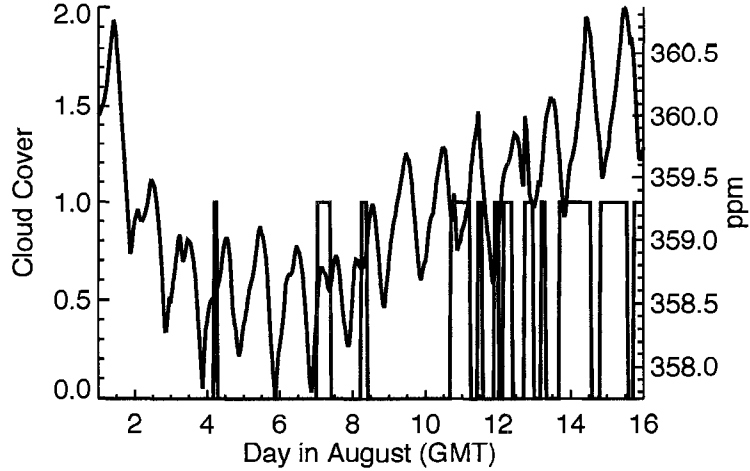


Figure 3.6: Simulated total column CO₂ concentrations at the Tapajos tower (solid line) and the modeled sky conditions (shaded line), where 0 indicates clear-sky and 1 indicates the tower was cloud covered.

to the NA simulation; however, the spatial variability over the coarse domain is smaller, which is due to the lack of synoptic-scale features which advected high CO₂ in NA. The average total column spatial range at 1300 LST is 1.46 ppm and 2.15 ppm for the fine and coarse grid columns, respectively (Table 3.1). The CO₂ spatial pattern at 1300 LST was similar for all days, with a low concentration on the eastern half of the domain and higher concentrations in the northwest corner, which is primarily due to the topography and surface cover (Lu et al., 2005).

The total column measurements in SiB-RAMS are consistent with results presented by Olsen and Randerson (2004). Using the Model of Atmospheric Transport and Chemistry (MATCH) three-dimensional atmospheric transport model, Olsen and Randerson (2004) investigated the total column CO₂ concentrations. They found that at WLEF the greatest variability of column CO₂ was linked to syn-

optic events on the order of 2 to 6 days. In order to influence the column, CO₂ flux anomalies had to accumulate in the lower troposphere over a period of several days or there had to be a large-scale replacement of air in the column. Day-to-day variations of up to ~ 8 ppm can be seen at the WLEF tower during the summer due to synoptic events. Similar to SiB-RAMS, results from Olsen and Randerson (2004) show the main driver of column CO₂ variability over WLEF during the summer is synoptic scale systems, as mid-latitude air-masses with distinct CO₂ concentrations develop in response to surface fluxes and are separated by fronts (Parazoo et al., 2008).

In the Amazon, modeled vertical CO₂ profiles were qualitatively similar to the observed profiles near the surface, but did not exhibit the same degree of variability (Olsen and Randerson, 2004). The amplitude of the average diurnal cycle within the Amazon basin was 0.9 ppm in July, which is slightly weaker than the diurnal cycle from SiB-RAMS; however, comparison of MATCH column CO₂ to column CO₂ profiles from aircraft data revealed that MATCH tended to have lower diurnal variability than observed. In the tropics, the dominant cause of CO₂ variability is the diurnal cycle due to the productive ecosystems and the lack of synoptic-scale features.

3.3.2 Spatial Representation Errors

Since satellite track widths are not the same size as an inverse model grid column, using satellite concentrations to optimize a grid column may introduce spatial rep-

representativeness errors into the inversion. In this study, the size of the coarse and fine domains in both NA and SA correspond roughly to a global model grid size. We calculated the spatial errors that inversions would incur from using satellite measurements to represent grid columns in central NA and in the Amazon by subtracting the domain-averaged 1300 LST total column concentrations from the simulated satellite concentrations, which use only clear-sky pixels. The daily results are compiled into a single sampling distribution for each domain and location (Figure 3.7). The mean and standard deviation of the sampling distributions for the fine and coarse domains for both NA and SA are provided in Table 3.2.

	Spatial μ/σ	Local Clear-Sky μ/σ	Diurnal μ/σ	Temporal μ/σ
NA fine	-0.01/0.06	-0.02/0.06	-0.19/0.33	-0.44/0.31
NA coarse	-0.13/0.43	-0.12/0.51	-0.25/0.51	-0.42/0.5
SA fine	-0.04/0.21	-0.04/0.18	0.1/0.26	0.06/0.66
SA coarse	-0.04/0.24	-0.03/0.19	0./0.25	-0.01/0.64

Table 3.2: Mean (μ) and Standard Deviation (σ) of the Sampling Distributions of the Spatial Representation Errors, the Local Clear-Sky Errors, the Diurnal Sampling Errors, and the Temporal Sampling Errors for All Four Cases. Units are in ppm.

The spatial errors for both fine grid columns are unbiased, as the mean of the distributions are close to 0. Over NA, all of the errors are within 0.3 ppm; however, over SA only 13% of the simulated satellite concentrations were within 0.3 ppm of the mean. The standard deviation for SA is 0.2 ppm and the maximum error is -0.72 ppm. 97% of the simulated SA tracks are within 0.5 ppm, which is only half of the expected spectroscopic retrieval error (Miller et al., 2007). The larger

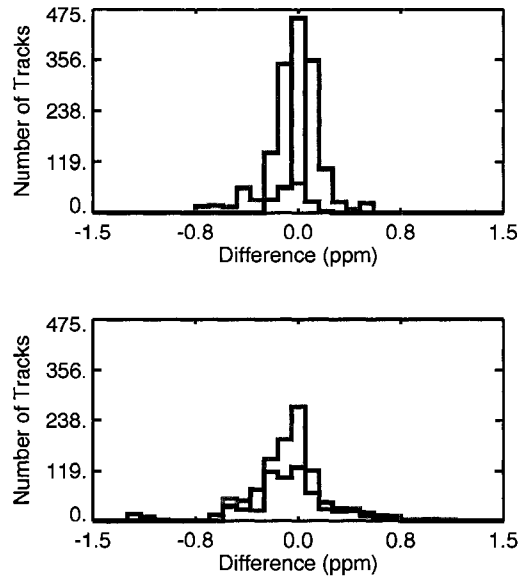


Figure 3.7: Sampling distributions of the spatial representativeness errors in NA (solid) and SA (shaded) at 1300 LST compiled from all days of the simulations. The x axis is the difference between the simulated satellite concentration and the domain mean concentration, and the y axis is the number of satellite tracks that correspond to each difference. Negative values indicate an underestimation by the simulated satellite measurements and positive values indicate an overestimation. Results from the fine grid columns (top) and distribution of the errors from the coarse grid columns (bottom).

errors over SA are due to the heterogeneity in that domain and cloud masking in NA, since the greatest NA variability occurred when there were clouds and hence no satellite retrievals. The relatively small magnitude of the errors is due to the limited total column CO₂ variability in the domains.

The errors that would be introduced into inversions that use satellite measurements to represent coarse grid columns are larger than the errors for a fine grid column, which is not surprising since the total column CO₂ is more variable. The spatial errors over SA remain unbiased and have a standard deviation similar to that of the fine domain. 95% of the satellite tracks capture the domain mean within 0.5 ppm. The errors for the NA coarse domain are much larger and negatively biased, with a mean of -0.13 ppm and a standard deviation of 0.43 ppm. Although nearly 25% of the tracks are within 0.1 of the mean, 18% of the tracks have errors larger than 0.5 ppm and 6% of the tracks have errors larger than 1 ppm, which is larger than the expected retrieval error. The large and negatively biased spatial errors are due to the large gradients of CO₂ due to the frontal passages and the cloud masking of the higher concentrations associated with the fronts.

3.3.3 Local Clear-Sky Errors

We define local clear-sky errors as errors that are introduced into inversions that use clear-sky satellite concentrations to represent a transport model grid column that includes clouds. These errors are calculated by subtracting the simulated satellite concentrations at 1300 LST using all pixels from the simulated satellite

concentrations using only clear-sky pixels. The resulting errors are smaller than the retrieval error and are unbiased for the fine domains (Figure 3.8). All the NA satellite tracks over the fine grid column that only use clear-sky footprints capture the true mean track value within 0.3 ppm. For the SA case, the standard deviation is larger and 87% of the tracks are within 0.3 ppm of the true mean. The largest error is 0.7 ppm. The SA coarse domain errors are very similar to the errors in the fine domain, with 85% of the errors less than 0.3 ppm. The similarity between the fine and coarse sampling distributions indicates that differences in carbon uptake due to local cloud-cover has a minimal impact on the concentration at a single snapshot in time. The local clear-sky errors over the NA coarse grid column are negatively biased with a sampling distribution mean of -0.12 ppm. The negative bias is due to a few tracks that have large negative errors. Although 80% of the simulated satellite concentrations using only clear footprints have errors less than 0.3 ppm, 3% of the tracks have errors greater than 1 ppm, with errors as large as 4 ppm. Similar to the spatial errors, large and negatively biased local clear-sky errors are due to cloud masking of high frontal CO₂.

To further examine the clear-sky errors, we analyzed local clear minus all-sky differences in net ecosystem exchange (NEE), which were calculated in a similar manner by subtracting the mean NEE value in a satellite track containing all pixels from the corresponding satellite track NEE mean utilizing only clear-sky pixels. The resulting errors are very small ($< 1 \mu\text{mol m}^{-2} \text{s}^{-1}$). For the fine domains, the errors are shifted towards enhanced uptake in clear conditions due

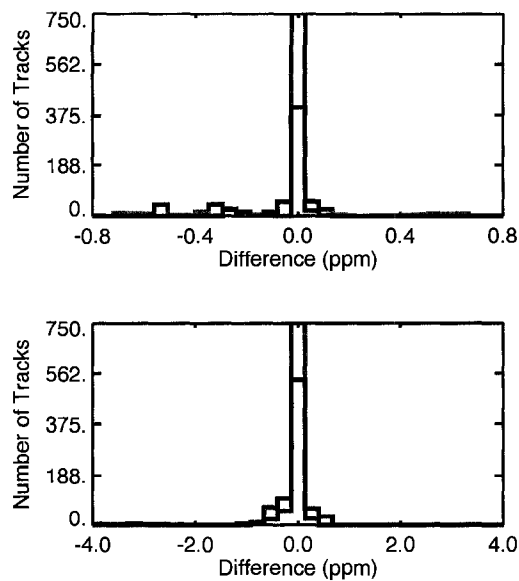


Figure 3.8: Local clear-sky total column CO₂ errors for NA (solid) and SA (shaded), which are the differences between the simulated satellite concentrations at 1300 LST using only clear-sky pixels and the simulated satellite concentrations at the same time using all the pixels in the satellite track. Errors from the fine grid (top) and results from the coarse grid (bottom).

to reduced photosynthesis under clouds; however, the errors in the coarse domains are symmetrical about 0. Since the clear-sky NEE errors are small, their effect on the column CO₂ concentration is minimal, indicating that the main driver of the large errors seen in the clear-sky CO₂ is the organization of regional CO₂ gradients along frontal boundaries, which are masked by large-scale cloud systems and not observed by satellites.

3.3.4 Temporal Sampling Errors

Temporal sampling errors can occur in inversions that use satellite concentrations to optimize temporally-averaged concentrations in the model. We calculate temporal errors from using satellite measurements to represent diurnal averages and bi-monthly averages.

Diurnal Sampling Errors

To calculate the diurnal errors, we subtracted the domain-average diurnal mean (0000 UT to 0000 UT) from the simulated 1300 LST satellite tracks (Figure 3.9). All the standard deviations for the diurnal errors are larger than the standard deviations seen for both spatial and local clear-sky errors. Over SA, the mean of the sampling distribution is positively biased by a tenth of a ppm, and the entire distribution is positively shifted, indicating that on a fine domain satellite concentrations at 1300 LST are slightly higher than the domain mean. 94% of the simulated satellite tracks have errors less than 0.5 ppm, and all the tracks have

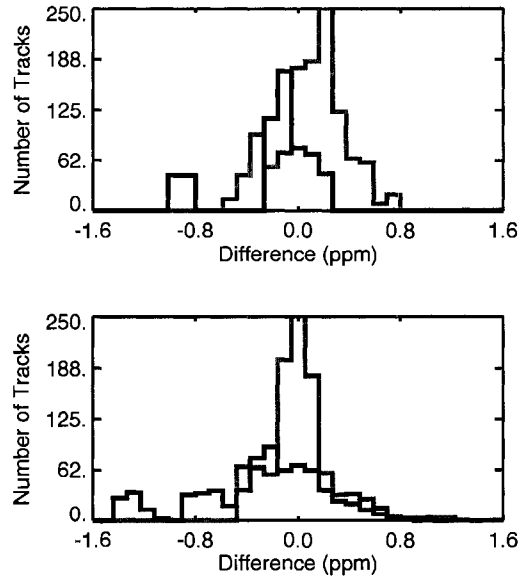


Figure 3.9: Diurnal sampling errors for NA (solid) and SA (shaded), which are the differences between the simulated satellite concentrations from each track using only clear-sky pixels and the diurnal mean CO₂ concentration from the entire domain, from 0000 to 0000 UT.

representation errors less than the expected retrieval error. For the SA coarse grid column, the diurnal errors are unbiased, the sampling distribution is symmetric about 0, and 95% of the errors are less than 0.5 ppm. The errors indicate that, in the absence of synoptic systems, 1300 LST satellite measurements over productive ecosystems are generally within 0.5 ppm of the diurnal mean and actually become less biased as the domain size increases. This result is similar to results from Olsen and Randerson (2004) and Miller et al. (2007) that indicate that column measurements over productive ecosystems have a diurnal maximum in the early morning, a minimum in the late afternoon, and are near the diurnal mean at 1300 LST.

The diurnal sampling errors for NA are negatively biased by ~ 0.2 ppm for both the coarse and the fine grid columns, indicating that sampling at 1300 LST underestimates the diurnal average for this case. Over the fine domain, 85% of the tracks capture the diurnal average within 0.5 ppm. The remaining tracks underestimate the mean by ~ 1 ppm. Since the total column concentration over the domain is driven by synoptic variability associated with cloud cover rather than the diurnal cycle due to vegetation, the large errors are idiosyncratic, resulting both from clouds masking the high concentrations and the timing of the fronts. The bias and standard deviations on the NA coarse domain is even larger. Rather than having a small subset of tracks underestimating the diurnal mean, the distribution is negatively shifted. Only 65% of the tracks have errors less than 0.5 ppm, indicating that over regions that have large synoptic variability the diurnal mean is not well sampled with a clear-sky satellite measurement taken at a single snapshot in time.

Bi-Monthly Sampling Errors

We calculated temporal sampling errors from comparing satellite concentrations to a domain-average bi-monthly mean by subtracting the domain-averaged CO₂ mean for the entire simulation from the 1300 LST satellite tracks (Figure 3.10). These errors are very large for all cases, as evidenced by the large standard deviations. The errors are biased by -0.4 ppm over NA. The NA sampling distributions for

both the fine and coarse domain are negatively shifted, showing that the clear-sky simulated satellite concentrations systematically underestimate the temporal average. Over the both domains in NA only $\sim 50\%$ of the tracks had errors less than 0.5 ppm. The large positive errors seen by a few tracks in the large domain is a result of the satellite concentrations sampled on the August 15, as a few pixels in the northwest corner of the domain were clear just prior to the frontal passage as the CO_2 concentration was increasing. Sampling between clouds enabled the satellite to observe higher concentrations associated with the front, but the front caused such a large anomaly in column CO_2 that the concentrations were actually higher than the domain-averaged temporal mean. At synoptic scales, horizontal and vertical mixing work together to cause these strong CO_2 variations along cold fronts (Parazoo et al., 2008). Since synoptic weather patterns can carry large CO_2 anomalies and since these weather disturbances and frontal passages are associated with clouds, clear-sky satellite measurements have large errors compared to temporal averages over regions with synoptic variability.

Over SA the standard deviation is also large for bi-monthly errors; however, the sampling distributions are unbiased. Even in a case driven by local vegetation and circulation, a substantial number of simulated satellite tracks have errors larger than 1 ppm. On the fine domain, only 40% of the tracks have errors less than 0.5 ppm, and only 45% of the simulated satellite concentrations have errors less than 0.5 ppm on the coarse domain. The large errors indicate that even in conditions dominated by local fluxes and circulation patterns, clear-sky satellite

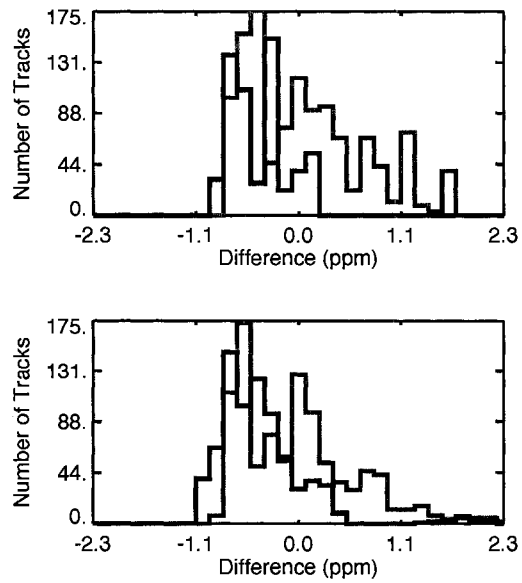


Figure 3.10: Temporal sampling errors for NA (solid) and SA (shaded), which are the differences between the simulated satellite concentrations from each track using only clear-sky pixels and the 10-d domain average. Fine grid column (top) and coarse grid column (bottom) results.

measurements sampled at 1300 LST cannot represent bi-monthly temporal averages without a substantial chance of introducing large errors.

3.4 Conclusions

Using a coupled ecosystem-atmosphere cloud-resolving model, we investigated sampling errors that may be introduced into inversions that use satellite retrievals of total column CO₂ in clear conditions. We analyzed two simulations: one over the mid-continental United States and one in the Brazilian Amazon. The main driver of column CO₂ variability in the NA case was synoptic systems associated with cloud cover, while the source of CO₂ variability in SA was the diurnal cycle and mesoscale circulations.

Spatial representation errors were unbiased and less than 0.5 ppm for a 100 x 100 km domain; however, the errors increased in the NA case when a single satellite track was used to represent a coarse (450 x 450 km) grid column. The local clear-sky errors exhibited the same patterns as the spatial errors: the majority of the errors were < 0.3 ppm for a 100 x 100 km domain, but the errors became negatively biased and large (> 2 ppm) for the coarse grid column of the NA simulation. Both the spatial and local clear-sky errors did not increase over the coarse SA grid column, where the variability was due to surface heterogeneity and local circulations. The main cause of large and biased spatial and clear-sky errors was not surface heterogeneity but rather synoptic systems associated with

cloud cover. CO₂ observations across North America showed large day-to-day CO₂ variations associated with passing weather disturbances manifested as surface cold fronts (Parazoo et al., 2008). Parazoo et al. (2008) found that although ecosystem response to frontal weather played a role, the majority of the CO₂ variations (70-90%) along fronts was due to horizontal and vertical mixing. Resulting strong coherent CO₂ patterns were then transported across the continent by horizontal advection. Since frontal systems create large gradients of CO₂ that are masked by clouds and cannot be sampled, inversions that use satellite measurements to represent coarse regions may incur large and biased spatial and local clear-sky errors. As inversions are influenced by a bias as small as a tenth of a ppm in the total column (Chevallier et al., 2007; Miller et al., 2007), satellite concentrations cannot be used to represent large regions with significant CO₂ variability due to synoptic systems. Our analysis suggests that transport models should be run at high resolution to avoid introducing biases.

Using satellite measurements to represent bi-monthly temporal averages created large and biased errors. Even in a location where the main temporal variability was due to the diurnal cycle and local circulations, the bi-monthly errors were larger than the expected retrieval error. Over NA, the errors were substantially negatively biased (~ -0.4 ppm) for both a fine and coarse grid column. Frontal systems that created CO₂ gradients and that could not be sampled due to cloud cover caused not only errors larger than the expected spectroscopic retrieval error, but sampling biases. Since sampling biases are harmful to inversions, satellite

measurements cannot be used to represent temporal averages. As our case study chose the synoptic event with the strongest CO₂ signal, the errors presented here are likely maximum error estimates; however, it is likely that biases will exist for all synoptic systems that are associated with clouds. In addition, the model overestimated the photosynthetic uptake for moderate radiation values, which could cause the role of large-scale advection relative to local changes in carbon flux to be overestimated. However, decreasing the uptake would increase the concentrations in cloudy conditions not visible by the satellite and would thus increase the negative bias in NA, making the results presented here robust despite this model deficiency.

Systematic variations of CO₂ along mid-latitude fronts makes model transport a priority. The model and the atmosphere must be sampled consistently, and observation operators in inversions must be accurate, including precise modeling of winds, clouds, fronts, and frontal timing. To avoid temporal sampling errors and biases, atmospheric transport must be modeled accurately and satellite mixing ratios must be used to optimize modeled concentrations sampled at the same time.

Acknowledgements

We thank Drs. Pedro Silva Dias, Maria Assunco Silva Dias, and Saulo Freitas for their SiB2-RAMS coupling work. Flux measurements at the WLEF tower were supported by the Department of Energy's Office of Science (BER) through the

National Institutes for Global Environmental Change and the Terrestrial Carbon Processes program. The carbon dioxide mixing ratio measurements at the WLEF tower are maintained by the National Oceanographic and Atmospheric Administration. Flux and CO₂ data in South America were supported by the National Aeronautics and Space Administration (NASA) grant NCC5-684. We thank Kenneth Davis for the data from the WLEF tower and Steven Wofsy for the Km 67 tower data. This research was funded by the NASA Earth System Science Fellowship 53-1970 and NASA contracts NNG0SGD15G and NNX06AC75G. We gratefully acknowledge the constructive comments by two anonymous reviewers, which improved the quality of the manuscript.

4 Assessing Temporal Clear-Sky Errors in Assimilation of Satellite CO₂ Retrievals Using A Global Transport Model

An edited version of this chapter was published by Copernicus Publications on behalf of the European Geosciences Union. Figure numbers, equation numbers, and citation styles have been changed for integration into the dissertation.

Corbin, K. D., A. S. Denning, and N. C. Parazoo, (2008), Assessing Temporal Clear-Sky Errors in Assimilation of Satellite CO₂ Retrievals Using a Global Transport Model, *Atmospheric Chemistry and Physics Discussion*.

Abstract

The Orbiting Carbon Observatory (OCO) and the Greenhouse gases Observing SATellite (GOSAT) will make global observations of the total column dry-air mole fraction of atmospheric CO₂ (X_{CO_2}) starting in 2008. Although satellites have global coverage, X_{CO_2} retrieval will be made only a few times each month over a given location and will only be sampled in clear conditions. Modelers will use X_{CO_2} in atmospheric inversions to estimate carbon sources and sinks; however, if satellite measurements are used to represent temporal averages, modelers may in-

cur temporal sampling errors. We investigate these errors using a global transport model. Temporal sampling errors vary with time and location, exhibit spatially coherent patterns, and are greatest over land and during summer. These errors often exceed 1 ppm and must be addressed in a data assimilation system by correct simulation of synoptic CO₂ variations associated with cloud systems.

4.1 Introduction

Atmospheric inversions, which use atmospheric CO₂ concentrations and a transport model to infer carbon sources and sinks, have provided valuable information regarding large-scale surface carbon fluxes (Gurney et al., 2002; Rodenbeck et al., 2003; Baker et al., 2006b). However, as modelers move to higher-resolution fluxes, the uncertainties increase primarily due to sparse data coverage (Gurney et al., 2003; Dargaville et al., 2005). In addition to the rapidly expanding surface network, CO₂ measurements from satellites will be used to quantify regional carbon sources and sinks. Studies indicate that spatially dense, global measurements of the column-integrated dry air mole fraction of atmospheric CO₂ (X_{CO_2}) with precisions of ~ 1 ppm are expected to substantially reduce the uncertainties in the CO₂ budget (Rayner and O'Brien, 2001; Baker et al., 2006a; Chevallier et al., 2007; Miller et al., 2007).

Two satellites designed specifically to measure X_{CO_2} are scheduled to launch in late 2008: the Orbiting Carbon Observatory (OCO) (Crisp et al., 2004) and the

Greenhouse gases Observing SATellite (GOSAT) (NIES, 2006). Both satellites will fly in a polar sun-synchronous orbit with an equator crossing time of ~ 1300 LST, collecting near-infrared spectra from reflected sunlight. OCO will orbit just ahead of the Earth Observing System (EOS) Aqua platform in the A-train, which has a 16-day repeat cycle. OCO has a 10 km-wide cross track field of view that is divided into eight 1.25 km-wide samples with a 2.25 km down-track resolution at nadir. GOSAT's orbit is recurrent every 3 days with a varying swath width from 88 to 800 km.

Satellite X_{CO_2} retrievals will be used in synthesis inversion and data assimilation models to quantify carbon flux estimates; however, X_{CO_2} measurements require clear conditions and are sampled at a single instance in time. If satellite data are used to represent temporal averages, variations in atmospheric CO_2 on synoptic time-scales may lead to temporal sampling errors. An observational assessment of systematic differences between mid-day CO_2 on clear-sky versus all days using multiyear continuous data at two towers located in mid-latitude forests found systematic differences of 1 to 3 ppm in CO_2 , with lower concentrations on sunny days than average (Corbin and Denning, 2006). The differences at both towers were greatest in the winter and were not attributable to anomalous surface fluxes. Another study used a high-resolution cloud-resolving model to analyze temporal sampling errors by comparing simulated satellite data to mean concentrations over an area equivalent to a global transport model grid column (Corbin et al., 2008). At both a temperate and a tropical site, the differences between

satellite measurements and diurnally and bi-monthly averaged transport model grid column concentrations were large (> 1 ppm). At the temperate site, the temporal sampling errors were negatively biased because of systematic X_{CO_2} anomalies associated with fronts that were masked by clouds.

While Corbin and Denning (2006) and Corbin et al. (2008) both previously showed underestimations of clear-sky satellite concentrations compared to the true temporal mean, both of these studies only assessed the differences under specific conditions. Corbin and Denning (2006) looked at continuous observations from towers that are both located in mid-latitude forests, and Corbin et al. (2008) focused on two simulations over limited regions for short time-periods in August. In this study, we are expanding on previous research by investigating the clear-sky temporal sampling errors using a global atmospheric transport model. In addition to assessing clear-sky differences globally, we also investigate how these differences vary on seasonal timescales.

4.2 Model and Methods

We simulated 2003 atmospheric CO_2 concentrations using the Goddard Space Flight Center (GSFC) Parameterized Chemical Transport Model (PCTM) (Kawa et al., 2004). The dynamical core of PCTM is a semi-Lagrangian algorithm in flux form from Lin and Rood (1996). PCTM is driven by meteorological fields from NASA's Goddard Earth Observation System version 4 (GEOS-4) data assimilation

system (DAS) (Bloom et al., 2005). PCTM was run with 1.25° by 1° horizontal resolution, 26 vertical levels up to 20.5 km, and a 7.5-minute time-step with CO_2 output every 3 hours. For spin-up, PCTM was run for 3 years from 2000-2002.

The surface fluxes of CO_2 include biological fluxes, ocean fluxes, and fossil fuel emissions. Surface sources and sinks associated with the terrestrial biosphere are based on computations of hourly net ecosystem exchange from the Simple Biosphere Model version 3 (SiB3) (Sellers et al., 1996b,a; Baker et al., 2007). Ocean fluxes are adopted from Takahashi et al. (2002), and estimates of fossil fuel emissions are from Andres et al. (1996). Comparisons to a network of in-situ continuous analyzers showed that the simulation captures synoptic features well (Parazoo et al., 2008).

To assess temporal sampling differences, for each grid-column in the model we compare simulated satellite concentrations to the corresponding concentrations that include all conditions. Differences between the simulated satellite data and the mean modelled concentrations are assessed on both annual and seasonal time-scales. While there are large differences in the size of the model grid cells and the OCO samples, Corbin et al. (2008) found spatial representation errors are less than 0.5 ppm, indicating that it is reasonable to simulate OCO observations from a model of this resolution.

To simulate satellite data, PCTM was sampled using the OCO methodology. First, we created a clear-sky subset of PCTM CO_2 concentrations. To determine if the grid cell is clear, we used downwelling solar radiation data from GEOS-4 and

created the clear-sky subset using the top-ranked data per month for each grid cell above a specified threshold value.

Simulating OCO orbit and scan geometry, Rayner et al. (2002) calculated a 26% probability that a pixel within a transport model grid cell will be clear. As cloud cover varies with location and time of year, we investigated both 15% and 40% thresholds to assess temporal sampling errors at realistic minimum and maximum coverage. Decreasing the threshold value to 15% produces more random errors with larger differences, while increasing the threshold to 40% decreases the magnitude of the differences but increases the spatial coherency. Since the main conclusions from this analysis are robust among all three thresholds, we will show the results from the 26% threshold value.

Since OCO is not yet in orbit, we used CloudSat tracks to determine the location and timing of satellite overpasses. CloudSat, an existing satellite in the A-train constellation, is flying with a nearly identical orbit only minutes behind the proposed OCO orbit (Stephens et al., 2002). This study used CloudSat tracks from January 1 through January 16, 2007, and the tracks are repeated every 16 days for the entire year; however, we only use data from the ascending branch since OCO requires sunlight. The model was sampled at the grid cell that included the satellite retrieval at the closest model hour available, using only the concentrations included in the clear-sky subset. After sampling the data, the concentrations were pressure weighted to create the OCO subset of total column CO₂.

4.3 Results

Annual mean temporal sampling errors are calculated by subtracting the annual mean total-column CO₂ concentration from the annual mean concentration in the simulated OCO subset for each grid cell [Figures 4.1 and 4.2]. Differences between the satellite-retrieved annual mean and the true annual mean are small in the southern hemisphere and increase with latitude. Large differences (> 1 ppm) occur over land and in the northern hemisphere. The standard deviation is ~ 0.8 ppm over subtropical land in the southern hemisphere, reflecting the large differences seen over South America. In the northern hemisphere, zonally averaged standard deviations greater than 1 ppm occur. Spatially coherent negative differences can be seen over southeastern North America, southern South America, the North Atlantic Ocean, and Europe. The zonal average of the annual mean differences is ~ -0.3 ppm in the northern hemisphere mid-latitudes, indicating inversions may incur a negative bias if satellite measurements are used to represent an annual mean.

We calculated seasonal temporal sampling errors incurred from using satellite measurements to represent seasonal averages by subtracting the 3-month seasonal total column CO₂ PCTM concentrations for each grid cell from the seasonal mean in the OCO subset at the same grid cell [Figures 4.3, 4.4, and 4.5]. The magnitude and location of the differences varies by season. Large differences occur during the summer, as the greatest standard deviation in the southern hemisphere is in DJF

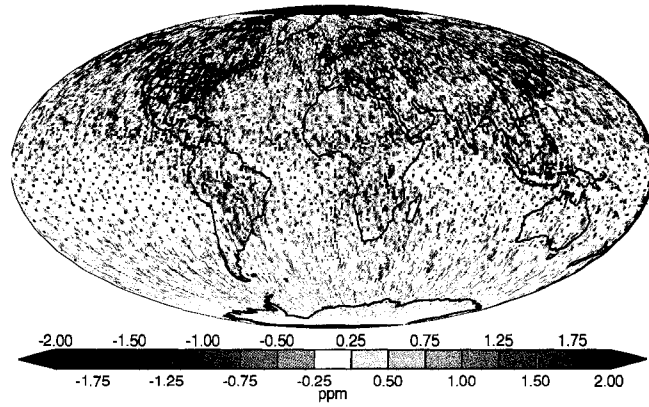


Figure 4.1: Annual mean temporal sampling errors, obtained by subtracting the annual mean at each grid cell from the annual mean in the OCO subset.

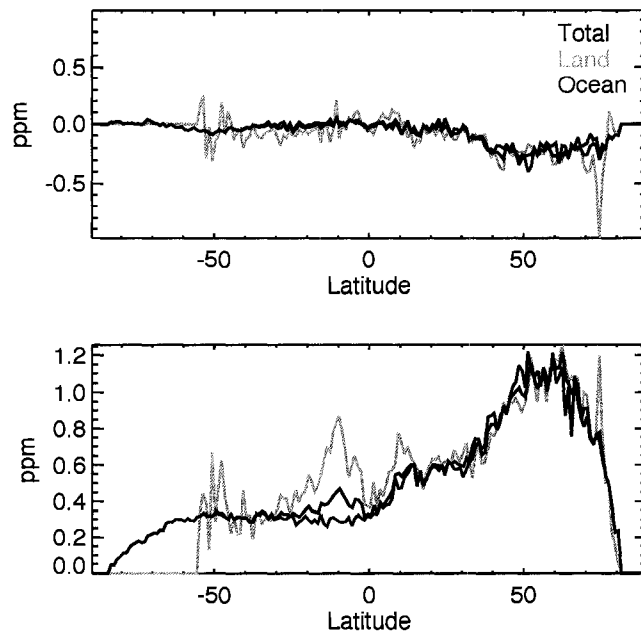


Figure 4.2: **Top)** Zonal averages of the annual mean temporal sampling errors. The black line indicates the total zonal mean, the green line shows the zonally-averaged errors over land and the blue line shows the zonally-averaged errors over ocean. **Bottom)** Zonal standard deviations of the annual mean temporal sampling errors.

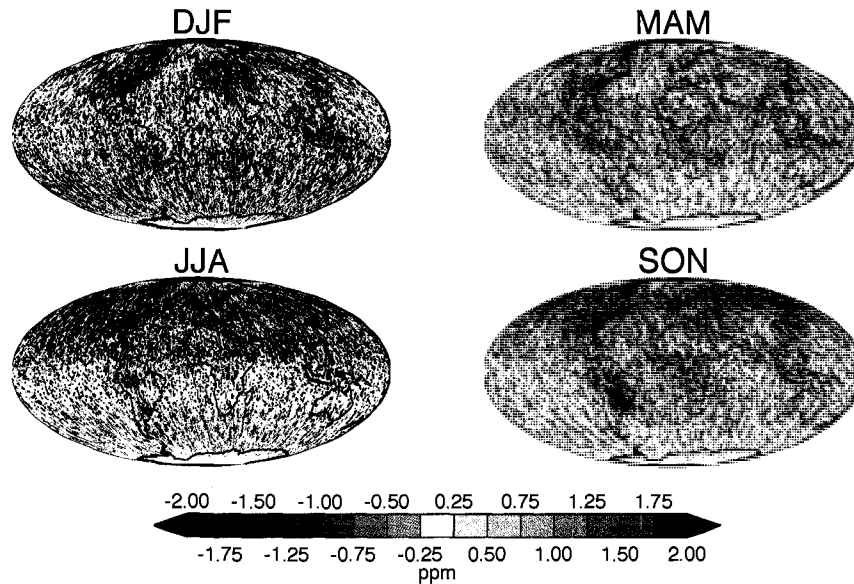


Figure 4.3: Seasonal temporal sampling errors, calculated by subtracting the grid cell mean for each season from the grid cell mean in the OCO subset.

and in the northern hemisphere is JJA. Differences also tend to be larger over land regions, likely due to the larger biospheric fluxes and fossil fuel emissions.

The seasonal maps show coherent spatial patterns. In the northern hemisphere winter, significant underestimates of the mean are seen in the eastern United States and Europe, while slight overestimations are prevalent near India. The regional underestimations can be seen in the zonal mean of the errors. The transition period during MAM has relatively small errors compared to the other seasons, as the standard deviations are less than 1 ppm; however, over tropical South America the satellite measurements are higher than the seasonal mean and over higher northern latitudes the concentrations over land are biased lower than average. In JJA, over the southern hemisphere and tropical oceans the errors are small and random, while

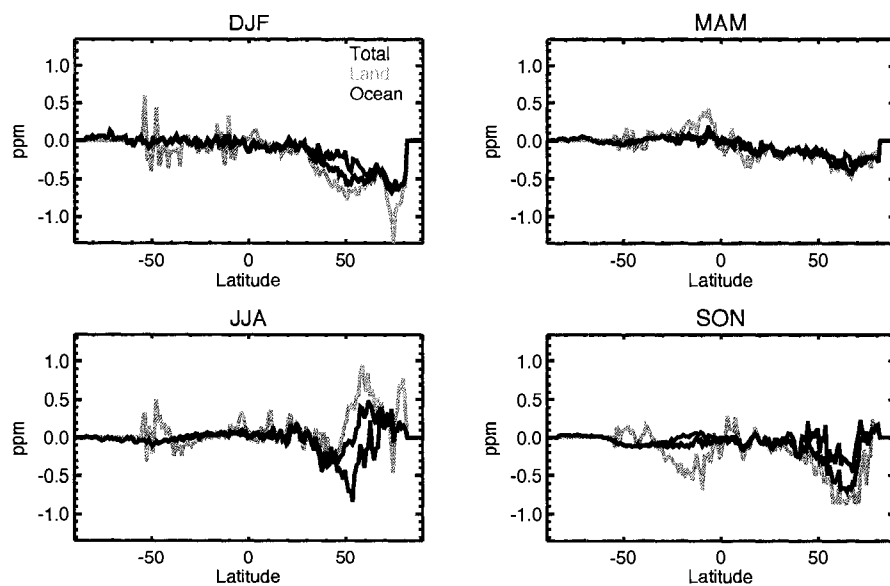


Figure 4.4: Seasonal zonally-averaged temporal sampling errors.

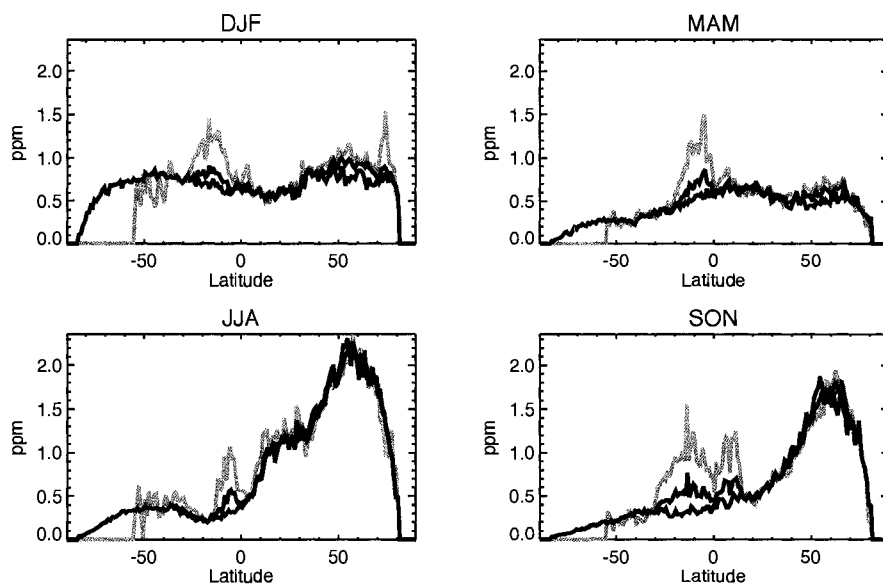


Figure 4.5: Seasonal zonally-averaged standard deviations of the temporal sampling errors.

over southern South America the satellite underestimates the seasonal mean in the southern half of the continent and overestimates the mean in the northern portion. Large overestimates can be seen in Asia, while underestimates can be seen over the north Atlantic. SON is also characterized by larger zonally averaged errors, particularly from regional overestimates in Asia and underestimations in South America. Calculating seasonal temporal sampling errors reveals large, spatially coherent differences between satellite measurements and temporal means that vary with time and location.

4.4 Conclusions

This study indicates that modelers cannot use satellite measurements sampled only in clear conditions to represent temporal averages. The 2003 annual mean errors calculated using PCTM are relatively small and randomly dispersed; however, the errors introduced into inversions using satellite data to represent smaller timescales such as seasonal means vary with both time and location and exhibit coherent spatial patterns at continental scales. The differences are largest during summer months and tend to be greater over land. In the northern hemisphere, relatively large regions in North America and Europe underestimate the temporal mean in the winter and fall, while these regions have large but random differences in the summer. Over South America, satellite measurements overestimate the concentrations in fall and winter but underestimate the concentrations during spring.

Although these errors should be investigated for various years using different transport models, it is likely spatially coherent patterns would still exist due to the covariance between clouds and CO₂ concentrations. Systematic variation of CO₂ and cloudiness due to advection along frontal boundaries produces differences between satellite observations and modeled time-means. It is imperative that source/sink estimates from satellite data match the sampling time and location to the observation platform. Further, transport models will need to capture correct placement and timing of synoptic weather features, including fronts and clouds.

Acknowledgements

We thank John Haynes for providing the CloudSat orbital information. This research was funded by the National Aeronautics and Space Administration (NASA) Earth System Science Fellowship 53-1970 and NASA contracts NNX06AC75G and NNG05GF41G.

5 An Evaluation of SiB3-RAMS and an Analysis of the Impact of Sub-Grid Land Cover Heterogeneity

Abstract

Numerous modifications have been made to the coupled ecosystem-atmosphere model SiB3-RAMS. One of the primary changes in the model is the inclusion of subgrid land-cover heterogeneity using patches. We evaluate the performance of SiB3-RAMS and the sensitivity of modeled CO₂ fluxes and concentrations to land cover by performing three simulations: using only C3 vegetation, including C4 grasses and crops, and using both C3 and C4 biomes while including patches of subgrid heterogeneity. SiB3-RAMS overestimates the summertime respiration at boreal sites; and the model underestimates the summertime uptake in mixed forests, causing the seasonal cycle of NEE to be underestimated at these locations; however, the model captures the fluxes at needleleaf forests and grasslands reasonably well. Inclusion of C4 vegetation and patches alters the net ecosystem exchange (NEE) across much of North America (NA). The greatest differences

occur in the Great Plains, where C4 vegetation enhances the summertime uptake, and over the southeast, where including the land cover heterogeneity reduces the magnitude of the regional summer source. Due to the large fractional coverage of C4 crops and grasses across NA, it is essential to include these biomes in model simulations. Including surface heterogeneity improves the CO₂ concentrations in the model, reducing the root mean square errors at tower sites by ~1 ppm on average.

5.1 Introduction

Although inverse models have provided valuable information regarding carbon sources and sinks, both the location and magnitude of these sources and sinks, as well as the processes driving them, remain highly uncertain (Gurney et al., 2002; Stephens et al., 2007; Jacobson et al., 2007). Recent effort has been shifted from quantifying sources and sinks on the global scale down to local and regional scales with higher time resolution (Peylin et al., 2005; Zupanski et al., 2007; Peters et al., 2007; Schuh et al., 2008). Fluxes and concentrations from regional forward model simulations can be used in inverse modeling to help improve the source/sink estimates.

In addition to providing *a priori* flux estimates, regional models have been used to study processes driving the variability of atmospheric CO₂ concentrations. Several studies have used coupled biosphere-atmosphere models to demonstrate the

importance of mesoscale variability on CO₂ concentrations. Nicholls et al. (2004) used a coupled model to investigate the mechanisms leading to CO₂ variability over the Great Lakes region in the United States, concluding that meteorological processes associated with complex terrain, such as katabatic winds and lake breezes, lead to substantial CO₂ advection and variability. A study by Lu et al. (2005) over a heterogeneous landscape in the Tapajos National Forest in South America also shows that CO₂ concentrations and fluxes are sensitive to mesoscale circulations induced by topography and differences in roughness lengths between land and water. van der Molen and Dolman (2007) used a regional model to demonstrate that relatively modest changes in topography can cause large horizontal gradients in the boundary layer that persist for hours. These studies all suggest that understanding mesoscale processes is essential in interpreting atmospheric concentrations and fluxes, particularly at specific sites on a regional scale.

Coupled models have also been used to investigate the role of synoptic events on atmospheric CO₂ variability (Chan et al., 2004; Geels et al., 2004; Wang et al., 2007). All these studies show that the CO₂ field is strongly influenced by the atmospheric dynamics. Synoptic systems alter the biosphere fluxes through radiative forcing and temperature variability, and synoptic variability in CO₂ concentrations is due to a combination of variations in carbon fluxes and large-scale horizontal advection and mixing.

Finally, coupled models have been used to investigate the utility of CO₂ measurements in inverse models by analyzing representation errors (Tolk et al., 2008;

Corbin et al., 2008). Synoptic variability causes large representation errors, particularly when observations are used to represent temporal averages. In the mid-latitudes, clouds associated with frontal systems will inhibit satellite measurements; however, these systems are associated with large concentration gradients due to horizontal advection and deformational flow (Parazoo et al., 2008). To minimize representation errors in inversions, these regional studies show that CO₂ measurements should only be used to represent modeled concentrations sampled at the same time.

Since regional models are used for a variety of applications, it is essential to continually identify shortcomings in the model and implement modifications to help improve these tools. One difficulty of regional modeling is correctly classifying the land cover type. Satellite maps provide high-resolution land cover classifications, but frequently these maps do not discriminate between C3 and C4 vegetation (Hansen et al., 2000; Mu et al., 2007). The partitioning between C3 and C4 vegetation has important implications on the carbon cycle, as well as on surface temperature, humidity, and energy fluxes (Still et al., 2003; Sellers et al., 1992; Collatz et al., 1992). C4 photosynthesis is a mechanism to overcome photorespiration, and is favorable in hot and dry climates. C4 plants are generally favored over C3 plants in arid or semiarid regions, such as the Great Plains of the United States. C4 plants are more productive at higher temperatures since the rate of photosynthesis in these plants is invariant to a wide range of temperatures, unlike C3 plants where the quantum yield decreases with temperature. Incorrect

partitioning of C3 into C4 vegetation will alter the carbon fluxes and hence impact the resulting concentrations.

Another difficulty in regional modeling is sufficiently capturing the land cover heterogeneity, as the land surface is characterized by pronounced spatial heterogeneity that spans a wide range of scales. To incorporate subgrid heterogeneity, one common technique in land surface modeling is to introduce patches, which divides the area of each grid cell into fractions covered by various vegetation types. Using patches allows the model grid cell to be represented by various land cover types, rather than just one dominant biome. Land-cover patches have been used in a variety of applications to improve energy fluxes and the hydrological cycle (Giorgi and Avissar, 1997; Essery et al., 2002; Avissar and Pielke, 1989; Overgaard et al., 2006); however, little work has been done to investigate the utility of patches in simulating CO₂ fluxes and concentrations.

The purpose of this study is to evaluate CO₂ fluxes and concentrations from the regional coupled atmosphere-biosphere model SiB3-RAMS and to investigate the impact of land cover classification. To do this, we perform three separate simulations: one that does not include C4 vegetation, one that uses a separate C3/C4 fractionation map to partition grasslands and croplands into C3 and C4 classes, and one simulation that includes both C3 and C4 vegetation as well as patches to capture the land cover heterogeneity. Resulting modeled NEE and CO₂ are compared to observations measured at towers across North America.

5.2 Methods

5.2.1 Model Description SiB3-RAMS

This study uses the Simple Biosphere Model Version 3 (SiB3) coupled to the Brazilian version of the Colorado State Regional Atmospheric Modeling System (RAMS). This coupled model has been used for a variety of applications (e.g. Denning et al., 2003; Nicholls et al., 2004; Wang et al., 2007; Corbin et al., 2008). Details of the model can be found in these previous studies; however, we have made numerous modifications. In this section we will briefly outline the important aspects of the model and highlight the changes.

SiB3 calculates the transfer of energy, mass, momentum, and CO₂ between the atmosphere and the vegetated surface of the Earth (Baker et al., 2003; Sellers et al., 1996b,a). To parameterize photosynthesis, SiB3 uses the photosynthesis model of Farquhar et al. (1980) and the stomatal model of Ball (1988); and the photosynthesis rate is linked with stomatal conductance using the Ball-Berry-Collatz equation (Collatz et al., 1991, 1992). The photosynthesis rate for each grid cell is scaled from the leaf-level to the canopy using satellite-derived leaf area index (LAI) and absorbed fraction of photosynthetically active radiation (FPAR).

A number of modifications have been added to SiB3 (I. T. Baker, personal communication). For more realistic flux calculations, a prognostic equation for the canopy air space has been added (Vidale and Stockli, 2005). Model hydrology has been improved by adopting the Community Land Model soil/snow submodel,

where soil temperature and soil moisture are calculated for ten co-located soil layers and up to five snow layers. All snow and soil layers have explicit treatment of liquid water and ice, and the root profile in the soil exponentially decreases from the surface down to the bottom soil layer. In addition, the effect of soil moisture stress on photosynthesis has been modified to allow a more realistic response of transpirational load shifting to deep layers when the surface layer dries out, and a simple approximation of frost stress has been added. Finally, respiration has been partitioned into autotrophic and heterotrophic components to help improve the annual cycle of carbon uptake and release.

To capture spatial land cover heterogeneity, we have implemented the capability to represent multiple land use classes within a single grid cell. Each grid cell is subdivided into non spatially-explicit patches of different vegetation classifications in order to more accurately model sub-grid scale land cover heterogeneity. The prescribed vegetation map is used to determine the land cover classification and associated fractional coverage of each patch. Since the vegetation map has a higher resolution than the model grid cell, the number of pixels for each biome is determined. The three biomes with the most pixels are the top three patches. The associated fractional coverage is calculated by dividing the number of pixels for each of the vegetation classes by the total number of pixels in the model grid cell, and weighting each of the associated areas so that the sum of the patch areas matches the total area of vegetation in the grid cell. SiB3 calculates the fluxes for each of the patches separately, and the total fluxes to the atmosphere are

calculated as an area-weighted combination of the contributions from each patch. In this study, we used three patches to capture the dominant land cover classes. We chose three patches as the area coverage of vegetation classes beyond the top three were minimal ($< 10\%$).

RAMS is a comprehensive mesoscale meteorological modeling system designed to simulate atmospheric circulations spanning in scale from hemispheric scales down to large eddy simulations of the planetary boundary layer (Frietas et al., 2006; Pielke et al., 1992; Cotton et al., 2002). RAMS is a fully three-dimensional, non-hydrostatic model that includes the capabilities to nudge the model fields to gridded analysis data, and to incorporate telescoping nested grids, allowing the model to solve the equations simultaneously on any number of interacting computational meshes of differing spatial resolutions (Walko and Tremback, 2002; Clark and Farley, 1984).

RAMS supports various turbulence closure, short and long wave radiation, boundary, and convection schemes. The turbulence closure option used in this study is the Mellor and Yamada (1982) scheme for vertical diffusion and the Smagorinsky (1963) scheme for horizontal diffusion. The radiation scheme used is the two-stream radiation scheme developed by Harrington (1997), and the lateral boundaries utilize the radiation condition discussed by Klemp and Wilhelmson (1978). For convection, this study used the Grell convective cumulus scheme, which is an entraining plume model based on the quasi-equilibrium assumption (Grell, 1993; Grell and Devenyi, 2002).

5.2.2 Model Initialization and Input Data

The meteorological fields in SiB3-RAMS are initialized by the National Center for Environmental Prediction (NCEP) mesoscale Eta-212 grid analysis with 40-km horizontal resolution (AWIPS 40-km). The analyses of horizontal wind, temperature, geopotential height, and specific humidity are also used to nudge both the lateral boundaries and the interior grid cells every three hours.

The land cover classification, leaf area index (LAI), and fraction of photosynthetically active radiation (FPAR) are remotely sensed data with 1-km horizontal resolution from the Moderate Resolution Imaging Spectroradiometer (MODIS) on the NASA AQUA platform. The data were filled and processed by the Numerical Terradynamic Simulation Group (NTSG) at the University of Montana (Zhao et al., 2005; Mu et al., 2007). The vegetation classes were reclassified into the corresponding classification in SiB3 using two methodologies. The first method used only C3 vegetation classes, since the original MODIS classification did not separate C3 and C4 species. The second method used overlaid a C3/C4 percent land cover map with 5 minute horizontal resolution from Leff et al. (2004) to further discriminate the vegetation classes into C3 and C4 biomes.

The soil map for SiB3-RAMS is a product of the International Geosphere-Biosphere Programme (IGBP) (IGBP, 2000). The original data were a soil type map of % sand / % clay / % silt values with 5 minute (~ 10 km) resolution. The data were then binned into soil classes (Sellers et al., 1996a).

Surface carbon fluxes due to fossil fuel combustion are prescribed by the Vulcan inventory, which represents the U. S. fossil fuel CO₂ emissions for 2002 at \sim 10 km spatial scale and hourly (Gurney et al., 2008). Using U. S. Environmental Protection Agency (EPA) emissions models and data, Vulcan is a comprehensive database that combines inventory data, process attributes, and classification information to construct the detailed emissions estimates. Vulcan utilizes three classes of input: point sources (i.e. power plants), mobile sources (i.e. vehicle emissions), and area sources (i.e. residential sources). To scale the emissions estimates to 2004, we matched the annual total emissions to the estimated emissions from the Energy Information Administration (EIA, 2007). Carbon monoxide emissions from anthropogenic activities are set to 1% of the CO₂ fluxes (Gamnitzer et al., 2006).

Air-sea CO₂ fluxes are the monthly estimates from Takahashi et al. (2002). Fluxes of carbon due to fire emissions are prescribed from the Global Fire Emissions Database version 2 (GFEDv2) (van der Werf et al., 2006). The database consists of 1° x 1° gridded monthly fire emissions of both CO₂ and CO.

To initialize respirable carbon, soil moisture, and prognostic variables, we used offline SiB3. We ran SiB3 for ten years from 1994-2004, using meteorological data from the NCEP Department of Energy (DOE) AMIP-II reanalysis. NCEP reanalysis II data were provided by the NOAA/OAR/ESRL Physical Sciences Division (PSD) in Boulder Colorado, USA and is available from their website at <http://www.cdc.noaa.gov>. SiB3 calculated the necessary fields for every grid cell. It is important to keep in mind that SiB3 is a balanced model: in calculating

the respiration factor, the total respiration in a year must equal the total uptake during the year.

The initial CO₂ field and the lateral boundaries in SiB3-RAMS are set and nudged every 3 hours to 2004 global concentrations from the Goddard Space Flight Center (GSFC) Parameterized Chemical Transport Model (PCTM) (Kawa et al., 2004). PCTM is driven by meteorological fields from NASA's Goddard Earth Observation System version 4 (GEOS-4) data assimilation system (DAS) (Bloom et al., 2005), and PCTM has 1.25° x 1° horizontal grid increments, 26 vertical levels up to 20.5 km, and a 7.5-minute time-step with CO₂ output every 3 hours. For spin-up, PCTM was run for three years, from 2000-2003. The PCTM simulation includes surface CO₂ fluxes from SiB3 biological fluxes (Baker et al., 2007), ocean fluxes (Takahashi et al., 2002) and fossil fuel emissions (Andres et al., 1996). Comparisons to a network of in-situ continuous analyzers showed that the simulation captures synoptic features well (Parazoo et al., 2008).

The initial CO field and the lateral boundaries are set and nudged to 2004 monthly-mean global concentrations from GEOS-CHEM, a global three-dimensional model of tropospheric chemistry driven by assimilated meteorological observations from GEOS-4. This simulated CO from GEOS-CHEM has 5° x 4° grid spacing and 30 vertical levels up to 66 km [P. Kasibhatla, personal communication]. The sink for CO is the reaction with hydroxyl radicals (OH) to create CO₂. The OH field is a 3-D climatological distribution with monthly temporal resolution, 10° x 8° horizontal grid increments, and 7 pressure levels (Spivakovsky et al., 2000).

5.2.3 Case Descriptions

In this study, we perform three simulations over North America (NA) with SiB3-RAMS. All three simulations run from 0000 UT 1 May to 0000 UT 1 September 2004. The simulations have 150 x 90 gridcells with 40 km horizontal grid increments and 46 vertical levels up to 24 km.

The first case, which we will refer to as C3, uses the SiB3 vegetation classes that correspond to the original MODIS biome map, which results in no C4 crops or grasses. The vegetation class in each grid cell is set to the dominant vegetation type. Figure 5.1 shows the fractional coverage of each SiB3 biome class for the C3 simulation. The majority of the central and mid-western U. S. is classified as C3 grasses and cropland. The southern and eastern portions of the U. S. are primarily covered by deciduous and mixed forests, Canada is predominantly needleleaf forest, and the southwestern U. S. is covered by shrubs.

The second case, C4, overlays the C3/C4 coverage maps and separates out C4 grasses and crops from the original C3 biome based on the C4 percent coverage for each gridcell. Using the C3/C4 map, much of the cropland over Nebraska and Iowa is C4 crops, and a significant portion of the western U. S. is C4 grassland. Maps of the fractional coverage of each biome class are shown in Figure 5.2.

The third case, PAT, uses C3 and C4 vegetation classes and utilizes patches, allowing three different biome types per grid cell (Figure 5.3). While much of midwestern U. S. is still predominantly covered with C3 grassland and crops, the

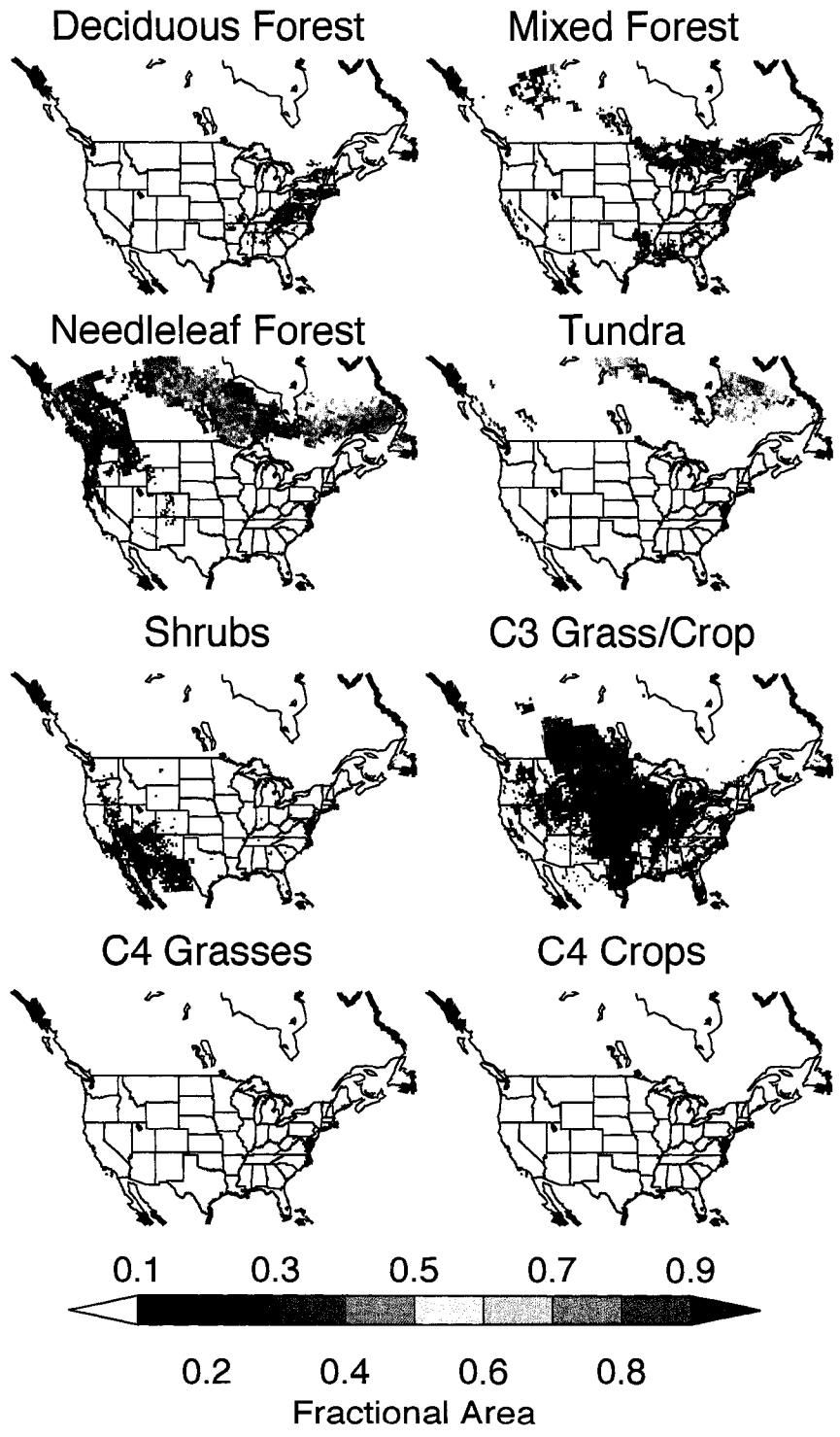


Figure 5.1: Percent land cover classifications using only C3 vegetation classes. Fractions < 1. are due to the presence of surface water.

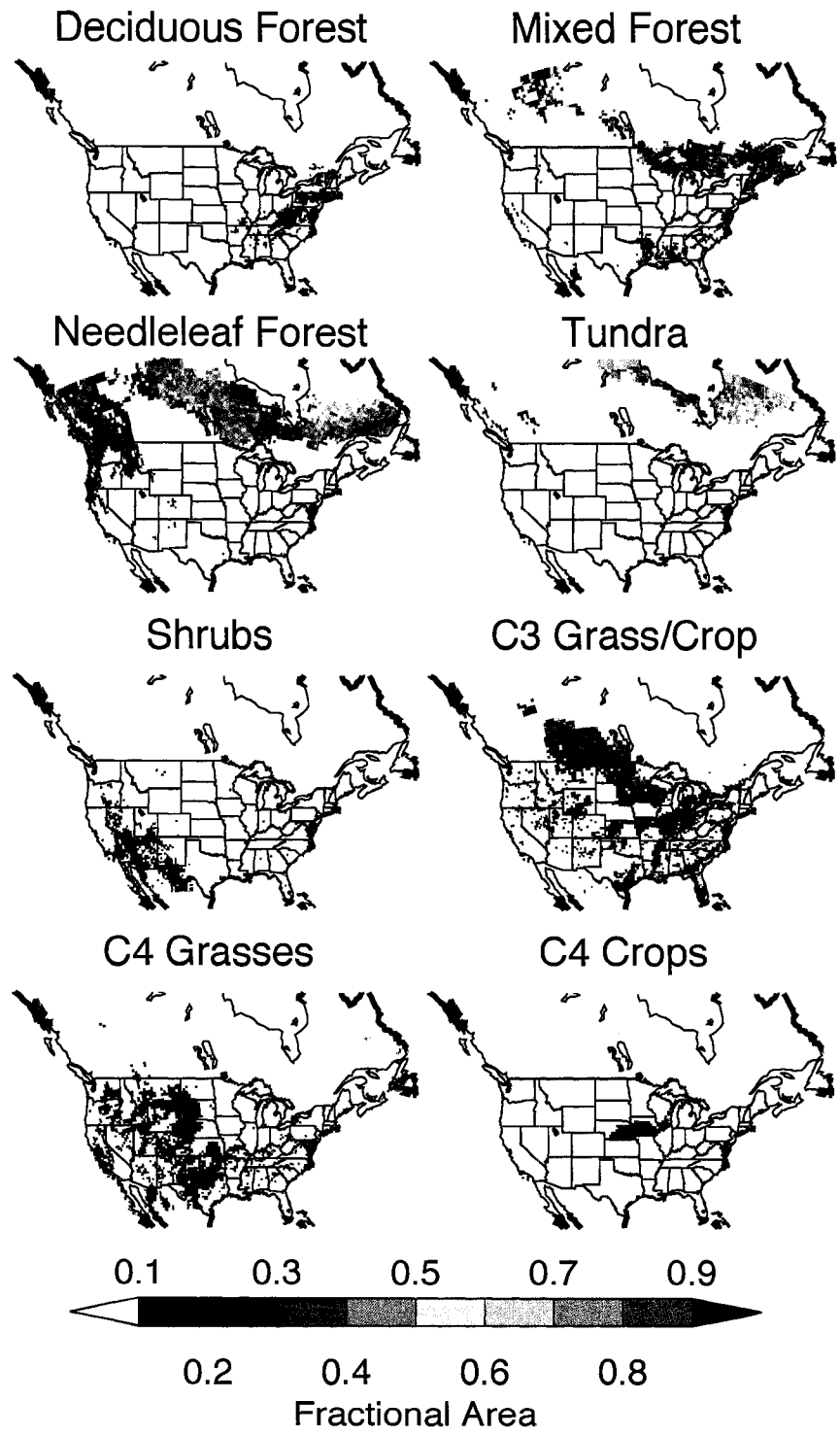


Figure 5.2: Percent land cover classifications including both C3 and C4 vegetation classes.

remaining regions of North America have considerable sub-grid scale heterogeneity. The vegetation coverage over the southern U. S. includes contributions from deciduous forest, mixed forest, C3 grasses and crops and C4 grasses. Over Canada, many of the grid-cells in the model contain deciduous forest, mixed forest, and tundra; and in the west shrubs, forests, and both C3 and C4 grasses all exist in a single grid cell and contribute to the land cover heterogeneity.

5.2.4 Observations

This study utilized continuous observations of CO₂ concentrations and net ecosystem exchange (NEE) measured at towers across the United States and Canada. Figure 5.4 shows a map of the locations of the towers used in this study. The flux tower data were obtained from FLUXNET (Olsen et al., 2004; Baldocchi, 2006), and is available on-line at <http://www.fluxnet.ornl.gov>. The majority of the continuous CO₂ observations are funded by the National Oceanic and Atmospheric Administration (NOAA) Earth System Research Laboratory (ESRL) Global Monitoring Division (GMD) and are publicly available at <http://esrl.noaa.gov/gmd>. Only flux tower sites where the dominant vegetation at the tower matches the dominant vegetation in the model grid cell are included. At towers that measure CO₂ concentrations at various levels on the tower, we used the data from the top level.

Data from five tower sites in Canada are used to evaluate SiB3-RAMS. The Western Peatland Flux Station (WPL) is located in a treed fen with stunted black

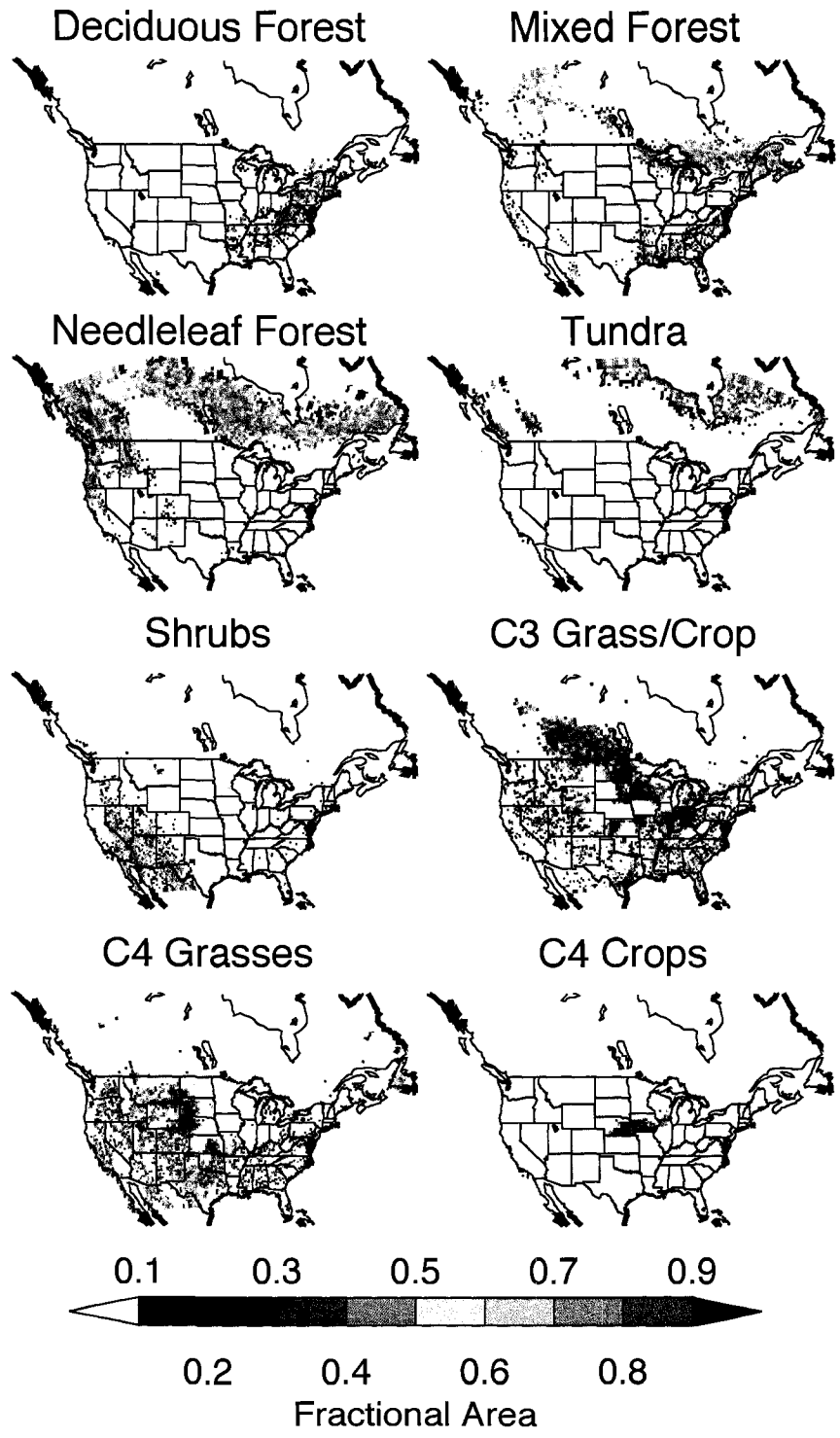


Figure 5.3: Percent land cover classifications including C3 and C4 vegetation and patches.

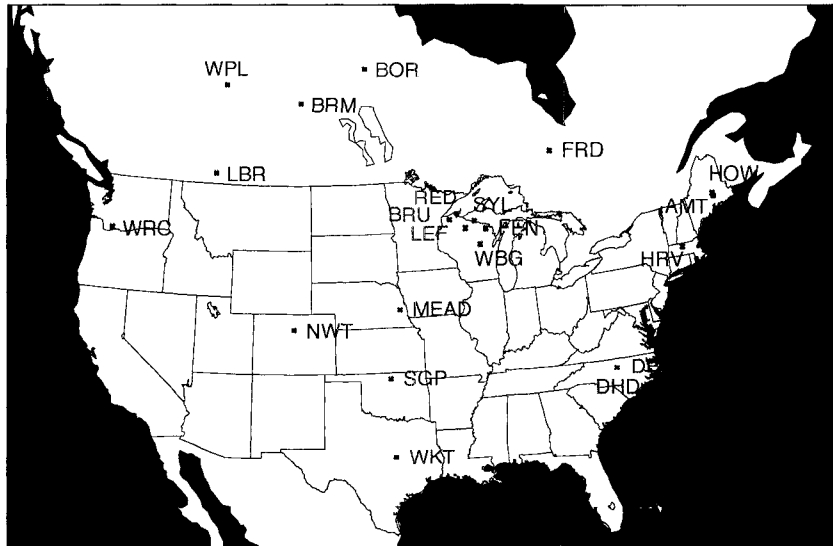


Figure 5.4: The locations of the tower sites used in this study.

spruce and larch trees (Syed et al., 2006). Near Lethbridge, Alberta, a 36 m flux tower (LBR) measures carbon fluxes over a northern temperate grassland. A more detailed description of the LBR station can be found in Ponton et al. (2006); Flanagan and Johnson (2005); Flanagan et al. (2002). The Boreal Ecosystem-Atmosphere Study (BOREAS) Northern Old Black Spruce (NOBS) flux tower site in central Manitoba, Canada (BOR) is situated on the low-relief terrain near the northern limit of the boreal forest, and the vegetation at the site is dominated by 160-year-old black spruce trees (Goulden et al., 1997; Steele et al., 1997; Dunn et al., 2007). Continuous CO_2 measurements are collected at both the Saskatchewan Station (BRM) and the Fraserdale tower (FRD). BRM is located in a 111 year-old mature black spruce overstory with feather moss ground cover (Amiro et al., 2006), and FRD is located on the southern perimeter of the Hudson

Bay lowland on the northern edge of the boreal forest. The tower sits in a small clearing at the edge of a reservoir and is in a region with extensive wetland coverage (Chan et al., 2004). Although 2004 data are available at the British Columbia Flux Station in western Canada, this flux tower was not included in this analysis as the LAI data was only approximately half of the observations at the site (Humphreys et al., 2003).

Over the United States, this study uses data from 16 flux towers. The Wind River Crane Site (WRC), a flux tower in Washington state, is located in a protected old-growth coniferous forest dominated by Douglas fir and western hemlock (U et al., 2004; Chen et al., 2004). The Niwot Ridge Forest flux tower (NWT) is situated in a subalpine coniferous forest in the Rocky Mountains on a glacial moraine (Sacks et al., 2006; Monson et al., 2005). The WKT tower is located near Moody, Texas in the Great Plains of North America over grasslands characterized by cattle grazing. High-calibrated CO₂ data are collected at the tower up to 457 m. A more complete description of the site can be found at <http://www.esrl.noaa.gov/gmdl/> (Tans and et. al., 1996; Bakwin et al., 1998; Zhao et al., 1997). The Atmospheric Radiation Measurement (ARM) Southern Great Plains (SGP) site makes flux and concentration measurements at a 60 m tower over a field containing winter wheat, some pasture, and summer crops (Fischer et al., 2007; Sims and Bradford, 2001). In Nebraska, the MEAD rainfed site measures reports NEE from carbon flux and storage measurements 6 m off the ground above a maize soybean rotation (Verma et al., 2005).

The Park Falls, Wisconsin tower (LEF) measures both fluxes and concentrations of CO₂ in a heavily forested zone of low relief. Mixed evergreen and deciduous forests dominate the area surrounding the tower (see Ricciuto et al. (2007); Davis et al. (2003); Bakwin et al. (1998) for a description of the site and measurements). During the spring and summer of 2004, additional CO₂ measurements were deployed on four 76 m communications towers forming a ring around the LEF tower with a 100-150 km radius. The towers included in the Ring of Towers are Brule (BRU), Redcliffe (RED), Fence (FEN), and Wittenberg (WBG). Just northeast of LEF, flux and concentration measurements are collected at the Sylvania Wilderness Area (SYL). SYL is in an old-growth forest dominated by eastern hemlock, sugar maple, basswoods, and yellow birch (Desai et al., 2005).

Five of the towers used in this study are located along the East coast. The Duke Forest hardwoods flux tower (DHD) in North Carolina is situated in a 80-100 year old stand in an oak-hickory type forest composed of mixed hardwood species with pine as a minor component. The Duke Forest loblolly pine flux tower site (DPP) is located in a pine forest composed of even-aged loblolly pine, deciduous, oak-hickory, mixed hardwood, and evergreen coniferous species. A more detailed description of both towers can be found in Stoy et al. (2005, 2007). Further north in Massachusetts, the Harvard Forest tower (HRV) is in a mixed forest that contains oak, maple, hemlock, and spruce (see Wofsy et al. (1993); Goulden et al. (1996) for further details). CO₂ measurements are collected at a tower in Argyle, Maine (AMT). The site is characterized by deciduous forest and a heavy

population to the south of the tower (Tans and et. al., 1996; Bakwin et al., 1998; Zhao et al., 1997). The last tower in this study is Howland Forest (HOW), which collects both fluxes and CO₂ concentrations and is located in a boreal-northern hardwood transitional forest consisting of hemlock, spruce, fir, aspen, birch, and hemlock-hardwood mixtures (Hollinger et al., 2004).

5.2.5 Modeled Vegetation Cover at the Tower Sites

The modeled vegetation classification at each tower is displayed in Table 5.1. For each case, the table depicts the fractional coverage of each biome in the model grid cell that includes the towers. The biome type at two towers, MEAD and LBR, switches from C3 crops and grasses to C4 vegetation. While some locations are not characterized by heterogeneous land cover (i.e. SGP, BOR, MEAD), several sites have significant contributions from all three biomes used in the PAT case. At LEF, C3 grass/crop, deciduous forest, and mixed forest all cover a significant portion of the region surrounding the tower. In the model, the NWT tower is in a grid cell that includes needleleaf trees, C4 grasses, and C3 grasses; and at the Duke sites the vegetation is relatively evenly distributed between deciduous forest, C4 grasses, and C3 grasses.

Ref.	Site	Deciduous Forest	Mixed Forest	Needleaf Forest	C3 Grass/Crop	C4 Grass	C4 Crop
A	WPL	0,0,0	x,94,94,43	0,0,0	0,0,41	0,0,0	0,0,0
B	LBR	0,0,0	0,0,0	0,0,1	x,99,0,17	0,99,81	0,0,0
C	BRM	0,0,0	0,0,31	x,94,94,58	0,0,5	0,0,0	0,0,0
D	BOR	0,0,0	0,0,7	x,100,100,92	0,0,0	0,0,0	0,0,0
E	FRD	0,0,3	x,97,97,66	0,0,28	0,0,0	0,0,0	0,0,0
F	WRC	0,0,0	0,0,17	x,97,97,71	0,0,0	0,0,1	0,0,0
G	NWT	0,0,0	0,0,0	x,100,100,45	0,0,15	0,0,40	0,0,0
H	WKT	0,0,0	0,0,10	0,0,0	x,90,90,55	0,0,26	0,0,0
I	SGP	0,0,0	0,0,1	0,0,2	x,100,100,97	0,0,0	0,0,0
J	MEAD	0,0,0	0,0,0	0,0,0	100,0,3	0,0,0	x,0,100,97
K	LEF	0,0,31	x,0,0,28	0,0,0	100,100,41	0,0,0	0,0,0
L	BRU	0,40,0	x,99,99,54	0,0,0	0,0,5	0,0,0	0,0,0
M	RED	0,0,12	x,86,86,48	0,0,0	0,0,26	0,0,0	0,0,0
N	FEN	0,0,42	x,100,100,49	0,0,0	0,0,9	0,0,0	0,0,0
O	WBG	0,0,12	x,0,0,0	0,0,0	100,100,80	0,0,0	0,0,8
P	SYL	0,0,4	x,85,85,80	0,0,0	0,0,1	0,0,0	0,0,0
Q	DPP	100,100,37	0,0,0	x,0,0,0	0,0,21	0,0,32	0,0,0
R	DHD	100,100,37	x,0,0,0	0,0,0	0,0,21	0,0,32	0,0,0
S	HRV	0,0,34	x,94,94,53	0,0,0	0,0,7	0,0,0	0,0,0
T	AMT	0,15,0	x,97,97,71	0,0,0	0,0,11	0,0,0	0,0,0
U	HOW	0,0,16	x,98,98,71	0,0,0	0,0,11	0,0,0	0,0,0

Table 5.1: Vegetation classification at each of the towers, in percent land cover. The first number is the percentage of coverage for the C3 run, the second number is the percent coverage for C4, and the final column is the coverage for the PAT case. The cover at the actual tower is depicted by an x. The remaining coverage not depicted is water.

5.3 Results

5.3.1 NEE Tower Comparisons

To evaluate SiB3-RAMS, we compare monthly diurnal composites of modeled NEE to diurnal composites of the data collected at flux tower sites across the United States and Canada (see Figure 5.4 for a location of the towers). The results have been grouped by biome type to help elucidate strengths and weaknesses in the model. Since assumptions in the eddy covariance technique require turbulent conditions, nighttime respiration may be underestimated in the measurements due to low turbulence and air mixing at night (Eugster and Siegrist, 2000; Lee, 1998). The night flux problem is by-passed by discarding the data corresponding to low mixed periods and replacing them by an assessment based on either the parameterization of the night flux response to climate or on look up tables (Falge et al., 2001; Papale et al., 2006). This approach, known as the u^* correction, uses the friction velocity, u^* , as a criterion to discriminate low and well mixed periods. Although FLUXNET datasets use the u^* correction, there is currently no set standard for data removal (Munger and Loescher, 2006; Papale et al., 2006). Although we will analyze all the data, it is important to keep in mind this data limitation when evaluating nighttime respiration magnitudes.

Monthly plots of diurnal composites at the boreal forest sites are shown in Figure 5.5. The model does a reasonable job at capturing the seasonality and the amplitudes of the diurnal cycle, particularly at WPL; however, the respiration

is too high causing NEE to be offset. Two factors may be contributing to the high summertime respiration seen at these sites. The first is that SiB3 is forced to annually balance respiration and photosynthesis, despite the fact that at many locations this assumption is not true. This site may be a sink of CO₂, causing the net assimilation to be underestimated. The second is that respiration is exponentially related to temperature, and underestimating soil temperatures during the winter may be forcing more respiration to occur during the summer months.

At BOR in August, the amplitude of the diurnal cycle is underestimated. In August, this site has a lower modeled water vapor mixing ratio than observed and experiences humidity stress during the day, which may be limiting the assimilation. Although the vegetation is boreal forest, both sites are classified as wetlands, which are not included in the model formulation. One potential cause of the stress is the omission of wetlands (Baker et al., 2003). We hypothesize that the inclusion of wetland classifications in SiB3-RAMS would increase the relative humidities and water vapor mixing ratios seen at the site due to the increased ground water available for evaporation, causing a decrease in the daytime stress.

Monthly plots of diurnal composites at needleleaf forests are displayed in Figure 5.6. The diurnal composites for May are not shown as the remotely sensed LAI data were less than half the observed LAI at both sites, which is likely due to snow and cloud contamination in the dataset. The model does a reasonable job at capturing the mean daytime uptake and the nighttime respiration. At NWT, SiB3-RAMS also captures the correct shape of the diurnal cycle; however, at WRC

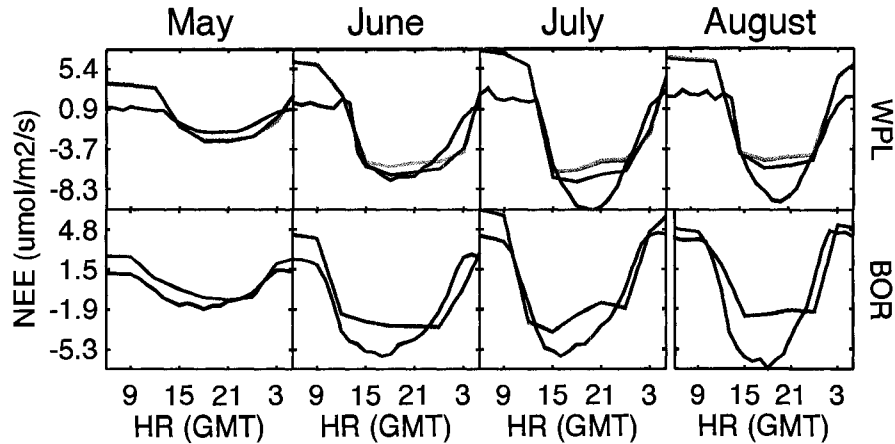


Figure 5.5: Monthly diurnal composites of the NEE at boreal forest sites. Black=observations, Red=C3 simulation, Green=C4 simulation, Blue=Patches simulation.

the model has constant uptake for several hours throughout the daytime rather than the v-shape seen in the observations. One potential cause for the mismatch in the shape of the daytime drawdown is that the FPAR values are prescribed from MODIS data and do not take into account changes with solar zenith angle. Another contributing factor may be that the version of SiB3 coupled to RAMS does not separate radiation into direct sunlight and shaded fractions, which has been shown to better reproduce the daytime v-shaped observations (I. T. Baker, personal communication).

Diurnal composites at the mixed forest sites are shown in Figure 5.7. Both Duke Forest sites (which are in the same model grid cell) do not show strong seasonality in NEE, but rather have relatively constant uptake over all four months. The modeled NEE is close to the mean NEE between the two sites. SYL, HRV, and HOW all have a considerable seasonal cycle with increasing uptake through the

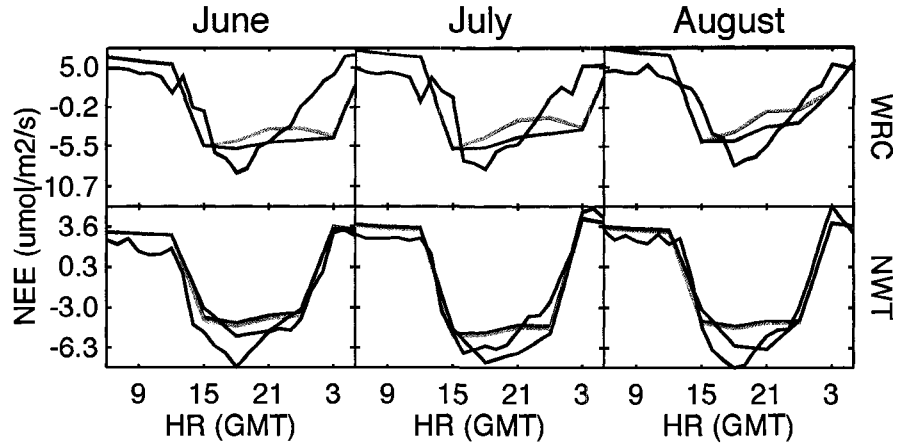


Figure 5.6: Monthly diurnal composites of the NEE at needleleaf forest sites.

summer that is not well captured in the model. One contributing factor to the model underestimation may be humidity stress, which reaches moderate values in the day during some periods in July and August at all three sites; however it is unlikely that the stress is causing the magnitude of the underestimation seen in the model. Observations at HRV indicate that this site is a strong sink due to forest regrowth following a disturbance in the 1930s. Since the model is forced to balance carbon over a year, it cannot simulate the sink at this location and thus underestimates the summertime uptake.

Monthly plots of diurnal composites at grassland and crop sites are displayed in Figure 5.8. At the LBR grassland site, the C3 simulation matches the observations reasonably well, as the dominant grasses at the site are C3. The model captures the diurnal cycle well during May, June, and August but underestimates the flux in July due to mid-day temperature stress. The C4 and PAT simulations switch the dominant biome at the site to C4 grasses, thus degrading the fit at the tower.

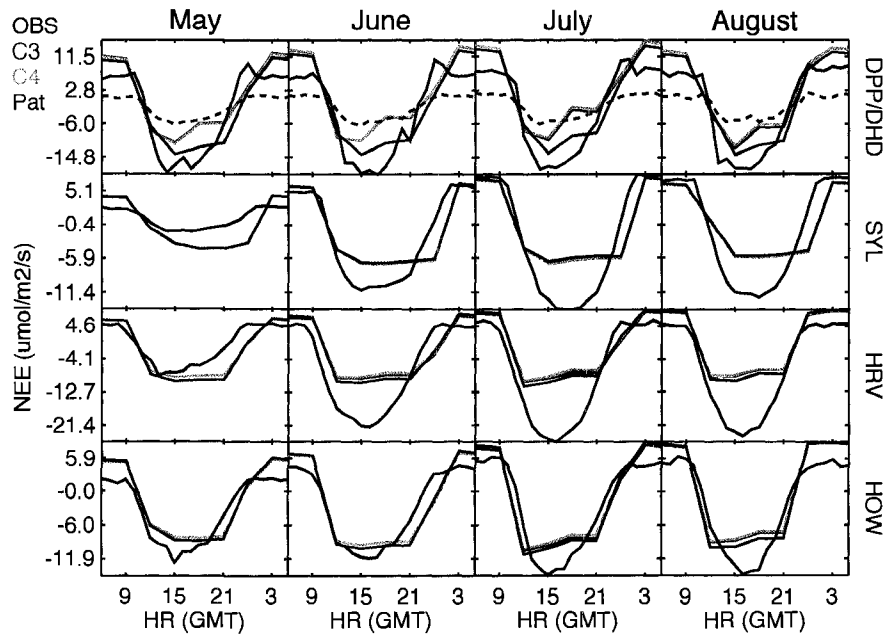


Figure 5.7: Monthly diurnal composites of the NEE at mixed forest sites. In the third row at the Duke Forest sites, the solid line displays the fluxes from DPP while the dashed line shows the NEE at DHD.

C4 vegetation removes the stress seen in C3 vegetation, but overestimates the daytime drawdown. At the SGP site, the model is dominated by two flaws: too much respiration at night for May through August and too much temperature stress during the day reducing the photosynthesis. The stress may be enhanced at SGP due to a low albedo at the site, causing the surface temperature to be overestimated due to the absorption of excess shortwave radiation (Philpott, 2006). At MEAD, the model underestimates the drawdown during August and does not capture the correct seasonality, with too much assimilation in the spring and not enough in late summer. These discrepancies are caused by a mismatch in the LAI/FPAR data, which are too high in May and too low in August.

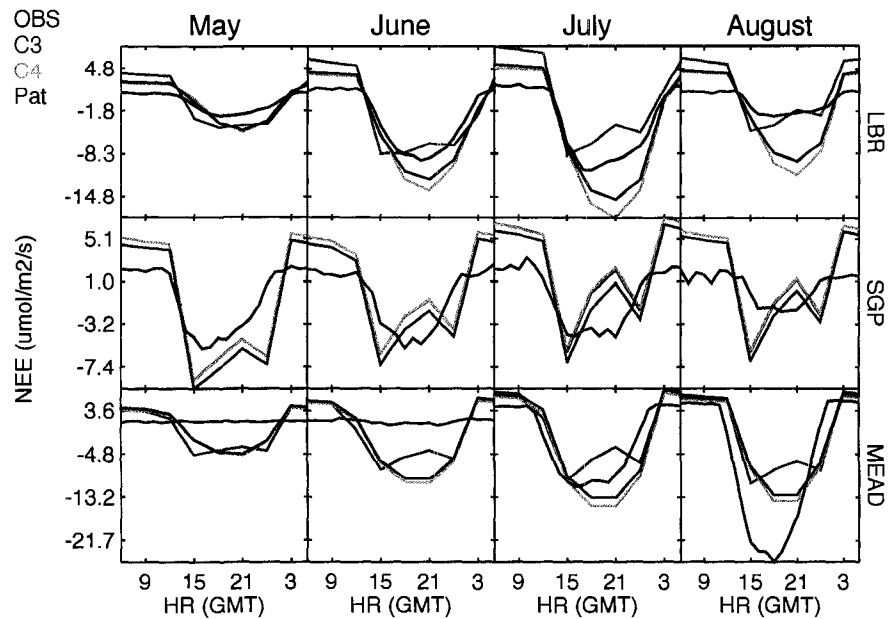


Figure 5.8: Monthly diurnal composites of the NEE at crop and grassland sites.

5.3.2 CO₂ Tower Comparisons

Daytime and nighttime root mean square errors (RMSE) for each of the towers and for all three simulations are displayed in Figure 5.9. The magnitude of the daytime errors is much less than at night. At all tower sites, using patches improves the concentration timeseries. The daytime mean RMSE for the C3 simulation is 6.8 ppm, and using C4 vegetation and patches reduces the mean daytime RMSE across all towers to 5.9 ppm. The mixed forest sites have the largest errors both during the day and at night, particularly HRV. The large errors at HRV, AMT, and HOW are caused by offsets seen in the concentration timeseries: SiB3-RAMS has too high concentrations in July and August. The offset is likely caused by the incorrect seasonality and the underestimation of the drawdown through this

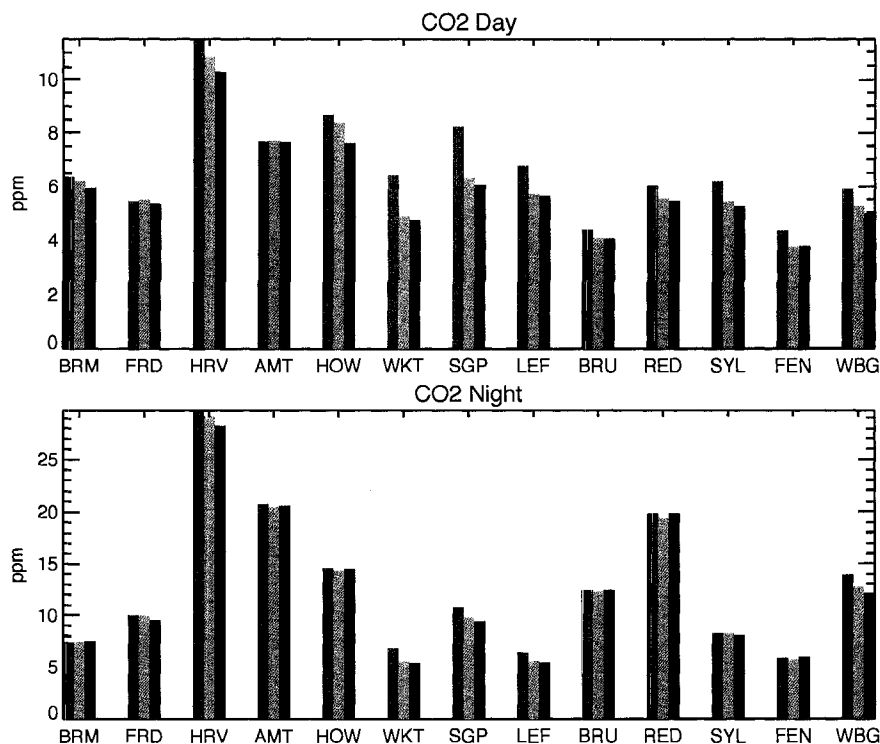


Figure 5.9: Root mean square errors at each of the tower sites for the mean daytime concentrations (top panel) and the mean nighttime concentrations (bottom panel). Daytime hours are from 1800 UT to 0000 UT and nighttime hours are from 0300 UT to 1200 UT. Red=C3 simulation, Green=C4 simulation, Blue=Patches simulation.

northeast region. The errors are particularly large at night from extreme buildup of CO_2 in the nocturnal boundary layer. Differences in the RMSE can be seen in the Ring of Towers despite the relative close proximity of those towers, indicating that local influences between the towers alter the concentrations.

A Taylor plot of the daytime CO_2 concentrations is shown in Figure 5.10 (Taylor, 2001). The model has skill at calculating CO_2 concentrations, as the majority of the towers have a fitness score of 0.8 or greater. The correlations between the model and the data are high, indicating the model is doing a reasonable job at

capturing the seasonal and synoptic scale variability. The normalized standard deviations at the majority of the sites is also near 1.0, indicating the model is capturing the correct variance seen in the observations. The figure also shows that including patches increases the fitness at all the towers, either by increasing the correlation or shifting the normalized standard deviation towards 1.0. The three outlier sites are H=WKT, S=HRV, and I=SGP. The correlations are low at WKT due to missing data in June and August. The correlations are low at Harvard Forest due to the offset discussed previously. At SGP the standard deviation in the model is too low. This could be caused by underestimation of the uptake during the day from the stress seen in the model fluxes at the site, as well as the underestimation of the uptake in croplands seen in SiB3-RAMS.

5.3.3 Distribution of the Net Ecosystem Exchange

The mean NEE for the growing season, May through August, for the PAT case is displayed in Figure 5.11. During the growing season, the majority of the U. S. is a sink for CO₂, except the south-eastern states where CO₂ is being released. The largest uptake occurs in the central Great Plains, through Oklahoma and Nebraska, and in the upper Midwest, centering around Michigan. The boreal forest is neutral to a weak sink of CO₂ during the summer; however, a region in northern Alberta, Canada is a source during the growing season. The summertime release of CO₂ is not due to stress, but rather is caused by high summertime respiration. The

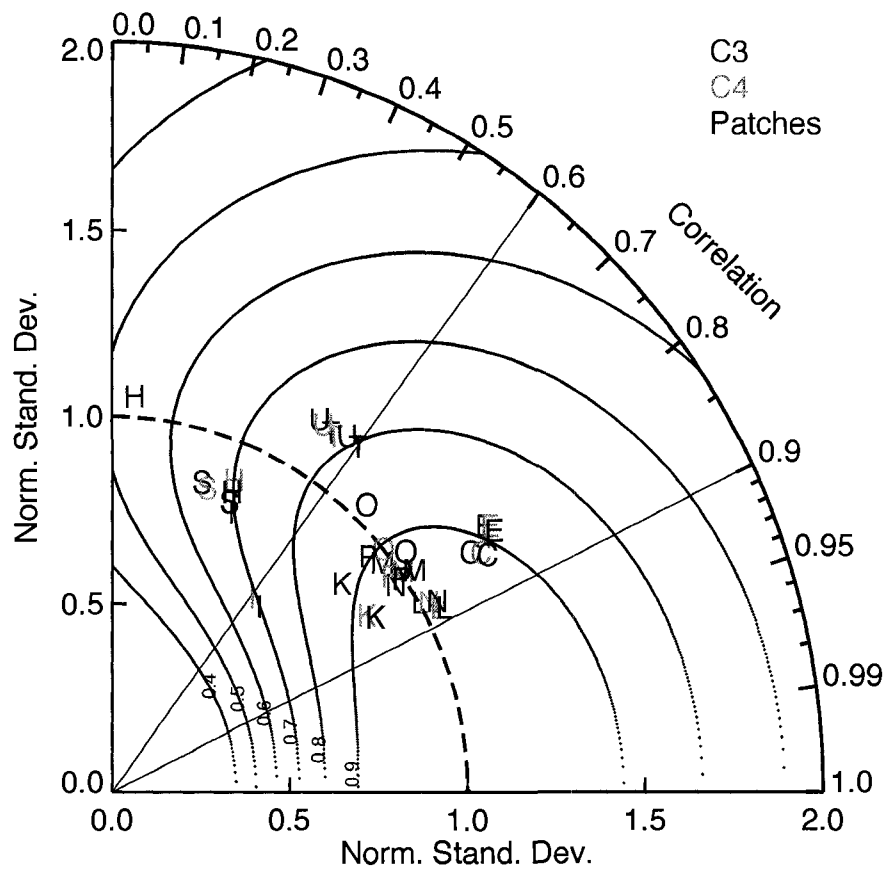


Figure 5.10: Taylor plot of the daytime mean CO₂ concentrations.

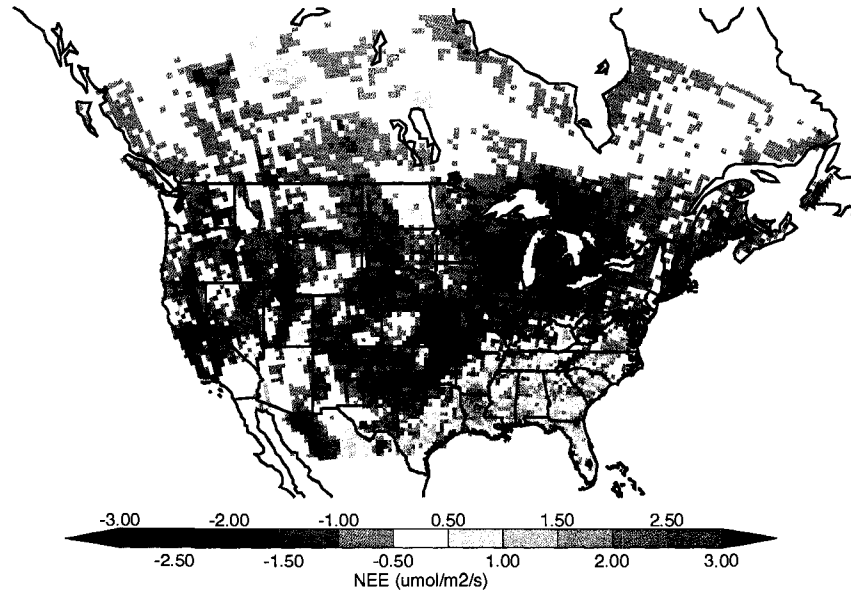


Figure 5.11: Map of the mean NEE from May through August, 2004. The results shown are from the PAT simulation, using both C4 vegetation and patches.

positive NEE seen from Texas up through Virginia is also due to high respiration, rather than plant stress due to humidity, soil moisture or temperature.

Changing the vegetation cover alters the NEE. Figure 5.12 shows the differences between using C4 versus C3 vegetation and the differences from adding patches. Including C4 crops and grasses increases the summertime sink of carbon throughout much of the United States, with changes over $3 \mu\text{mol m}^{-2} \text{s}^{-1}$ in some regions. Using C4 vegetation has the greatest impact on NEE through the Great Plains and western U. S., where a high fraction of the region is covered by C4 grasslands.

Adding patches to the model also modifies the NEE compared to only using the dominant vegetation in each grid cell. Patches moderate the enhanced uptake with C4 vegetation seen in Texas and up through the central Great Plains. The

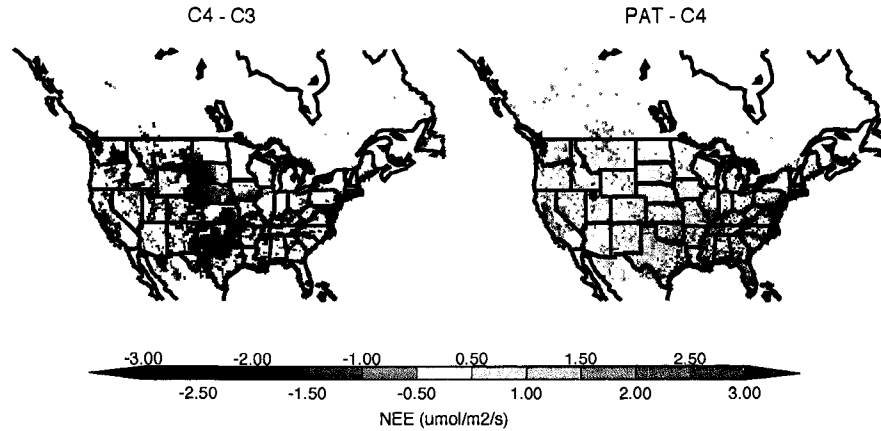


Figure 5.12: Maps of the differences between the mean NEE between simulations. The left hand panel shows the differences between the C4 simulation and the C3 simulation, and the right hand panel displays NEE differences between the PAT and C4 simulations.

decrease in NEE seen between PAT and C4 is due to including the mixture of C3 and C4 grasses and crops found through this region. Increases in the net uptake from using patches are seen in the southeast, with changes up to $1 \mu\text{mol m}^{-2} \text{s}^{-1}$. Changes through this region are not surprising, since the areal coverage of vegetation was relatively evenly distributed between deciduous forest, mixed forest, C3 grasses and C4 grasses rather than the region being dominated by one specific biome. Significant changes in NEE can also be seen in California. Changing much of the vegetation to C4 substantially increased the photosynthetic uptake, and adding patches reduced the magnitude of the changes caused by using C4 as the dominant vegetation, resulting in a moderate sink during the growing season.

Monthly maps of NEE for the PAT, C4, and C3 simulations are shown in Figure 5.13. In May, the boreal forest is a source of CO_2 while the majority of the

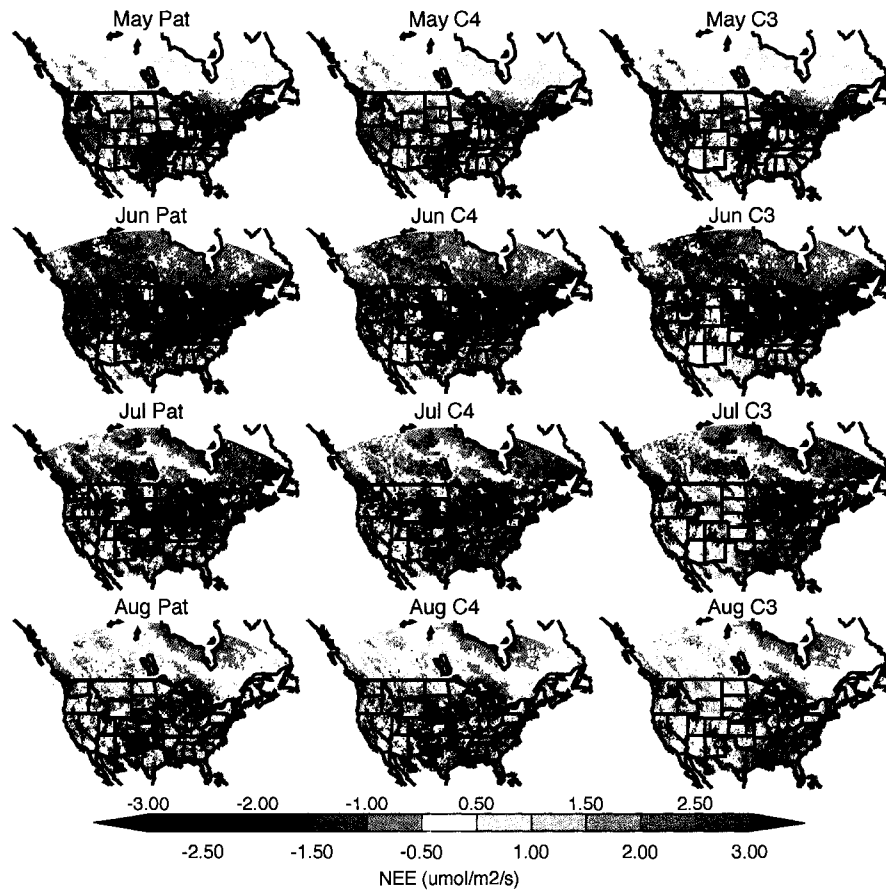


Figure 5.13: Maps of the monthly mean NEE for each simulation.

continental U. S. is a sink, with the exception of croplands in Iowa and Nebraska. Using patches increases the uptake seen in the southern states and decreases the sink in Texas and Oklahoma compared with using only dominant vegetation. If C4 vegetation is not included, the southern states become sources of CO₂ and the uptake of CO₂ is reduced throughout the southern Great Plains. The Pacific Northwest also has less uptake in the C3 simulation.

In June nearly all of North America is taking up CO₂. The greatest assimilation of CO₂ occurs in the central Great Plains and northern Midwest. If patches are

not used, the Great Plains become dominantly covered by C4 and have enhanced uptake, while reduced uptake occurs through the deep south due to the lack of heterogeneity in land cover. Not including C4 vegetation decreases the uptake seen throughout much of the western and central U. S.

Moving to July, much of NA is still a sink, although regions where CO₂ is being released can be seen, particularly through the northwestern states. The southern states are strong sources of carbon, while regions in the Great Plains are strong sinks. Similar to the pattern seen in June, not including patches increases the magnitude of the source in the southeast while enhancing the uptake through Texas. Not including patches also results in regions through Montana and Wyoming to become sources. Not using C4 vegetation significantly reduces the CO₂ uptake, causing much of the western Great Plains to become a source.

In August, the uptake is reduced as the growing season ends. Many of the southern and eastern states are sources of CO₂, as is a large region of the boreal forest. The majority of the western and central U. S. is still taking up CO₂, although the magnitude of the drawdown has decreased. Not including patches has nearly the same effect as in July: an enhanced sink throughout the southern portions of the Great Plains and enhanced sources through the southeast. Using only C3 vegetation and not including patches results in the northwestern states releasing more CO₂ and extends and enhances the sources regions in the southern and eastern U. S.

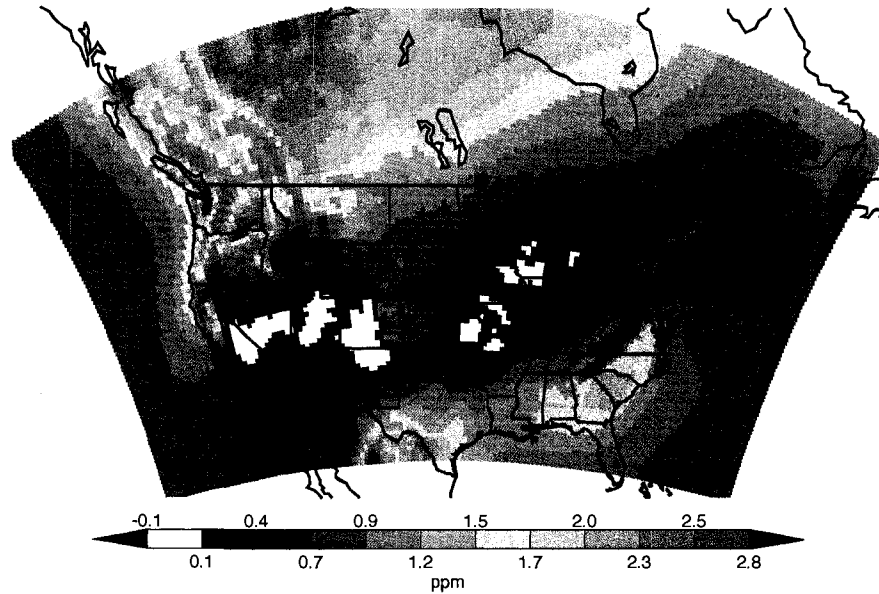


Figure 5.14: Total column CO₂ concentrations due only to biological fluxes.

5.3.4 CO₂ Maps

A map of the mean May through August total column CO₂ concentration due only to the biological fluxes for the PAT simulation is shown in Figure 5.14. As expected, the spatial pattern of CO₂ is similar to the NEE map: high contributions of CO₂ to the atmosphere occur in the southeast, where the vegetation is releasing carbon, while lower concentrations are seen over the central and midwestern states. High total column CO₂ is also seen in western Canada due to the high respiration in the region.

Differences in the mean total column CO₂ between C3 and C4 and between C4 and PAT are displayed in Figure 5.15. Using C4 vegetation results in reduced CO₂ in the total column over all of NA. The differences are greatest over the Great

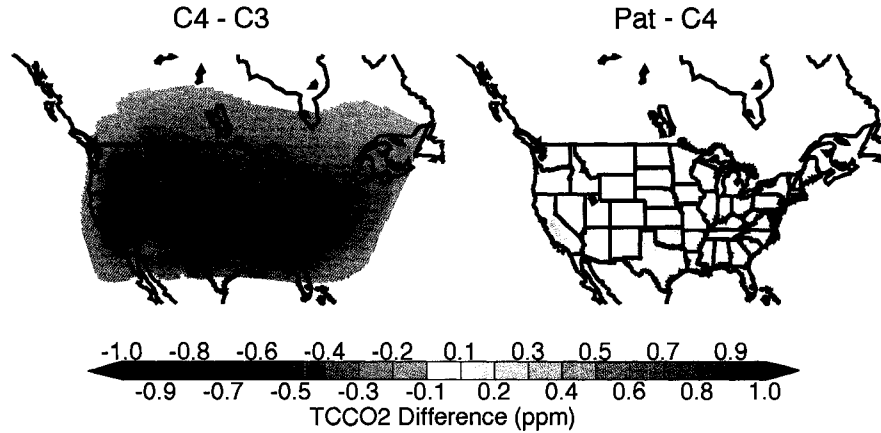


Figure 5.15: Differences between the total column CO_2 concentrations. The left hand panel shows the differences between C4 and C3 simulations. The right hand panel shows the differences between PAT and C4 simulations.

Plains, where the mean column CO_2 is reduced by more than 1 ppm from including C4 vegetation. Larger differences can also be seen over Nevada and in California. Adding patches slightly increases the mean total column CO_2 compared to the C4 simulation over both California and in northern Texas and Oklahoma. The rest of the NEE changes do not alter the total column CO_2 in the 4-month time mean.

Monthly differences in the total column CO_2 between the PAT, C4, and C3 simulations are shown in Figure 5.16. In May, the mean total column CO_2 over the northwestern U. S. is higher when C4 is included in the land cover. Although a large region of reduced uptake is not readily apparent in the NEE map, the atmosphere integrates the contributions from individual grid cells to increase the total column CO_2 in the C4 simulation. The C4 run also has lower total column concentrations in the eastern U. S. Differences in the mean total column concentration between using dominant vegetation versus including patches are minimal.

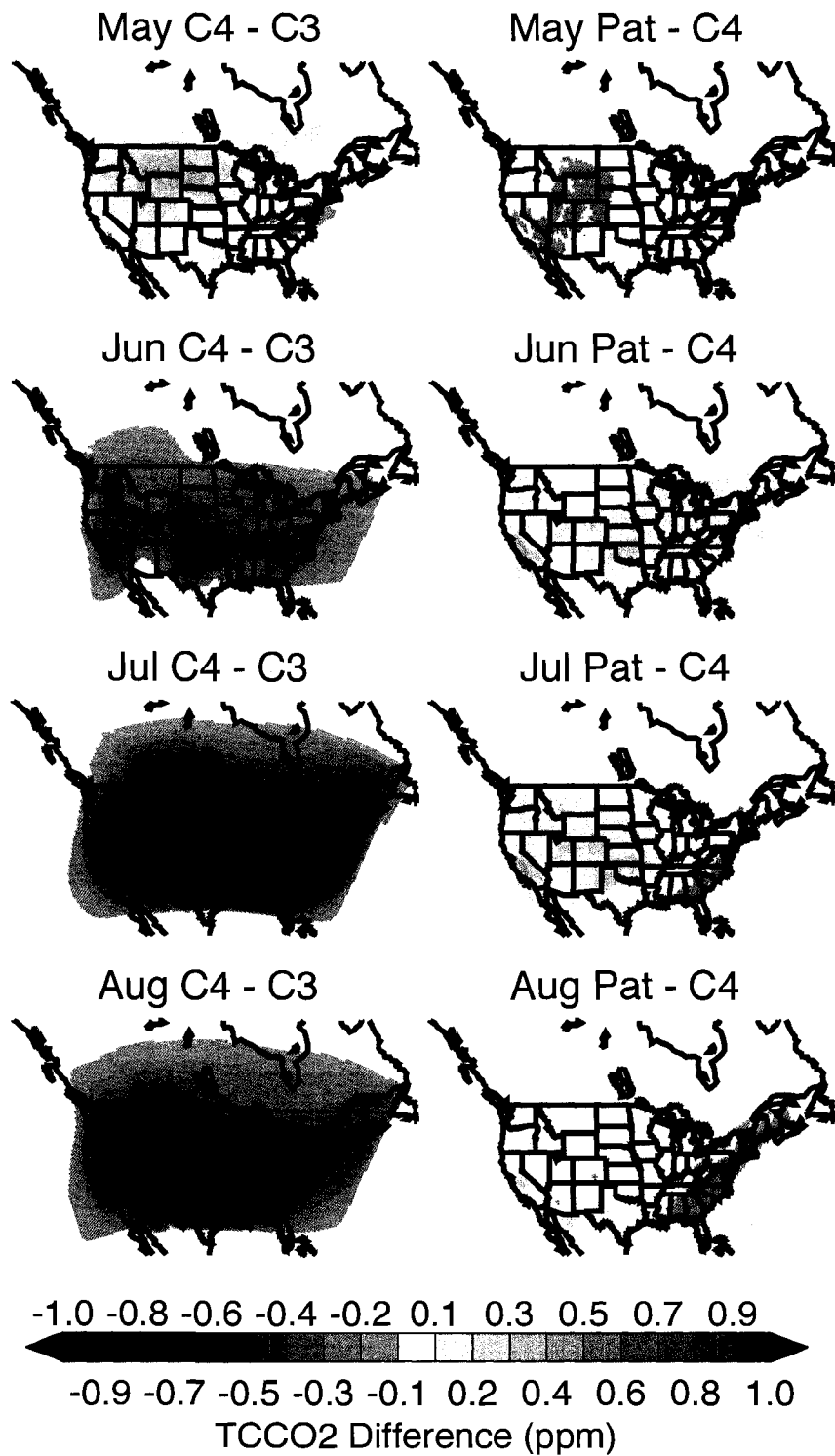


Figure 5.16: Maps of the differences between the simulations for each month. The left hand column shows the differences between the C4 and C3 simulations, while the right hand column shows the differences between the PAT and C4 simulations. May is in the top row and August is in the bottom row.

The run with patches has slightly lower CO₂ over the western U. S., which again results from the integration of slightly enhanced uptake from individual grid cells that include heterogeneous vegetation.

Patterns in the differences between PAT, C4, and C3 are similar for June, July, and August. Using C4 vegetation lowers the total column CO₂ over the entire U. S. The maximum differences occur in July, corresponding to the month with the largest NEE differences, and the differences reach up to 2 ppm in the total column. Adding patches reduces the total column CO₂ over the central and western U. S., with the greatest differences in July occurring over California and the Great Plains. In July and August, total column CO₂ in the southern and eastern U. S. is \sim 0.1-0.3 ppm lower due to including land cover heterogeneity.

5.3.5 Sources of Atmospheric CO₂ Concentrations

SiB3-RAMS includes a variety of sources as well as individual atmospheric CO₂ tracers for each of the sources, and the contribution from each of the sources can be analyzed. The CO₂ sources included in the model are lateral boundary concentrations from a global model, biological surface fluxes, fossil fuel emissions, fire emissions, CO₂ produced from CO oxidation, and ocean fluxes. Figure 5.17 displays maps of the mean 30 m CO₂ concentrations resulting from each of these sources. A map of the contribution of ocean fluxes is not included as the resulting CO₂ contribution was $<$ 0.01 ppm.

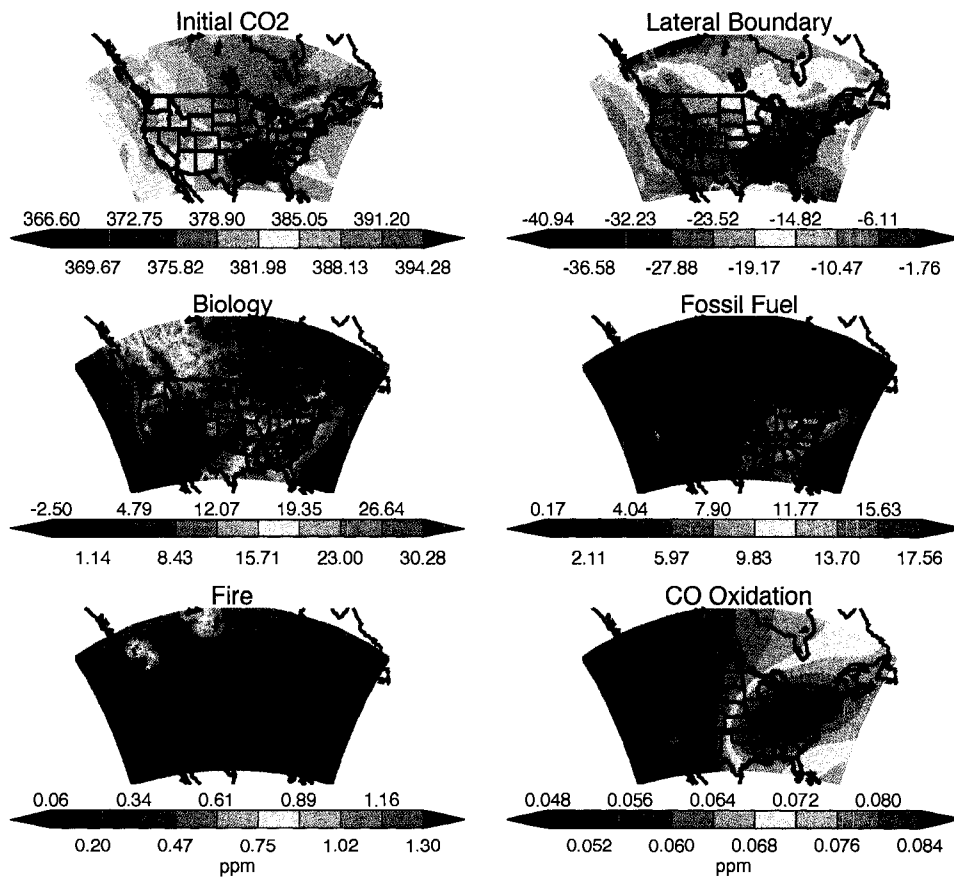


Figure 5.17: Maps of the May through August mean contribution of individual sources to the total atmospheric CO₂ concentration, at 30 m. The top left panel shows the initial CO₂ concentration on May 1. All maps have units of ppm and use the concentrations from the PAT case.

The dominant contributors to the atmospheric CO₂ concentrations over North America are the lateral boundary concentrations, the biological fluxes and the fossil fuel emissions. The concentrations from the lateral boundaries act to lower the total CO₂ concentration, particularly over the northern U. S. and the Gulf of Mexico. The smallest impact from the lateral boundary conditions is over the central and southern portions of the United States, where on average the lateral boundaries alter the CO₂ concentration by less than 5 ppm near the surface.

The biological fluxes alter atmospheric CO₂ concentrations during the summer by as much as 30 ppm on average. Higher concentrations are seen over the southeastern U. S., which was a source of CO₂. In Canada, the biology also contributes ~ 20 ppm to the mean concentration. Lower contributions occur over the central and western portions of the U. S, where the fluxes are weaker.

The mean impact of fossil fuel emission on CO₂ concentrations is approximately half of the magnitude of the changes due to the biology. As expected, the map of CO₂ concentrations resulting from fossil fuel matches the emissions map with higher concentrations in the east coast and California, where the CO₂ concentration increases by ~ 10-15 ppm due to anthropogenic emissions.

Both fire emissions and the source of CO₂ from the oxidation of CO are minor contributors to the overall CO₂ concentration. Two centers of high CO₂ from fires can be seen over Canada, contributing over 1 ppm near the surface on average. Although this source is small on average, fire emissions are likely important on shorter timescales while the fire is burning, particularly in the boreal forest where

more fires occur. Unfortunately, the majority of the boreal fires during the 2004 summer were further north and not included in the simulation.

The impact of CO oxidation to the CO₂ concentration is minimal in this simulation, causing mean changes of < 0.1 ppm near the surface. Unlike the previous sources where the flux is at the surface, the CO contribution occurs in the atmosphere; however, this source of CO₂ concentrations remains minimal at all vertical levels. The contribution from CO oxidation is highest over the eastern half of the country, where there are more fossil fuel emissions and hence more CO. Over the western U. S., the CO₂ concentration increase from the oxidation of CO is less than 0.05 ppm.

5.4 Conclusions

Substantial modifications have been made to SiB-RAMS: SiB was updated to version 3.0, respiration factors are now calculated for every grid cell from offline runs, CO₂ is initialized and lateral boundaries are nudged to global concentrations, high resolution fossil fuel emissions are included, fire emissions and CO contributions are included, and land cover patches are included to represent sub-grid surface heterogeneity. This study focused on an evaluation of the NEE and CO₂ concentrations in the model, as well as the impact of land cover.

While SiB3-RAMS does a reasonable job simulating fluxes at needleleaf and grassland sites, NEE comparisons at several towers within specific biome types

reveal several deficiencies that still exist in SiB3-RAMS. SiB3-RAMS overestimates the summertime respiration at boreal forest sites, and the model does not capture the correct seasonality in the fluxes at mixed forests and croplands. At mixed forest sites in the north-eastern U. S., the daytime flux is underestimated during July and August. One cause for this underestimation may be that these regions are sinks of carbon that are not represented by SiB3-RAMS since it is a balanced model, and another contributing factor may be daytime humidity stress. At a C4 cropland site, the model overestimated the drawdown during the spring and underestimated the uptake in July and August due to remotely sensed LAI data that did not match the specific crop field being measured. At a C3 crop site, daytime assimilation was underestimated due to temperature stress in SiB3-RAMS.

Adding sub-grid heterogeneity has a relatively significant impact on the fluxes and mean NEE across North America, with changes over $3 \mu\text{mol m}^{-2} \text{s}^{-1}$. The most significant changes occur in the Great Plains and in the southeast. The Great Plains and Midwest has a large contribution of C4 grasses and crops, which are characterized by high water-use efficiency and reduced temperature stress; and including C4 vegetation increases the summertime sink across these regions. In the southeast, using patches decreased the source of CO_2 from including the land-cover heterogeneity.

SiB3-RAMS captures the seasonality and the synoptic variability in CO_2 reasonably well; however larger differences occur between the model and the observations in the northeast because of offsets in the model. SiB3-RAMS has high

concentrations in this region which likely result from the underestimation of daytime uptake that was seen in the NEE comparisons. In addition, large nighttime errors are due to an overestimation of the buildup in high nighttime concentrations. Comparisons between modeled and observed CO₂ concentrations reveal that including both C3 and C4 vegetation as well as sub-grid land cover heterogeneity improves the model performance, reducing RMSE errors by ~ 1 ppm on average.

Acknowledgements

We sincerely thank all the data providers. We thank Larry Flanagan at the University of Lethbridge for the WPL and LBR data, Doug Worthy at the Meteorological Service of Canada Air Quality Research Branch for the FRD and BRM data, and Steve Wofsy from Harvard University for the BOR data. For the Ameriflux data, we thank Sonia Wharton at the University of California Davis for the WRC data; Russ Monson at Colorado University for the NWT data; and Shashi Verma at the University of Nebraska Lincoln for the MEAD data. We thank Margaret Torn and Marc Fischer from Lawrence Berkeley National Laboratory for the SGP data. Data at the SGP site were obtained from the Atmospheric Radiation Measurement (ARM) Program sponsored by the U. S. Department of Energy, Office of Science, and Office of Biological and Environmental Research.

We thank Ken Davis for the LEF data and for the data from the Ring of Towers. The carbon dioxide mixing ratios at the LEF tower are maintained by the National Oceanographic and Atmospheric Administration. Flux measurements at the LEF

tower were supported by the Department of Energy's Office of Science through the National Institutes for Global Environmental Change and the Terrestrial Carbon Processes Program.

We also wish to thank Ankur Desai at the University of Wisconsin for the SYL data. Thank you to Gaby Katul and Ram Oren for providing the Duke Forest data, which was funded by the U. S. Department of Energy (DOE) through the Office of Biological and Environmental Research (BER) Terrestrial Carbon Processes (TCP) program (Grants 10509-0152, DE-FG02-00ER53015; and DE-FG02-95ER62083). We thank William Munger and Steve Wofsy at Harvard University for HRV data, and David Hollinger with the USDA Forest Service for the data at HOW. We thank Arlyn Andrews at NOAA/ESRL/GMD for the WKT and AMT data and the World Meteorological Organization (WMO) World Data Center for Greenhouse Gases (WDCGG) and NOAA/ESRL/GMD for making the CO₂ data at these towers publicly available.

This research was funded by the National Aeronautics and Space Administration (NASA) contracts NNX06AC75G and NNG05GF41G.

6 Effects of Agricultural Production on Regional Variations of Atmospheric CO₂ Concentrations

Abstract

The North American Carbon Program (NACP) Mid-Continent Intensive Campaign (MCI) sponsored measurements of atmospheric concentrations at five towers centered over Iowa during the summer of 2007. We simulated both CO₂ fluxes and concentrations for June through August 2007 using the coupled ecosystem-atmosphere model SiB3-RAMS, focusing on the concentrations over the MCI region. To improve CO₂ fluxes in this region, we coupled a crop phenology model to SiB3-RAMS, which calculates the leaf area index (LAI), fraction of photosynthetically active radiation absorbed by the plants (FPAR), and net ecosystem exchange (NEE) for both corn and soybeans. Including the crop model dramatically improved the concentrations at all the towers, reducing the root mean square errors by nearly half. Concentrations as low as 340 ppm were seen both in the model and in the observations. The CO₂ gradient between the towers increased

throughout the summer until mid-August and had considerable day-to-day variability. The model simulation showed that large changes in the CO₂ differences between the towers were due to a large-scale gradient between high concentrations to the south of the MCI region and low concentrations to the north. During the 2007 summer, the southeast United States experienced record temperatures and a severe drought, causing the region to be a large source of CO₂ and creating high concentrations. Depending on the synoptic conditions, the large-scale gradient shifted across the MCI region, creating the large day-to-day variability seen in the differences among the towers.

6.1 Introduction

Since CO₂ is the second most important greenhouse gas in the Earth's atmosphere after water vapor, it is an important atmospheric constituent that affects the climate. Atmospheric CO₂ concentrations have increased by more than 30% over the past two centuries due to fossil fuel emissions and land use changes; however, only approximately half of the human-induced emissions have remained in the atmosphere (Denman et al., 2007). The CO₂ growth rate is lower due to the ocean and the terrestrial biosphere taking up a significant amount of anthropogenic CO₂, but the distributions of these sinks and the mechanisms driving them still remain uncertain.

To determine both the spatial and temporal structure of terrestrial carbon fluxes, the scientific community has utilized two different approaches: bottom-

up methods that use in situ data to estimate regional fluxes and top-down atmospheric inversions that use variations in measured atmospheric concentrations to infer sources and sinks. Inventory measurements provide a detailed assessment of changes in carbon stocks from which atmospheric fluxes can be calculated (Dixon et al., 1994; UN-ECE/FAO, 2000; Nabuurs et al., 2003); however, inventory data generally fall short of full carbon accounting; consideration of belowground biomass, soil carbon, litter and the fate of forest products is inconsistent; spatial and temporal heterogeneity is high and not fully accounted for; and obtaining broad spatial coverage is very labor intensive (House et al., 2003; Denman et al., 2007). Process-based models are used in conjunction with inventory data to extrapolate flux observations into regional estimates (Rayner et al., 2005; Pacala et al., 2001a; Goodale et al., 2002; Janssens et al., 2003). A direct flux measurement approach uses the eddy covariance technique to measure CO₂, water and energy fluxes between the biosphere and the atmosphere. This technique is utilized in various regional networks (e.g. Baldocchi et al., 2001; Aubinet et al., 2000; Margolis et al., 2006). One limitation of this methodology is that the fluxes have a very small footprint (< 1 km²) and are only representative of local fluxes, although flux measurements combined with remotely sensed properties are being used to extrapolate flux observations into regional estimates (Gilmanov et al., 2005; Falge et al., 2002; Turner et al., 2003).

An alternative method to the bottom-up approach is inverse modeling, by which the distribution of regional fluxes can be retrieved using observations of

atmospheric CO₂ and related tracers within models of atmospheric transport (the top-down approach as implemented by Enting et al. (1995); Gurney et al. (2002); Rodenbeck et al. (2003)). Prior knowledge of fossil fuel sources and estimates of the fluxes and their uncertainty ranges are required to constrain the results. Inverse modeling has the attraction that it estimates the total net flux generated by the sum of all mechanisms and has smaller uncertainties at large scales; however, measurement and modeling errors, uneven and sparse coverage of the data network, and errors in transport can introduce errors into the flux estimates (House et al., 2003; Denman et al., 2007).

Comparing and reconciling bottom-up regional fluxes with inversion flux estimates is difficult: inversion fluxes may utilize information from bottom-up fluxes making the estimates not fully independent, the time period for which inversion models and bottom-up estimates are compared is often not consistent, the land area represented by the fluxes may differ, and inversions of CO₂ data produce estimates of CO₂ fluxes which will differ from estimates of carbon fluxes due to oxidation of reduced carbon compounds. Due to these difficulties, robust findings have been reported only for large-scale regions (Denman et al., 2007; Pacala et al., 2001a; House et al., 2003). As the atmospheric CO₂ observation network expands and computing resources improve, the focus of flux estimates is shifting from large-scale to smaller regional scale estimates with a higher temporal resolution.

To fully understand the fluxes and the processes driving them, it is essential to evaluate both top-down and bottom-up flux estimates. To compare and rec-

oncile regional fluxes on hourly to annual time-scales using top-down atmospheric budgets versus bottom-up ecosystem model-based inventories and to identify the mechanisms governing these fluxes, the North American Carbon Program (NACP) is funding the Mid-Continent Regional Intensive Campaign (MCI) centered over Iowa (Figure 6.1, Ogle et al. (2006)). As part of the MCI campaign, the National Oceanic and Atmospheric Administration's (NOAA) tall-tower and aircraft trace gas sampling network was expanded with atmospheric measurements from radio tall towers and numerous aircraft profiles. CO₂ concentrations in the MCI region began in spring 2007. In addition to atmospheric concentrations, the MCI campaign funded dense inventory and flux measurements throughout the summer and fall. The region also hosts relatively dense networks of eddy-covariance flux towers, several long-term agricultural experimental sites with time-series of carbon stocks, forestry data collected through the United States Department of Agriculture (USDA) Forest and Inventory Analysis (FIA) program, annual crop yield data collected by USDA National Agricultural Statistics Service (NASS), and fossil fuel emissions estimates from the Environmental Protection Agency (EPA) Fuel Emission Statistics (Ogle et al., 2006).

The dense network of data from the MCI can be used for a variety of modeling studies, not only to investigate the carbon fluxes, but also to enhance our knowledge of the carbon cycle. Regional models provide a way to quantitatively map sources and sinks of CO₂ using many different observations (i.e. soil maps, vegetation maps, topography, meteorology). Many of the fields independently

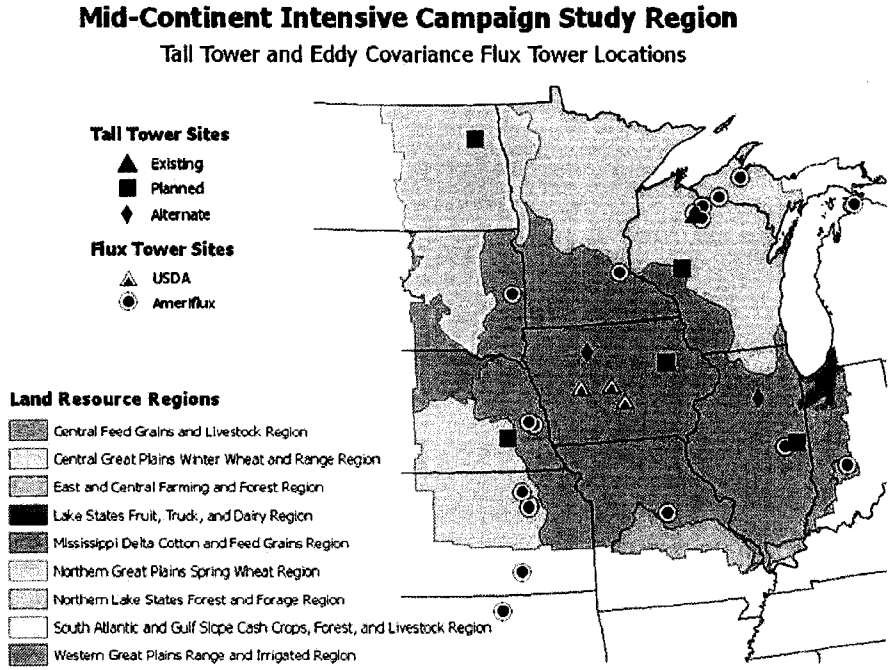


Figure 6.1: The Mid-Continent Intensive Campaign (MCI) Study Region.

measured during the MCI campaign are predicted by forward models, and model-data comparisons lead to the advancement of our understanding of the processes and mechanisms driving the variability in these fields. In addition to providing atmospheric inversions with initial flux estimates that include all known mechanisms, coupled ecosystem-atmosphere models can help interpret the high-frequency variability in CO₂ concentrations. Since atmospheric CO₂ concentrations contain information about sources and sinks of carbon, understanding the mechanisms driving the CO₂ variability will help us better estimate carbon fluxes.

To evaluate and analyze concentrations, it is essential that the fluxes are modeled as accurately as possible using all the processes currently understood. Since the MCI campaign is over a region that is heavily farmed for corn and soybeans, it

is important that fluxes of these crops match observations. To model corn and soybean fluxes, Lokupitiya et al. (2008) developed a crop-specific phenology submodel for the Simple Biosphere Model (SiB3crop) that replaces remotely-sensed leaf area index (LAI) and the fraction of photosynthetically active radiation (FPAR) for estimating carbon dynamics. Lokupitiya et al. (2008) showed that using a crop phenology model significantly improved simulated carbon fluxes for these crops.

To improve both CO₂ fluxes and concentrations, we coupled the crop phenology model to the ecosystem-atmosphere model SiB3-RAMS. In this study, we will investigate the impact of the new crop model on atmospheric concentrations and evaluate the modeled CO₂ field against the observations collected during the MCI. In addition, we will investigate causes of the variability in the CO₂ gradient between the towers.

6.2 Methods

6.2.1 Model Description

The base model used in this study is the Simple Biosphere Model Version 3 (SiB3) coupled to the Brazilian version of the Colorado State Regional Atmospheric Modeling System (RAMS). The coupled model is described in Chapter 5. In this section we will only discuss the modifications not included in the previous description, as well as any differences in the model setup.

In order to more accurately simulate crops, we coupled a crop phenology model developed by Lokupitiya et al. (2008) to SiB3-RAMS. The phenology sub-model

includes phenology events and growth stages for both corn and soybeans; and it calculates the leaf area index (LAI), fraction of photosynthetically active radiation absorbed by plants (FPAR), and net ecosystem exchange (NEE) for these two crops. The planting date occurs when the daily mean temperature is above a threshold value for a specified number of days. At emergence, the initial biomass values are based on observed values and a daily LAI is estimated based on the dry weight carbon in the leaves. Throughout the growth cycle, daily increments in carbon are based on SiB's daily photosynthetic assimilate. The daily assimilated carbon added to the plant biomass is allocated to four different pools: roots, leaves, stems, and products (i.e. flowers, grains, etc.). The amount of biomass allocated to each of these pools depends on the number of days since planting and on growing degree days, which are calculated based on the number of days above a threshold temperature. A fraction of the assimilated carbon is released in growth and maintenance respiration. Senescence is induced when the respiration outweighs the daily leaf growth, and the crop is harvested after it reaches physiological maturity, allowing some field drying. Further details of the crop model are described in Lokupitiya et al. (2008).

6.2.2 Model Initialization and Input Data

The meteorological fields, soil map, fossil fuel emissions, and air-sea fluxes are described in Chapter 5. The land cover classification, LAI, and FPAR are remotely sensed data with 1 km horizontal resolution from the Moderate Resolution Imaging

Spectroradiometer (MODIS) satellite on the NASA TERRA platform. The data were filled and processed by the Climate and Vegetation Research Group at Boston University and are available on-line at <http://cliveg.bu.edu/modismisr/index.html> (Lotsch et al., 2003; Myneni et al., 2002). LAI and FPAR data for 2007 were only available with monthly time resolution, and we linearly interpolated the data down to 8-day composites.

The vegetation classes from MODIS were reclassified into SiB classes. We used the C3/C4 percent land cover map with 5 minute horizontal resolution from Still et al. (2003) to discriminate between C3 and C4 crops and grasses. To determine corn and soybean coverage, we used a 56 m resolution map provided by Matt Hansen at South Dakota State University and aggregated the map up to 1 km resolution. The MODIS-trained, Advanced Wide Field Sensor (AWiFS) -based corn and soybean product for 2007 covers Iowa and regions immediately surrounding the state (Figure 6.2). The crop map was created by integrating high temporal resolution data from MODIS with high-spatial resolution data from AWiFS. Using a regression tree analysis, time-series of MODIS data were compared to phenological timing of the development of corn and soybeans trained by AWiFS data to determine the fractional coverage that best matched the observations (Chang et al., 2007).

To include crop and soybean land cover, SiB3-RAMS calculated separate fluxes for three patches per grid cell. The average flux for every grid cell is an areal-weighted average of the flux from each patch. If the MODIS map from Boston

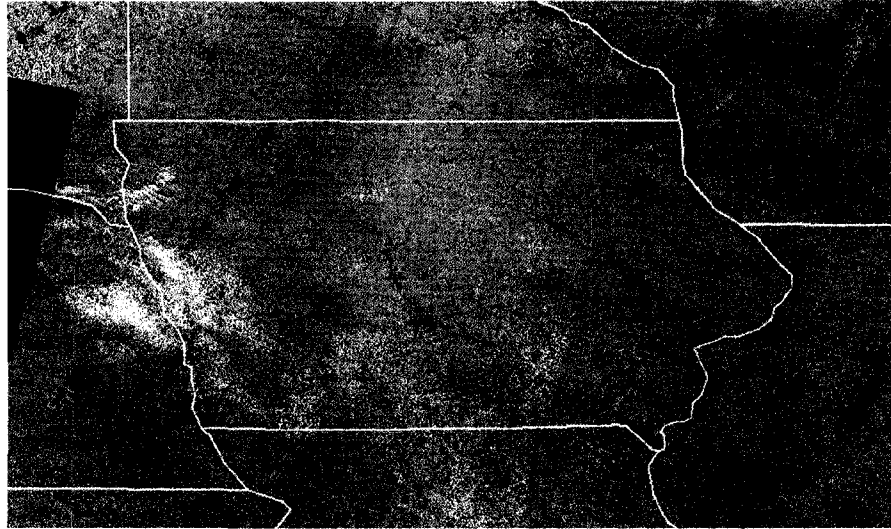


Figure 6.2: Map of corn (green) and soybean (purple) coverage over the MCI region. Provided by M. Hansen.

University had crop as a vegetation class in any of the patches over the MCI region, we utilized the Chang et al. (2007) corn and soy map. The total number of pixels of both corn and soybean were counted to determine the fractional area of coverage for each crop. The fractional coverage was then compared with the patch areas of the three original patch land classes, and the vegetation class was reassigned to the dominant three classes. Once the vegetation types were determined, the areal coverage of the patches was recalculated to equal the original land cover percent from using the original MODIS map alone. It should be noted that the crop map covers a limited area centered over Iowa, and no corn or soybeans were specified in the model outside this limited region.

To initialize respirable carbon, soil moisture, and prognostic variables, we used offline SiB3crop and calculated these values for every gridcell. We ran SiB3crop

for ten years from 1997 through 2007 using meteorological data from the National Center for Environmental Prediction (NCEP) Department of Energy (DOE) AMIP II reanalysis, which was provided by National Oceanic and Atmospheric Administration (NOAA) Physical Sciences Division (PSD) in Boulder, Colorado, USA and is available from their website at <http://www.cdc.noaa.gov> (Kalnay et al., 1996). For the gridcells with crops, the crop type was alternated every other year between soybean and corn. SiB3 is a balanced model, and for every gridcell the carbon assimilated in a year equals the total respiration for the year. For corn and soybeans, we reduced the respiration factor by 40% to account for the harvest and removal of crops (Lokupitiya et al., 2008).

The initial CO₂ field and the lateral boundaries in SiB3-RAMS were set and nudged every day to global concentrations from the Parameterized Chemical Transport Model (PCTM, see Chapter 5 for more details on the model). Since concentrations for 2007 were not available, we calculated monthly mean concentrations from 2003 and 2004 and linearly interpolated these to daily values.

6.2.3 Case Descriptions

In this study, we performed three simulations over North America (NA) with SiB3-RAMS. All three simulations ran from 0000 UT 1 June to 0000 UT 1 September 2007. The coarse grid for all cases had 150 x 90 grid cells with 40 km horizontal grid increments and 46 vertical levels up to 24 km.

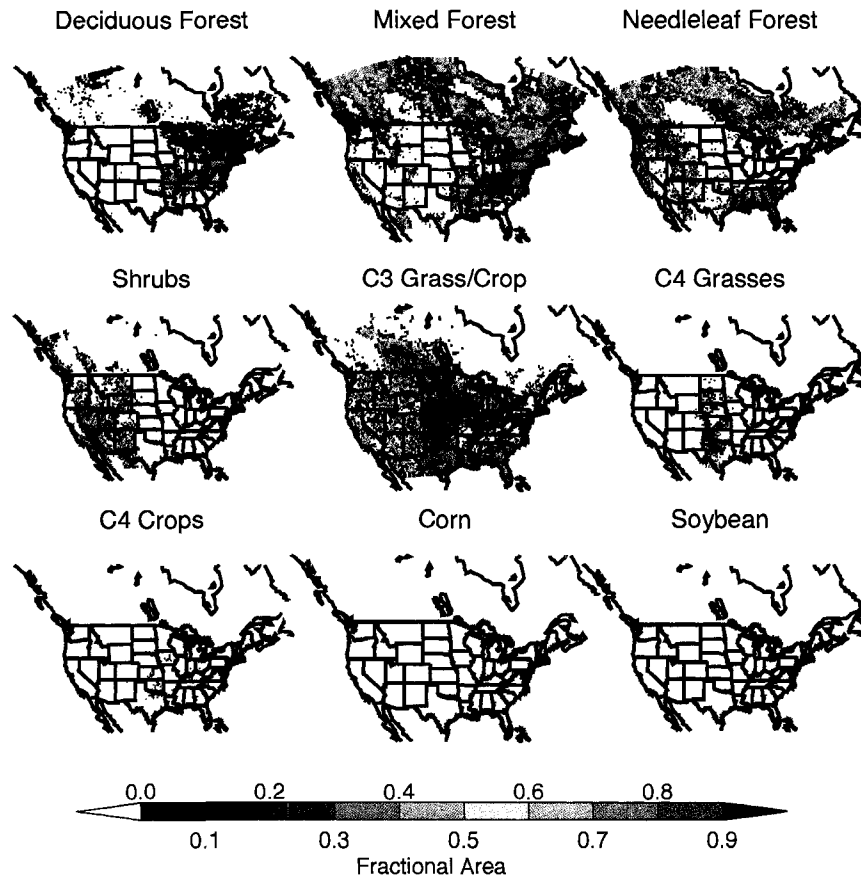


Figure 6.3: Percent land cover classifications for the BASE simulation, which does not include corn and soybean crops explicitly.

The first case, which we will refer to as BASE, used the original SiB3-RAMS and did not use corn and soybean crops. A map of the fractional coverage of each biome class is displayed in Figure 6.3. The majority of the area over the MCI region was classified as C3 grass/crop, with a small percentage covered by C4 grasses and crops.

The second case, NEST, used the crop phenology model and included a nested grid over the MCI region (Figure 6.4). The horizontal grid spacing for the nested

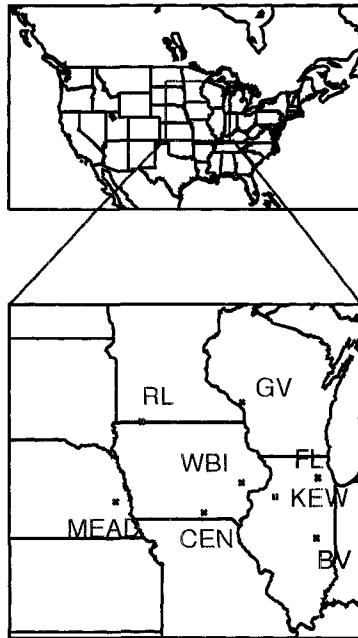


Figure 6.4: Grid setup for the NEST simulation. The interior grid is outlined in red on the coarse domain. The six red crosses indicate the towers in the MCI region that measure continuous CO₂ concentrations, and the purple crosses show the flux towers in the region.

grid was 10 km. The vegetation cover for the coarse grid is shown in Figure 6.5 and the vegetation for the interior grid is displayed in Figure 6.6. On the coarse grid, roughly half of the landcover was corn in the MCI region and approximately 20% of the cover in each gridcell was soybeans. In the nested grid, corn accounted for 60-70% of the vegetation over central Iowa and soybeans covered ten to twenty percent of the area. The regions outside of the crop map were predominantly covered by C3 crops and grasses, except for forest regions in Missouri, Wisconsin, and Minnesota.

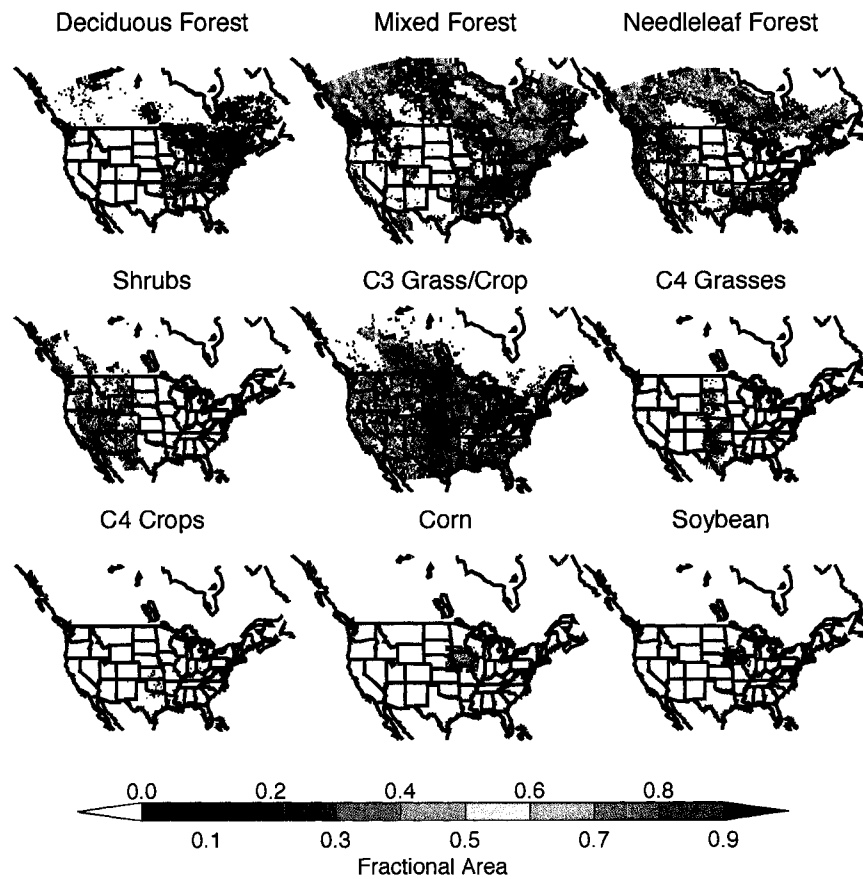


Figure 6.5: Percent land cover classifications including corn and soybeans from the Hansen (2008) crop map.

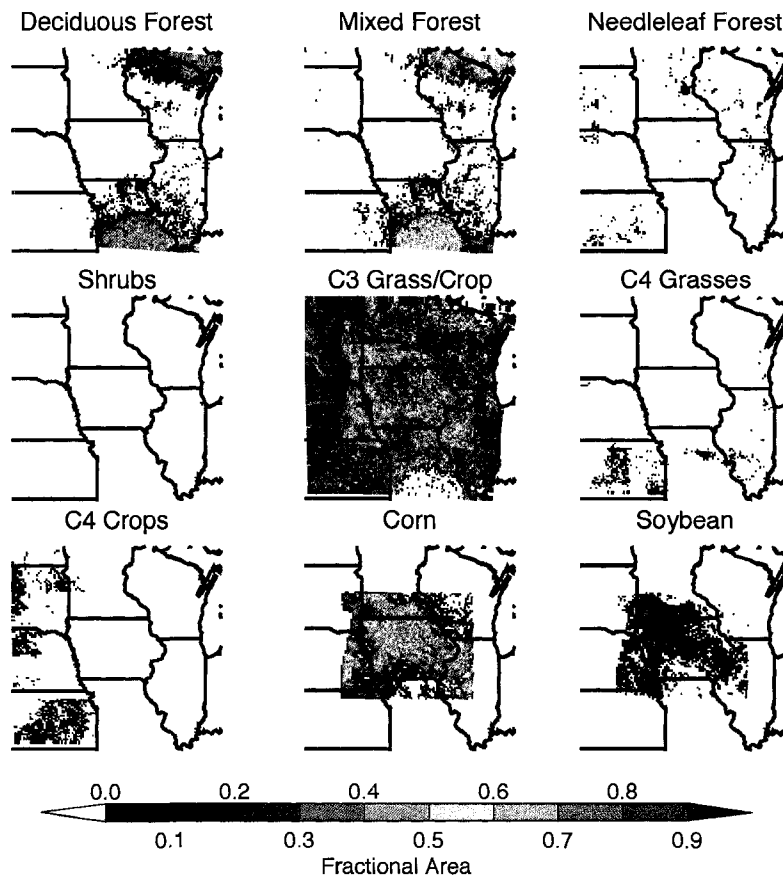


Figure 6.6: Percent land cover classifications for the interior grid of the NEST case, which includes corn and soybeans from the Hansen (2008) crop map.

Ref.	Abrv.	Site	Latitude	Longitude	Sampling Heights
A	MEAD	Mead, NE	41.14 N	96.46 W	20/122 m
B	RL	Round Lake, MN	43.53 N	95.41 W	30/110 m
C	CEN	Centerville, IA	40.79 N	92.88 W	30/110 m
D	WBI	West Branch, IA	41.73 N	91.35 W	31/99/379 m
E	GV	Galesville, WI	44.09 N	91.34 W	30/122 m
F	KEW	Kewanee, IL	41.28 N	89.97 W	30/140 m

Table 6.1: Location and sampling height of each of the towers measuring continuous CO₂ concentrations in the MCI region. The sampling heights are in meters above ground level.

The third case, CROP, used the crop phenology model on the single coarse domain. The vegetation cover for this case is the same as the cover on the coarse grid of the NEST case (see Figure 6.5).

6.2.4 Observations

This study utilized continuous observations of CO₂ concentrations measured at 6 towers in the MCI region (Figure 6.4; Miles and Richardson, personal communication). Table 6.1 states the location and sampling heights at each of the towers. For all the comparisons in this study, we used the tower level that was closest to 120 m.

Five of the towers, MEAD, RL, WBI, CEN, GV, and KEW, are all part of the MCI campaign. To measure atmospheric CO₂, cavity ring-down spectroscopy (CRDS) instruments were deployed. CRDS is a laser-based technique that is able to distinguish individual absorption features by measuring the rate of decay of specific wavelengths of light in the cavity. Advantages to CRDS are that it is very sensitive due to its long path length making the measurements highly accurate, and

it has a reduced need for calibration compared to systems used in the Ameriflux network.

The sixth tower, WBI, is funded by the NOAA Earth System Research Laboratory (ESRL) Global Monitoring Division (GMD), and the data are publicly available at <http://esrl.noaa.gov/gmd> (Bakwin et al., 1998; Tans and et. al., 1996; Zhao et al., 1997). High accuracy CO₂ measurements at WBI are made by a non-dispersive infrared spectroscopy CO₂ analyzer. The sample air is dried to a dewpoint of -25° by passing the air through a refrigerated, continuously purged liquid water trap, then through a Nafion drier. About every three hours the instrument is calibrated with a sequence of four standards containing 330, 360, 390, and 420 ppm CO₂.

Modeled carbon fluxes are compared to data collected at the Fermi National Accelerator Laboratory flux tower site in Illinois (FL, 41.86°N and 88.22°W) and at the Bondville site in Illinois (BV, 40°N and 88.29°W). In the summer of 2007, fluxes from soybeans were collected at the FL site. The data were obtained from FLUXNET and is available on-line at <http://www.fuxnet.ornl.gov> (Olsen and Rander, 2004; Baldocchi, 2006).

6.3 Results

6.3.1 Impacts of the Crop Phenology Model on LAI, FPAR, and NEE

Using the crop phenology model dramatically changes the LAI and FPAR for corn and soybeans (Figures 6.7 and 6.8). Comparisons of LAI predicted by the crop model to observations at Bondville from a point simulation by Lokupitiya et al. (2008) show a sample seasonal growth cycle of LAI of both corn and soybeans. Figure 6.7 illustrates that the crop phenology model captures the correct timing and magnitude of LAI for both these crops.

In this study, both the LAI and FPAR for corn and soybeans from MODIS used in the BASE case gradually increase throughout the simulation, reaching maximum values of ~ 2.5 and 0.8 , respectively (Figure 6.8). Using prescribed LAI and FPAR does not capture the growth cycle in the crops nor the specific characteristics for corn and soybean. For corn, various studies show that crops grow rapidly through June to reach maximum LAI values in mid-July of ~ 5.5 - 6.5 (Howell et al., 1996; Maddonni et al., 2006; Williams and Lindquist, 2007; Pachta, 2007). The crop phenology model, CROP, does a much better job at capturing the LAI growing cycle for corn, reaching a maximum LAI of ~ 0.7 around July 15 and then declining after reaching physiological maturity; however, CROP tends to overestimate the maximum LAI compared to mean values reported in the literature. The associated FPAR reaches a maximum just under 1.0 and remains constant until harvest, when it rapidly declines.

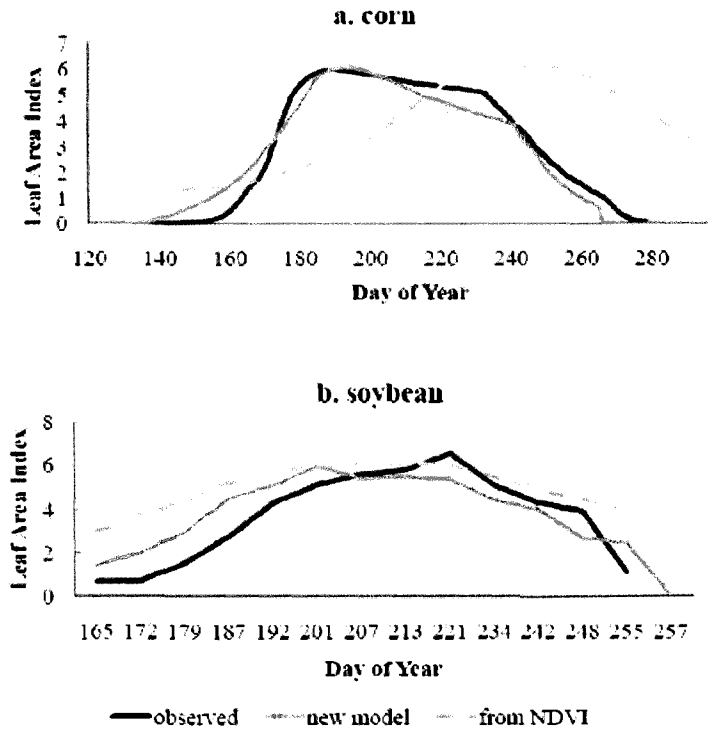


Figure 6.7: Leaf area index (LAI) of crops in rotation in Bondville. Corn in 1999 is displayed in the top panel and soybeans in 2000 are displayed in the bottom panel. The drop of LAI towards the end of the growing season represents the field drying and harvest events (from Lokupitiya et al. (2008)).

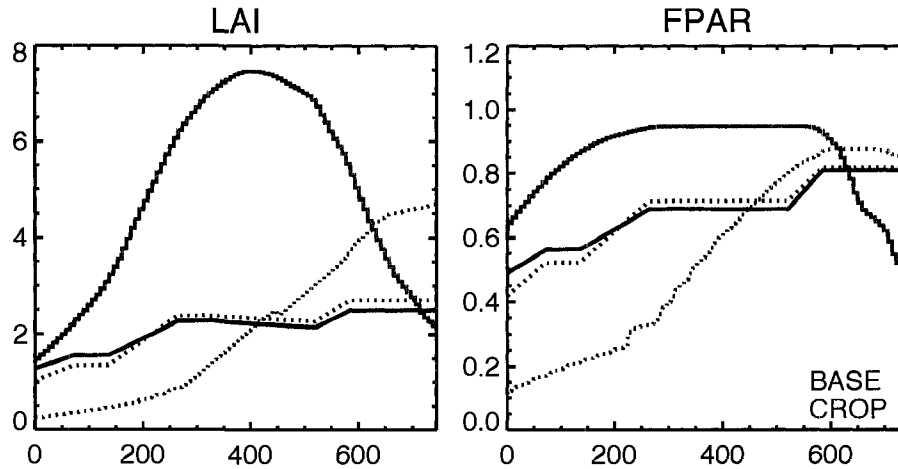


Figure 6.8: Leaf area index (LAI, left panel) and fraction of photosynthetically active radiation (FPAR, right panel) from the BASE simulation without the crop model (blue) and from the CROP simulation (red). The values plotted are the means from all of the gridcells that have corn (solid) and soybeans (dotted). In the BASE case, since these crops are not included, we plotted the mean MODIS LAI and FPAR for the corresponding gridcells.

Differing from corn, soybeans generally grow later in the summer and typically reach maximum LAI values of $\sim 5-6$ in the beginning to mid August (Malone, 2001; Jones et al., 2003; Wang et al., 2003; Cohen et al., 2003; Suyker et al., 2005). The CROP simulation captures the seasonality of soybean growth much better than the prescribed LAI from MODIS, although the maximum LAI in the model may occur slightly later than times reported. The magnitude of the maximum LAI for soybeans is reasonable, but on the low side of the typical range. The FPAR in the CROP case follows the LAI curve, increasing to ~ 0.9 in mid-August.

To provide an estimate of the annual cycle in NEE for both corn and soybeans, as well as to depict the skill of the crop phenology model, monthly mean NEE for the BV site from Lokupitiya et al. (2008) are displayed in Figure 6.9. The mean

NEE for corn and soybeans from this study is displayed in Figure 6.10. The CROP simulation dramatically changes the NEE for corn. While the BASE model has a relatively constant daytime NEE of $\sim 10 \mu\text{mol m}^{-2} \text{s}^{-1}$ that slightly increases from May to August, CROP has much greater uptake with a more realistic seasonality. According to literature, maximum daytime crop uptake during the peak growing season between mid-June and mid-August is 55-70 $\mu\text{mol m}^{-2} \text{s}^{-1}$ (Suyker et al., 2005; Verma et al., 2005; Lokupitiya et al., 2008). The CROP simulation daytime maximum NEE for corn matches reported values well and captures the timing of the increase in drawdown at the beginning of June as well as the decrease of the NEE at the end of the growing season during harvest. The day-to-day variability seen in the corn NEE is due to synoptic events and correlates well with changes in temperature and radiation.

For soybeans, the change in NEE caused by including the crop model is less significant. The BASE model again has a relatively constant daytime uptake that increases from $\sim 5 \mu\text{mol m}^{-2} \text{s}^{-1}$ in June to $\sim 10 \mu\text{mol m}^{-2} \text{s}^{-1}$ in August. Using the crop phenology model changes the timing of the increase in NEE. Rather than a gradual increase throughout the season, the CROP simulation has limited daytime drawdown until mid-July, when the soybeans begin growing rapidly. The maximum daytime uptake using the crop phenology model is $\sim 20 \mu\text{mol m}^{-2} \text{s}^{-1}$ throughout August. According to observations, the peak drawdown for soybeans is 25-35 $\mu\text{mol m}^{-2} \text{s}^{-1}$ during August and the crops do not begin actively photosynthesizing until July (Verma et al., 2005; Turner et al., 2003; Lokupitiya et al.,

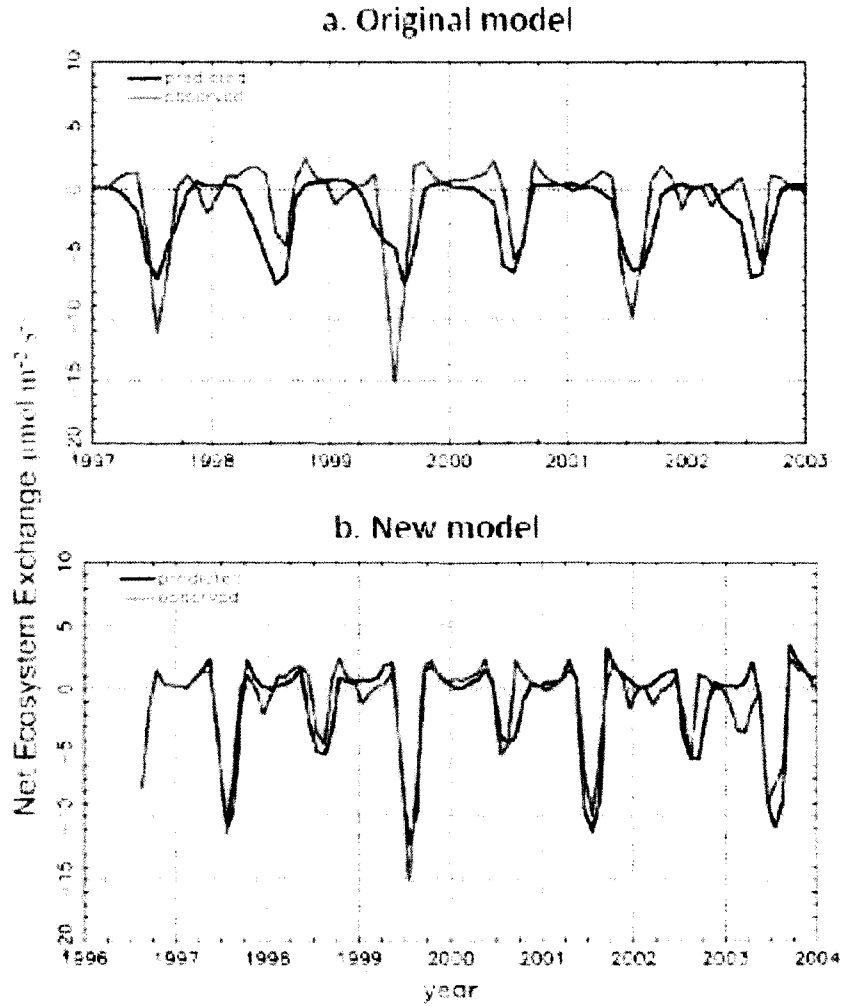


Figure 6.9: Monthly means of net ecosystem exchange (NEE) for Bondville site. Observed and predicted NEE from SiB before any modification (top), and simulation results from the new crop phenology model (bottom). Even years are soybeans and odd years are corn (from Lokupitiya et al. (2008)).

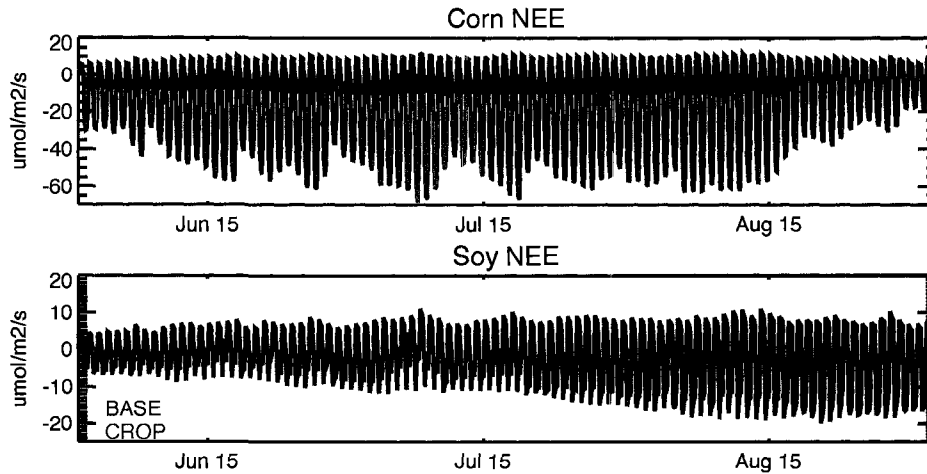


Figure 6.10: Mean NEE for corn (top) and soybeans (bottom) for both the BASE (blue) and CROP (red) simulations. Since the BASE simulation does not include corn and soybean explicitly, we calculated the mean NEE from the corresponding gridcells where the vegetation cover was C4 crops for corn and C3 grass/crop for soybean.

2008). The CROP case does a reasonable job at simulating the mean timing of the drawdown, but underestimates the magnitude of the maximum daytime uptake.

Carbon dioxide flux measurements over a soybean field for 2007 are available at one site in the MCI region (FL, see Figure 6.4 for a location of the flux tower). The CROP simulation has very good synchrony with the observations: minimal fluxes both during the day and at night until the end of June; increasing daytime uptake and nighttime respiration through July, and high daytime drawdown during August (Figure 6.11). While SiB3-RAMS captures the seasonality in NEE, it underestimates the magnitudes of the daytime fluxes, as observations show daytime maximum NEE values of $\sim -30 \mu\text{mol m}^{-2} \text{s}^{-1}$. The model also underestimates the nighttime respiration compared with the observations.

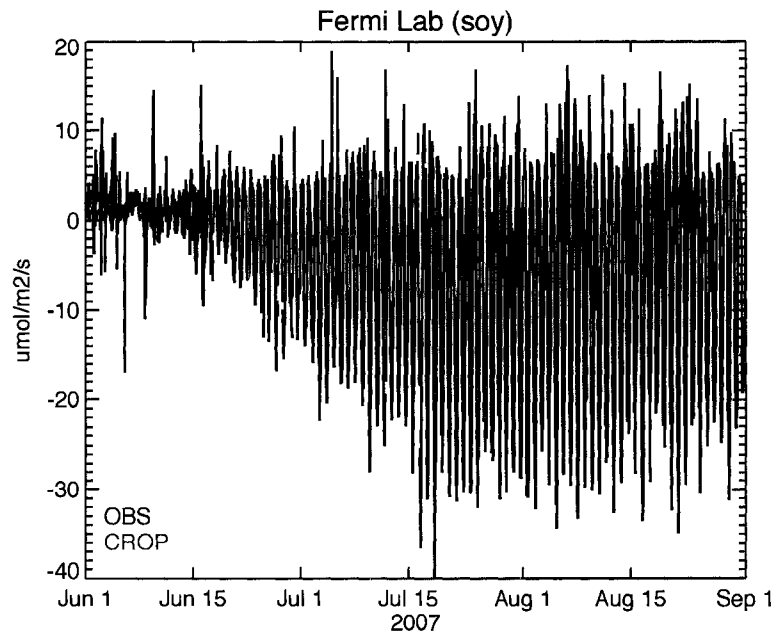


Figure 6.11: NEE observed at the Fermi National Accelerator Agricultural Site over a soybean field (black) and modeled NEE at the nearest soybean gridcell in the CROP simulation (red).

6.3.2 Distribution of the 2007 NEE

The mean growing season NEE, June through August, for both the BASE and CROP simulations, is displayed in Figure 6.12. During the summer of 2007, the entire southeastern U. S. is a source of CO₂, as is California. Photosynthesis is shut down in the model through this region due primarily to temperature stress, although daytime humidity stress also contributes. According to the National Climatic Data Center, the summer of 2007 was the 6th warmest for the U. S. in the past 113 years, with the highest temperatures in the southeast and in the west. The southeastern U. S. experienced a heat wave in August, breaking over 70 records for all-time high temperatures and for the most days above 90° F and 100° F. The 3-month Standardized Precipitation Index for June through August 2007, calculated by NOAA, shows that southeastern U. S. was exceptionally dry and southern California was moderately dry. It is very likely that the stress in the model is realistic due to the climatic conditions throughout the summer; however, the magnitude of the carbon release may be overestimated, as some areas are a mean source of more than $6 \mu\text{mol m}^{-2} \text{s}^{-1}$ during the summer.

The northern half of the United States and regions of Canada are summertime sinks of carbon. Using the crop phenology model dramatically changes the mean NEE in the MCI region. The moderate sink over the central U. S. in the BASE case becomes a significant sink, with mean NEE values of more than $-6 \mu\text{mol m}^{-2} \text{s}^{-1}$. The enhanced uptake over Iowa is due to the inclusion of corn and soybeans into

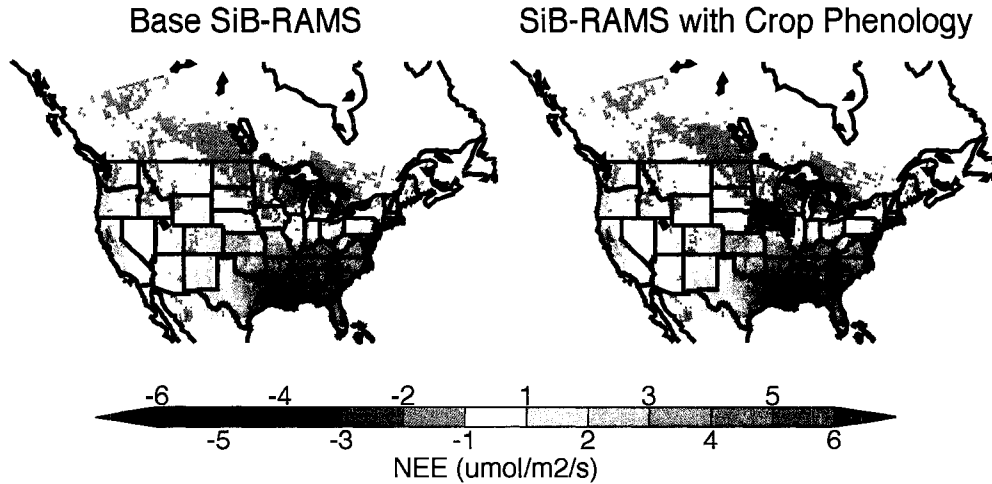


Figure 6.12: Map of the mean NEE from June through August, 2007, for both the BASE (left) and CROP (right) simulations.

the model, which have significantly more drawdown during the summer months.

Altering the NEE impacts the atmospheric CO₂ concentrations (Figure 6.13). Adding an explicit representation of corn and soybeans in the model lowers the concentrations due to the enhanced uptake. The differences between the CROP and BASE mean concentrations are more than 1 ppm in the total column over central Iowa (which corresponds to 22 ppm near the surface). The impact of the mean concentration change extends out to Canada due to atmospheric transport, although the magnitude of the difference decreases away from the MCI region due to mixing.

6.3.3 Analysis and Evaluation of Atmospheric CO₂ Concentrations

This section presents results from analyzing the CO₂ concentrations; however, we only include concentrations from June 15 rather than from June 1. The initial CO₂

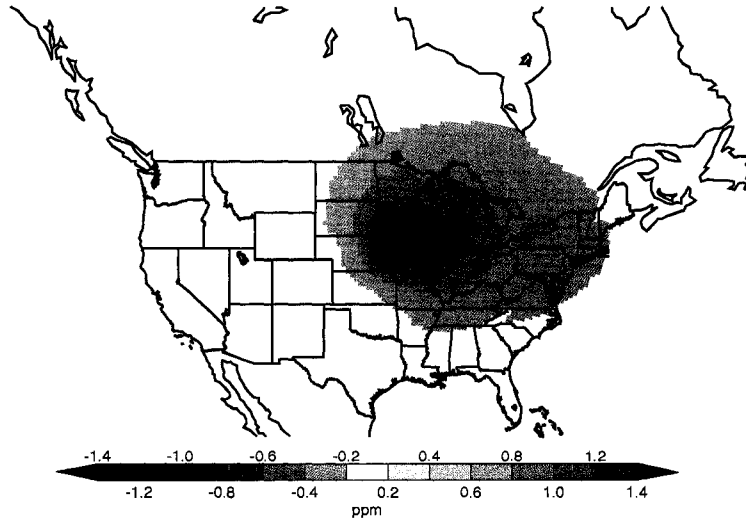


Figure 6.13: The mean June through August total column concentration difference between CROP and BASE, calculated by subtracting the mean BASE concentrations from the CROP concentrations.

concentrations on June 1 are much lower than observed, causing the concentrations in the model simulations to increase initially and creating unrealistic seasonality. To avoid including this in our analyses, we excluded the first fifteen days.

CO₂ Maps

A map of the mean June through August concentration at 120 m is displayed in Figure 6.14. The mean concentrations reflect the NEE map, with higher concentrations over the southeast where the region is a source of CO₂ and lower concentrations in the northern U. S. and Canada, where the vegetation is a summertime sink. In the eastern half of the country, the mean wind flow is southerly from the Gulf Coast and up the coastline, advecting the higher concentrations in the

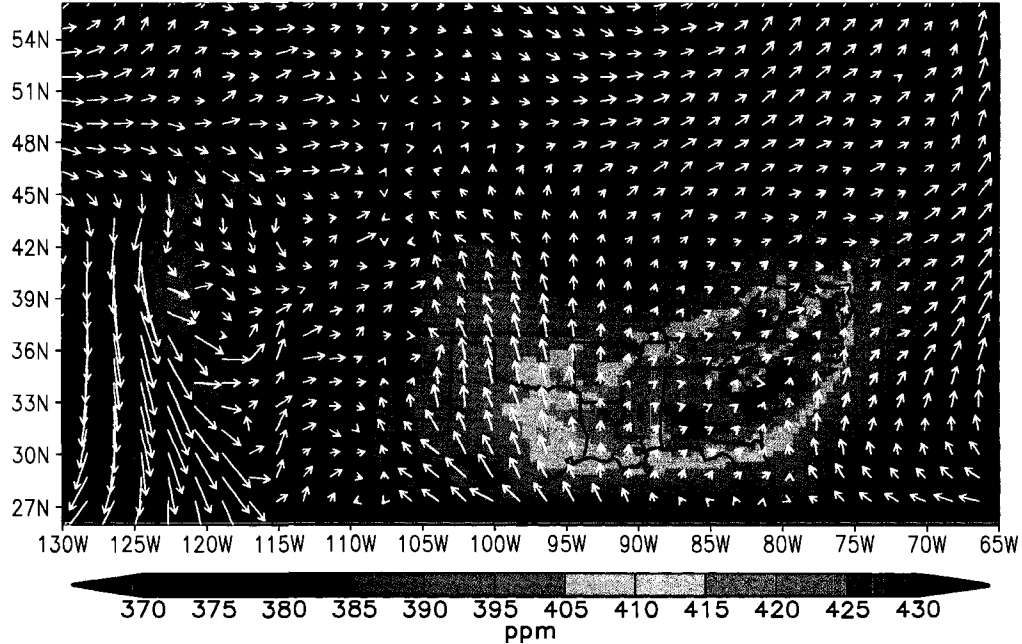


Figure 6.14: Mean CO_2 concentrations at 120 m from June through August from the CROP simulation. The mean wind vectors at 120 m are overlaid.

southeast northward. In the southern portion of the MCI region, over Nebraska, northern Missouri, and Illinois, there is a strong gradient of CO_2 where the concentrations change over 30 ppm as the land shifts from being a source to a sink. In the northern U. S. and Canada, the mean wind flow is westerly, transporting low CO_2 across the continent. On the west coast, the mean wind flow is northerly, advecting the higher concentrations from California down the coast.

Using the nested grid from the NEST simulation, we can zoom in on the mean concentrations over the MCI region (Figure 6.15). Figure 6.15 shows the strong gradient that is seen in the CROP case, with a change of over 15 ppm between the southern and northern towers in the MCI. A region of low CO_2 exists over northern Iowa, due to the strong drawdown from the crops. The southerly winds advect

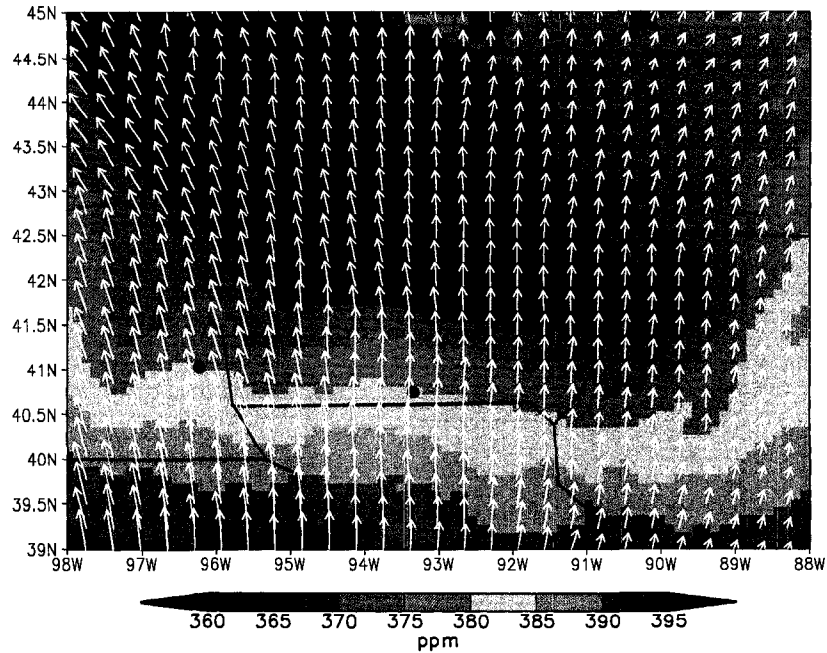


Figure 6.15: Mean CO_2 concentrations at 120 m from June through August from the interior grid in the NEST case. The mean wind vectors at 120 m are overlaid. The black dots represent the towers.

the low concentrations northward so that the center of the low CO_2 anomaly is no longer over central Iowa.

CO₂ Evaluation at the Towers

At each of the six towers in the MCI region, we calculated the root mean square errors (RMSE) between the observations and the three cases, including both the CROP case and the NEST case which both used the crop phenology model (Figure 6.16). Including the crop phenology model reduces the day and night errors at all the towers except WBI at night, where the errors are higher due to low concentrations in both CROP and NEST. Focusing on BASE versus CROP, all of the daytime errors are cut in half when the crop model is included. This substantial

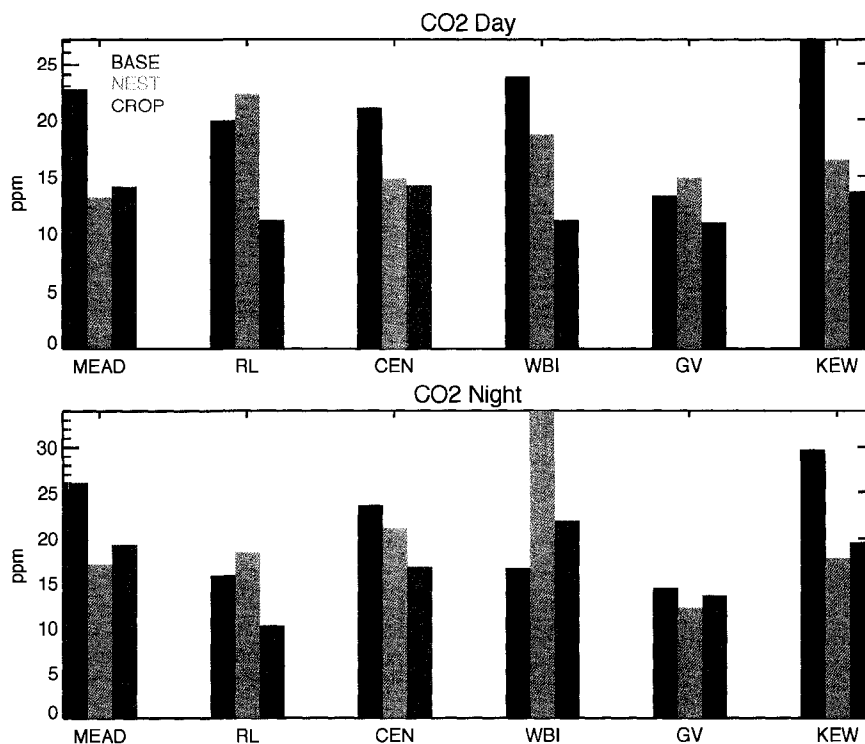


Figure 6.16: Root mean square errors (RMSE) for daytime (1800 - 0000 UT, top) and nighttime (0300 - 1200 UT, bottom) for the three cases: BASE=blue, NEST=green, and CROP=red.

reduction is due to the concentrations being too high in the BASE model, causing offsets of more than 20 ppm at some of the towers. The errors at night are also substantially reduced at all towers except WBI, which is in the center of the MCI region.

Comparing BASE with NEST, in general modeling corn and soybeans reduces the errors, especially at the three southern-most sites (MEAD, CEN, and KEW). The errors are actually larger at the two northern sites (RL and GV). These large errors in the NEST case are due to the concentrations being too low and thus offset from the observations. Since the mean wind flow is southerly, underestimating

the concentrations at the northern sites indicates that including the crop model overestimates the total uptake in the region, which would cause the concentrations to be too low as air is advected across the the strong sink.

Including the nested grid actually increases the errors from the CROP case, which only a used single grid. The increase is due to offsets between the NEST case and the observations, with the NEST concentrations being lower than observed. The change in errors between the two cases suggests we are overestimating the fraction of crops in the MCI region, as the mean uptake for both corn and soybeans remains the same for NEST as it was in CROP. We hypothesize that a detailed investigation into the crop map and fractional coverage of both corn and soybean would fix the underestimation seen in the concentrations, as aggregating the original 56 m map up to 10 km likely overestimated the areal crop coverage.

To evaluate the synoptic variability in SiB3-RAMS, we created a Taylor diagram of the daytime minimum concentrations (Figure 6.17, Taylor (2001)). Including the crop model increases the correlations at all towers and for both cases. Calculating fluxes specific for corn and soybeans improves the model and increases the skill of the model by more accurately capturing both the synoptic variability and the seasonal trend. Using the nested grid increases the standard deviations, as the day-to-day changes in concentrations are overestimated due to the overestimation in the areal coverage of the large sink. The CROP case decreases the normalized standard deviation at half of the sites (RL, CEN, and GV) and increases the standard deviations at MEAD and KEW.

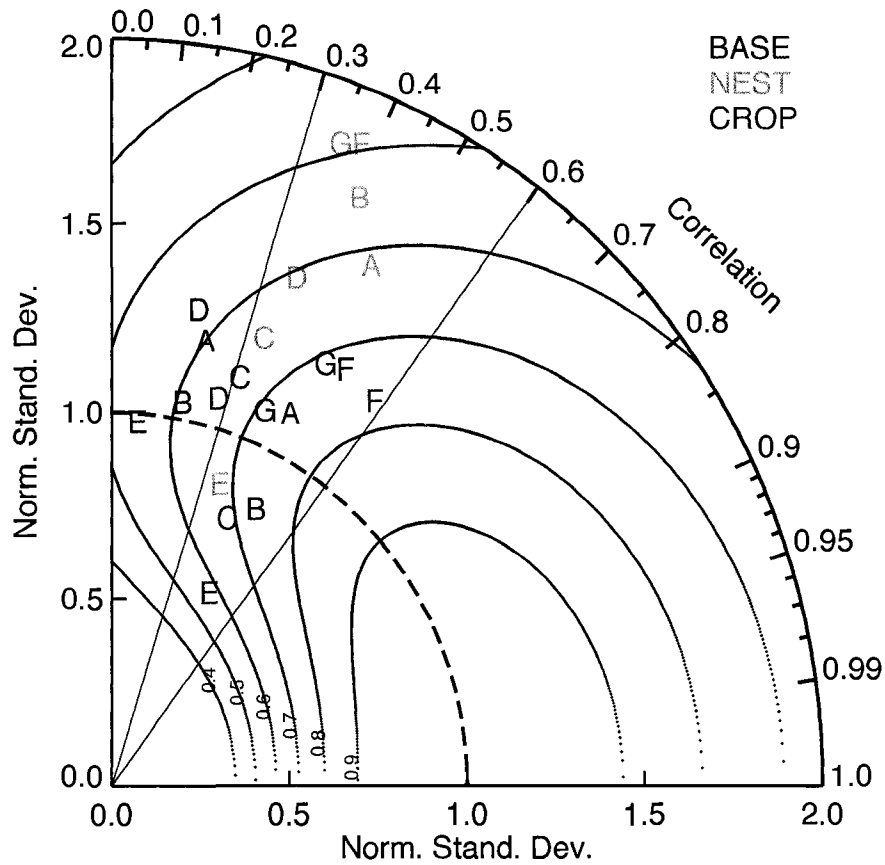


Figure 6.17: Taylor diagram of the daytime minimum concentrations for the BASE (blue), NEST (green), and CROP (red) cases. Daytime minima are used to remove the diurnal cycle of CO_2 to investigate the model's ability to capture the synoptic variability. The contours indicate a fitness score based on a combination of the normalized standard deviation and the correlation (Taylor, 2001). The towers are labeled A-F as in Table 6.1. The gradient between the towers is also calculated for the both observations and the simulations, and is represented by G. The gradient is the highest daytime minimum concentration across all towers minus the lowest daytime minimum concentration on the same day.

The gradient between the towers is relatively highly correlated for all three cases, indicating that even the BASE model does a reasonable job at capturing the changes in the gradient across the tower network, despite the concentrations being too high at all towers. Including the crop phenology model increases the standard deviation of the gradient, hence the model overestimates the day-to-day variability in the gradient.

Further Analysis of the CO₂ Gradient over the MCI Region

The lowest concentrations both observed and modeled are at RL and WBI, and the CROP case matches the magnitudes of these concentrations relatively well, capturing concentrations less than 340 ppm seen in the observations (Figure 6.18). Without including the crop phenology model, SiB3-RAMS cannot recreate these low concentrations and the modeled CO₂ is shifted upwards by nearly 20 ppm. In general, the highest observed and modeled concentrations are at the two southernmost sites, MEAD and CEN, although towards the end of August the observations have the highest concentrations at WBI and GV. The model does capture the increase at these towers; however, it underestimates the magnitude of the change.

Figure 6.18 also shows the seasonal cycle in the CROP case differs slightly from the observations. While both the model and the observations have decreasing concentrations through June, the model overestimates the decrease and has minimum concentrations in mid-July while the concentrations in the model are still decreas-

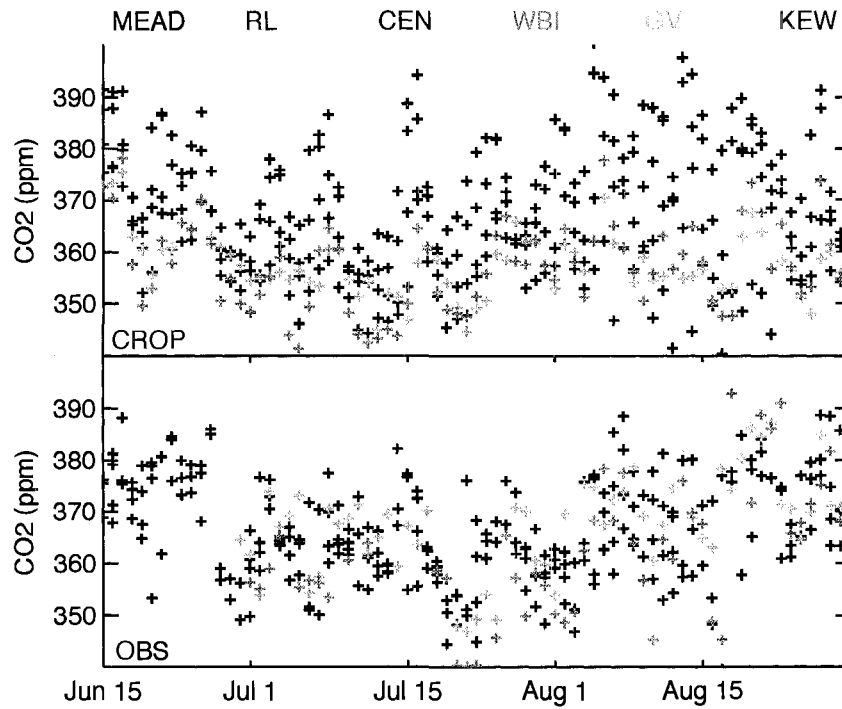


Figure 6.18: Daytime minima at all the towers for the CROP simulation (top) and the observations (bottom). Each tower is a different color: MEAD=black, RL=purple, CEN=blue, WBI=green, GV=yellow, and KW=red.

ing and do not reach their minimum values until the end of July. SiB3-RAMS also underestimates the concentrations at RL and GV during mid-August.

Overall, SiB3-RAMS does a reasonable job at capturing the magnitude of the gradient between the towers (Figure 6.19). The gradient increases with the growing season until mid-August, when the differences between the towers begin to shrink. The mean gradient in late June is ~ 15 ppm in the observations, increases to ~ 30 ppm in mid-August, and decreases to ~ 18 ppm by the end of August. The model captures the overall shape; however, SiB3-RAMS overestimates the gradient both at the beginning of the simulation and during mid-August, which indicates the magnitude of the sink in Iowa is too strong in the model, causing the model to overamplify the large increases in the gradient. The CROP simulation captures the day-to-day variability in the gradient quite well, which was also indicated by the high correlation values seen in Figure 6.17.

Changes in the magnitude of the gradient are due to synoptic weather patterns shifting the location of the large-scale gradient seen between the low concentrations in the north and the high concentrations in the southeast. On 16 July the gradient across the towers is the largest seen during the summer, with a change of over 40 ppm across the region. The CO₂ map for 16 July shows that the large-scale gradient occurs over northern Missouri, crosses the southwestern corner of Iowa, and continues up across South Dakota (Figure 6.20). The mean wind flow over the central U. S. is from the south, helping to advect the high concentrations from the south further north. Zooming in to the MCI region shows that the large-scale

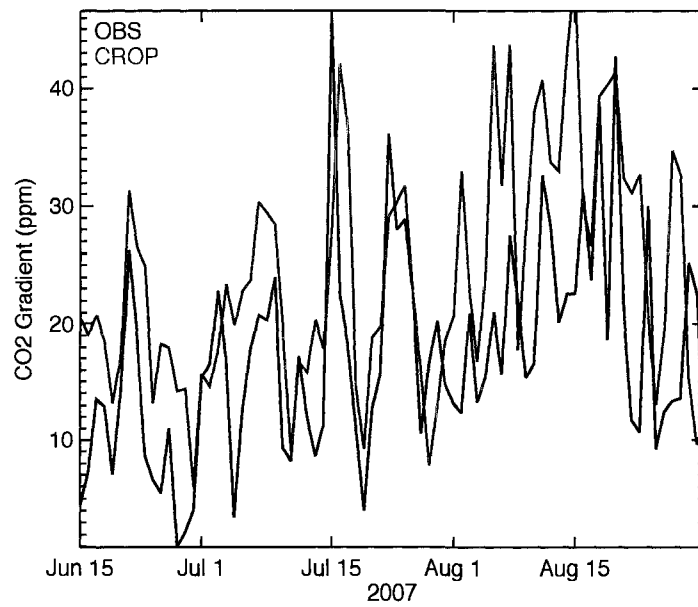


Figure 6.19: The measured gradient between the towers (black) and the simulated gradient in the CROP case (red). The gradient is the difference between the lowest and highest daytime minimum values across the towers.

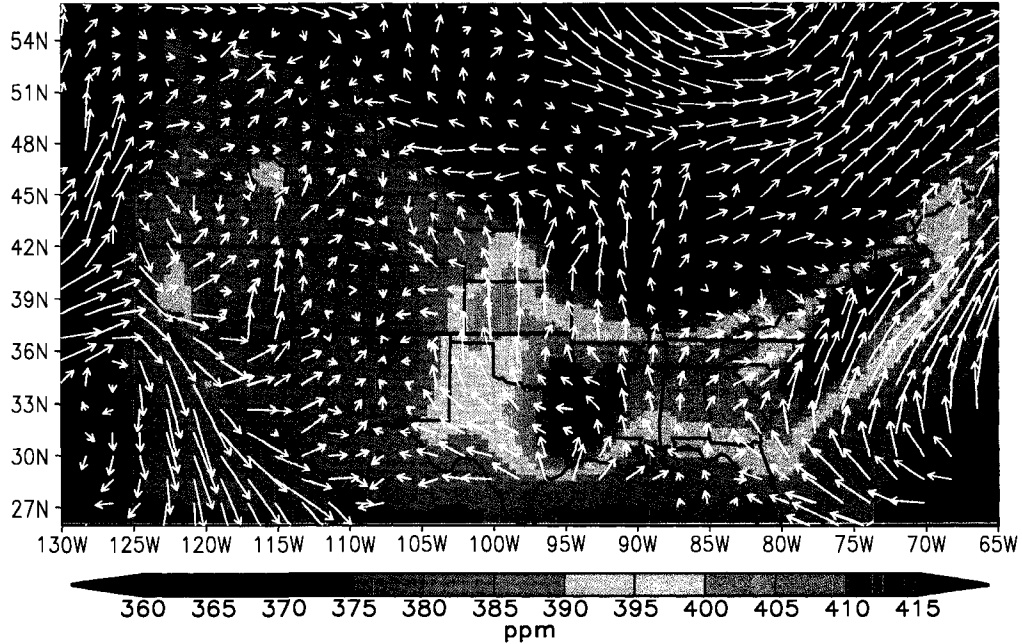


Figure 6.20: Mean daytime (1800 - 0000 UT) concentrations on 16 July, 2007 at 120 m for the CROP case with the mean wind vectors overlaid.

gradient runs through the center of the towers, causing the southernmost towers, MEAD and CEN, to have concentrations over 30 ppm higher than the rest of the towers (Figure 6.21), although it should be noted that the NEST simulation does overestimate the magnitude of the gradient.

Three days later, on 19 July, the CO_2 differences between the six towers is less than 10 ppm. Low CO_2 concentrations extend across nearly the entire MCI region, and the mean wind is northerly (Figure 6.22). The large-scale gradient now occurs over further southwest, over northern Kansas and up through Nebraska. Focusing on the MCI region, the lowest concentrations are centered over central Iowa. The large-scale gradient in CO_2 is shifted further southwest and no longer impacts any of the towers due to the northerly wind flow (Figure 6.23).

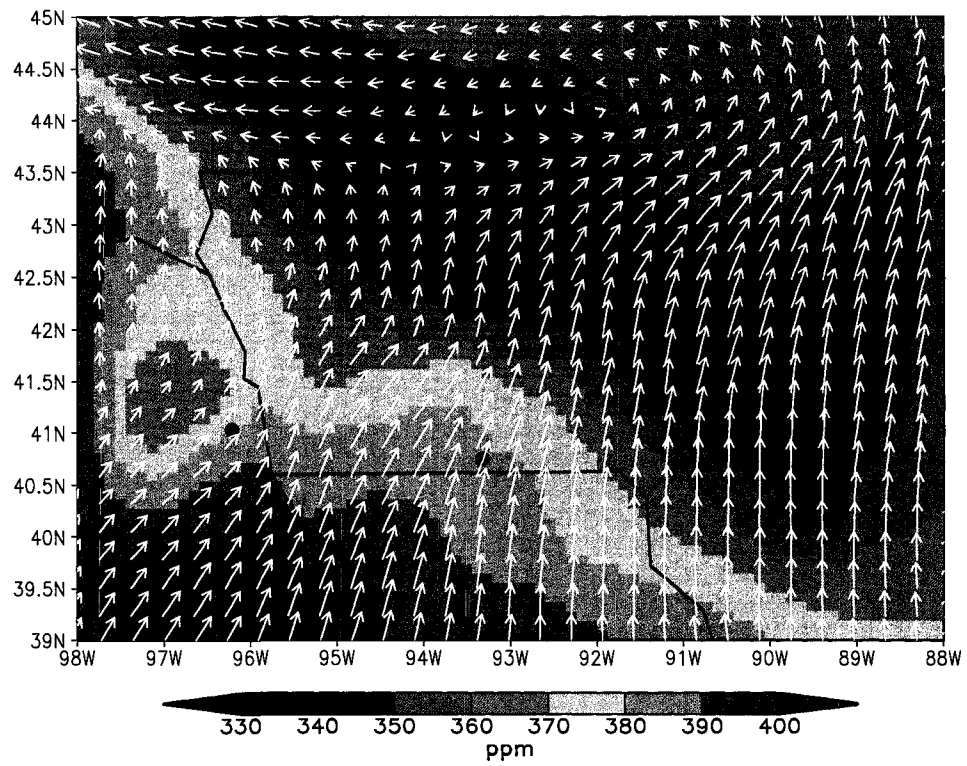


Figure 6.21: Mean daytime concentrations on 16 July at 120 m over the MCI region in interior grid of the NEST case.

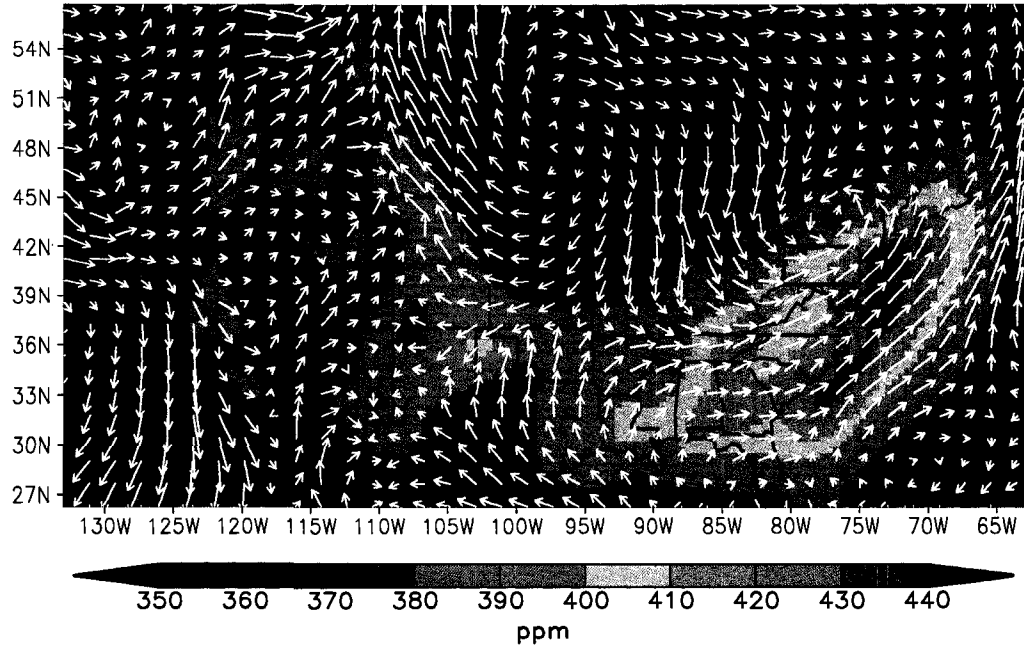


Figure 6.22: Mean daytime concentrations on 19 July at 120 m for the CROP case.

Although the concentrations are only displayed for these two cases, we investigated other days and found the results to be similar. High gradients occur when the mean wind is southerly, causing high concentrations from the south to be advected northward. This synoptic weather pattern causes the large-scale gradient to shift over the MCI region and causes large differences in the concentrations between the towers. On days when the gradient between the towers is low, the wind is from the north, advecting the low CO_2 from the crops over Iowa further south so that all the towers have lower concentrations.

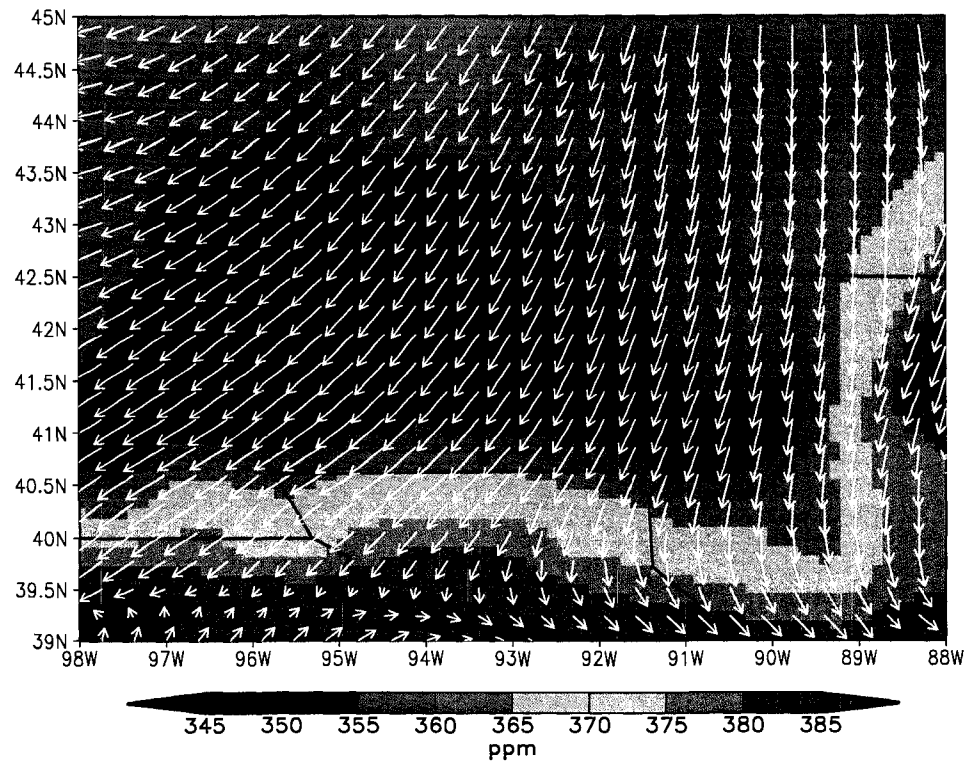


Figure 6.23: Mean daytime concentrations on 19 July at 120 m for the interior grid of the NEST simulation.

6.4 Conclusions

In 2007, the North American Carbon Program (NACP) launched a Mid-Continent Intensive Campaign (MCI) centered over Iowa to investigate CO₂ sources, sinks, and concentrations, measuring high calibrated CO₂ concentrations at six towers across the region. In this study, we analyzed CO₂ fluxes and concentrations for that summer using the coupled ecosystem-atmosphere model SiB3-RAMS. To improve the CO₂ fluxes over the mid-continent region, we coupled a crop phenology model to SiB3-RAMS, which replaced the MODIS LAI/FPAR with predicted values. Simulating both corn and soybeans explicitly with the crop model made the fluxes for these two crops more realistic compared with the observations and dramatically altered the fluxes over the central mid-continent region, increasing the mean uptake to more than 6 $\mu\text{mol m}^{-2} \text{s}^{-1}$. The changes caused the mean total column CO₂ concentration to decrease by over 1 ppm over the region, and the concentrations near the surface decreased by more than 20 ppm.

During the summer, the southeast U. S. experienced both a heat wave and a drought. The climatic conditions stressed the plants, significantly reduced the photosynthesis while increasing the respiration, and resulted in the southeastern region of the country being a large summer source of CO₂. Humidity and temperature stress in California, also due to hot and dry conditions, caused this state to be a source of CO₂ as well. The northern half of the continent was a moderate summertime sink for CO₂.

The mean summer distribution of CO₂ matched the NEE map, with high concentrations in the southeast and low concentrations in the north. The high southern concentrations created a large-scale gradient over the mid-continent, with differences of over 4 ppm in the total column and over 40 ppm at 120 m. Shifting of this large-scale gradient impacted the concentrations at the towers. When the mean flow was southerly, the gradient crossed through the MCI region and created differences of over 30 ppm between the towers; however, when the wind was northerly the large-scale gradient shifted to the southwest and smaller differences were seen.

Comparing the modeled CO₂ concentrations with tower data collected during the MCI Campaign, the CO₂ concentrations over the MCI region dramatically improved when the crop model was included, reducing the RMSE at all all towers by nearly half. Including the crop phenology model also improved the synoptic variability in CO₂ concentrations as well as the gradient seen across the towers. Concentrations lower than 340 ppm were seen during July and August in both the model and in the observations. This study showed that corn and soybeans are highly productive crops that significantly impact both CO₂ fluxes and concentrations, and to model the mid-continental region accurately both these crops must be included.

Acknowledgements

Thank you to Erandi Lokipitiya for developing the crop phenology model and to Ian Baker for helping implement it into SiB3-RAMS. We thank Natasha Miles, Ken Davis, and Scott Richardson from Penn State University and Keith Paustian from Colorado State University for the MCI CO₂ data, Arlyn Andrews at NOAA-ESRL for the concentrations at WBI, and Roser Matamala from Argonne National Laboratory for the CO₂ fluxes at the Fermi National Accelerator Laboratory Agricultural Site. We thank Matt Hanson from South Dakota State University for the crop map. This research was funded by the National Aeronautics and Space Administration (NASA) contracts NNX06AC75G and NNG05GF41G and by the Department of Energy contract DE-FG02-06ER64317.

7 A Preliminary Analysis on the Effects of Fossil Fuel Emissions on Regional Atmospheric CO₂ Concentrations

Abstract

To improve fossil fuel emissions estimates, Gurney et al. (2008) created a high spatial and temporal resolution inventory, Vulcan. Since the Vulcan database will be used in a variety of applications, it is important to investigate the effects of changes in the spatial and temporal distribution of fossil fuel emissions on atmospheric CO₂ concentrations. Using the coupled ecosystem-atmosphere model SiB3-RAMS, this study compared CO₂ concentrations from the previous coarse emissions (Andres et al., 1996) to concentrations using the Vulcan inventory. Changes in the spatial distribution caused differences of over 10 ppm near the surface, with the largest changes in California and in the eastern half of the United States. Including seasonality in the emissions also altered regional CO₂ concentrations, with the largest differences occurring over the southeast, where higher concentrations occurred during the summer and lower concentrations occurred during the remainder

of the year. The magnitude of the seasonal changes was more than 20 ppm at some locations. This study demonstrated that using coarse spatial distributions and unaccounting for temporal variability created biases in the concentrations and thus may cause significant errors in source and sink estimates from atmospheric inversions.

7.1 Introduction

Even though the atmospheric CO₂ concentration is increasing rapidly, only about half of the CO₂ emitted by human activities is accumulating in the atmosphere. The portion of the emitted CO₂ not present in the atmosphere is absorbed by sink processes on land or in the ocean: the CO₂ is either taken up by terrestrial ecosystems due to an excess of primary production (photosynthesis) over decomposition or is dissolved in sea water and mixed into the deep ocean. Using atmospheric tracer transport models, inverse modelers can quantitatively estimate the strengths and spatial distribution of carbon sources and sinks around the world from CO₂ concentration data; however, in order to make these estimates, the fossil fuel CO₂ emissions must be accurately estimated and removed so that the biospheric and oceanic fluxes can be isolated and quantified.

Compared with other aspects of the carbon cycle, fossil fuel CO₂ emissions have been considered to be relatively well understood, as nation-level CO₂ emissions for the industrialized world have been quantified at annual and sometimes monthly timescales (Marland and Rotty, 1984; Blasing et al., 2005; Gurney et al., 2007). To

downscale CO₂ emissions from fossil fuel burning to spatial scales smaller than the national level, the emissions were allocated to a 1° x 1° map using political units and population density (Andres et al., 1996). Although these emissions estimates are adequate for studies that use sub-continental spatial scales and annual mean temporal scales, as studies reduce both the spatial and temporal resolutions of interest the emissions estimates have several shortcomings: the emissions lack seasonal and diurnal variation, the estimates have a coarse spatial resolution, and the estimates use population density to subdivide the national estimates while the combustion often does not scale with population. In a sensitivity study of atmospheric inversions by Gurney et al. (2005), not including the seasonality in fossil fuel emissions produced biases of up to 50% of seasonal flux estimates at the height of the growing season in regions where fossil fuel emissions are large.

To improve fossil fuel emissions estimates, Gurney et al. (2008) produced a high-resolution inventory, Vulcan, of anthropogenic emissions with ~ 10 km grid increments and hourly timesteps over the United States. By incorporating CO₂ emissions factors into a process-based, data-driven air-quality emissions model, Gurney et al. (2008) generated a comprehensive database that combined inventory data, process attributes, and classification information. The Vulcan inventory utilizes three classifications of input: point sources (i.e. power plants), mobile sources (i.e. vehicle emissions), and area sources (i.e. residential sources). This high-resolution fossil CO₂ inventory will be used in a variety of scientific applications to enhance our understanding of the carbon cycle.

The new Vulcan inventory will replace the previous coarse, population based fossil fuel estimates in both forward and inverse modeling studies. Since the emissions will alter the atmospheric CO₂ concentrations, as well as the sources and sinks predicted by these models, it is important to understand the effects of both the spatial distribution and the seasonality of fossil fuel emissions on the atmospheric CO₂ concentrations. This study investigates the impact of the Vulcan emissions on CO₂ concentrations using a coupled ecosystem-atmosphere model, SiB3-RAMS.

7.2 Methods

7.2.1 Model Description, Initialization, and Input Data

The model used in this study is the Simple Biosphere Model Version 3 (SiB3) coupled to the Brazilian version of the Colorado State Regional Atmospheric Modeling System (RAMS). The model is described in Chapter 5. The meteorological fields; soil map; vegetation coverage; leaf area index (LAI) and fraction of absorbed photosynthetically active radiation (FPAR); fire emissions; air-sea fluxes; initial respirable carbon, soil moisture and SiB3 prognostic variables; CO₂ initial and lateral boundary concentrations; CO initial and lateral boundary concentrations; and OH concentrations are all described in Chapter 5. This study used the vegetation cover that included both C3 and C4 vegetation and three patches per grid cell to capture sub-grid land cover heterogeneity.

To investigate the impact of spatial and seasonal redistribution in fossil fuel emissions estimates on atmospheric CO₂ concentrations, this study utilized two different inventories of fossil fuel emissions. Both of the annual anthropogenic source estimates were matched to the total estimated emissions from the Energy Information Administration (EIA, 2007). The first inventory used is the Andres et al. (1996) 1° x 1° distribution of CO₂ emissions from fossil fuel consumption and cement manufacture (Figure 7.1, left panel). This inventory covers all of North America, including emissions over Canada and Mexico. Anthropogenic CO₂ was emitted constantly in each grid cell of the SiB3-RAMS simulation domain at each timestep.

The second inventory used is the Vulcan high-resolution dataset by Gurney et al. (2008) (Figure 7.1, right panel). The Vulcan emissions have ~ 10 km horizontal resolution, which was aggregated up to the grid cell increment used in SiB3-RAMS. The emissions estimates change every hour and include the seasonal and diurnal cycles of fossil fuel emissions. The Vulcan database only includes emissions over the United States.

7.2.2 Case Descriptions

In this study, we performed two simulations over North America with SiB3-RAMS. Both simulations ran for an entire year, from 0000 UT 1 January 2004 to 0000 UT 20 December 2004. The simulations had 150 x 90 gridcells with 40 km horizontal grid increments and 46 vertical levels up to 24 km (see Figure 5.3 for the domain

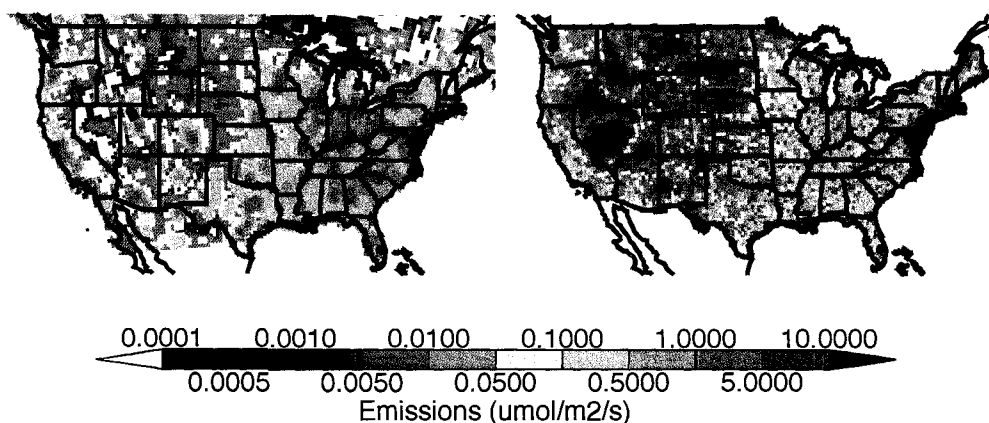


Figure 7.1: Fossil fuel fluxes from the Andres et al. (1996) distribution (left panel) and the Vulcan inventory by Gurney et al. (2008) (right panel). The Andres et al. (1996) flux was calculated from the annual emissions estimates and is emitted every timestep in the model. The flux from Vulcan shown is the annual mean emissions for comparison. In the model the Vulcan emissions change hourly.

region and landcover classification). The first case, which we will refer to as FF95, used the fossil fuel emissions estimates by Andres et al. (1996). The second case, HRFF, used the Vulcan inventory by Gurney et al. (2008).

7.2.3 Observations

This study utilized continuous observations of CO_2 concentrations measured at tower sites across the United States (see Figure 5.4 for a location of the towers and Chapter 5 for a complete description of the data). Table 7.1 lists the towers that were analyzed in this study. The Canadian towers were not included since the Vulcan estimates only cover the U. S. The Ring of Towers over the central U. S. (BRU, RED, FEN, and WBG) only measured CO_2 concentrations from May

Ref.	Site	Lat (N)	Lon (W)	Ref.	Site	Lat	Lon
A	WKT	31.32	97.33	G	WBG	44.82	89.06
B	SGP	36.62	97.5	H	SYL	46.25	89.35
C	LEF	45.92	90.2	I	HRV	42.54	72.17
D	BRU	46.47	91.57	J	AMT	45.03	68.68
E	RED	46.83	90.84	K	HOW	45.2	68.74
F	FEN	45.74	88.43				

Table 7.1: List of the towers that collected 2004 CO₂ concentrations and that were used in this study.

through August. Measured concentrations were compared to the closest model level available, and measurements at the highest elevation were used if the concentrations were collected at various levels.

7.3 Results

7.3.1 Evaluation of Atmospheric CO₂ Concentrations

To evaluate the impact of different fossil fuel emissions on atmospheric CO₂ concentrations, we compared modeled concentrations to tower measurements. To evaluate any seasonal impacts of the fossil fuel emissions, we separated the year-long simulations into three time periods: January through April (JFMA), May through August (MJJA), and September through December (SOND). For each of these three time periods we calculated the root mean square errors (RMSE) between the model and the measurements (Figure 7.2).

Using the Vulcan high-resolution inventory has very little impact at all the towers and over all three time periods. Changes between the FF95 case and the HRFF case are usually less than 1 ppm, and the mean change across all the

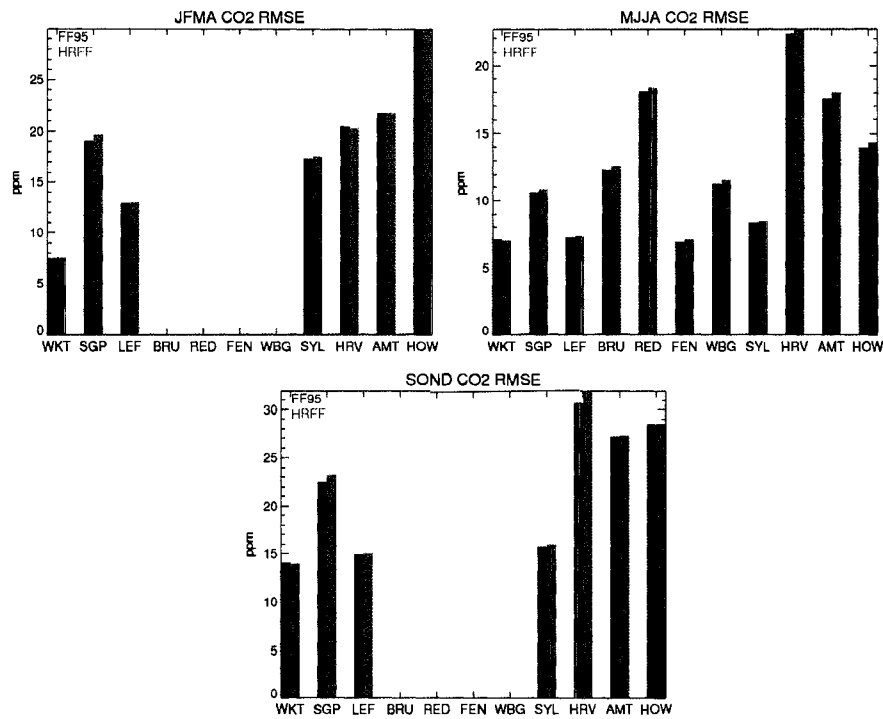


Figure 7.2: Root mean square errors at each of the tower sites for January through April (top left), May through August (top right), and September through December (bottom center). The blue bars show the results from the FF95 case and the red bars show the results from the HRFF case.

towers was < 0.2 ppm for all three time-periods. The errors are reduced at the towers in the northeastern U. S. during the beginning of the year; however, the errors are increased for the remainder of the year due to the concentrations being shifted slightly higher in the HRFF case. Although the concentrations did improve at WKT throughout the year and in the northeast during the winter and early spring, in general using the Vulcan database minimally increased the RMSE.

To investigate the impact of high resolution emissions on the synoptic variability of CO₂ concentrations, we created Taylor diagrams for both cases and for all three time periods (Figure 7.3, Taylor (2001)). Similar to the results from the RMSE evaluation, using the Vulcan inventory only has a minimal impact on the concentrations at the towers. During the growing season when SiB3-RAMS has the most skill (MJJA), the HRFF case has slightly higher standard deviations at five of the towers, indicating the magnitude of the day-to-day variability increased slightly; and in MJJA the correlation at WKT in Texas marginally improved. In JFMA, the differences between the FF95 and HRFF cases are negligible except at SGP, where using the Vulcan inventory further increased the already overestimated variability. Using the Vulcan emissions has the greatest impact on the modeled CO₂ concentrations during fall and winter. The model skill is slightly higher in the HRFF case, and this marginal improvement is caused by a reduction in the standard deviations and slightly increased correlations at half of the towers.

The small magnitude of changes at the towers can likely be primarily attributed to their locations, as all of these towers are located in relatively remote regions

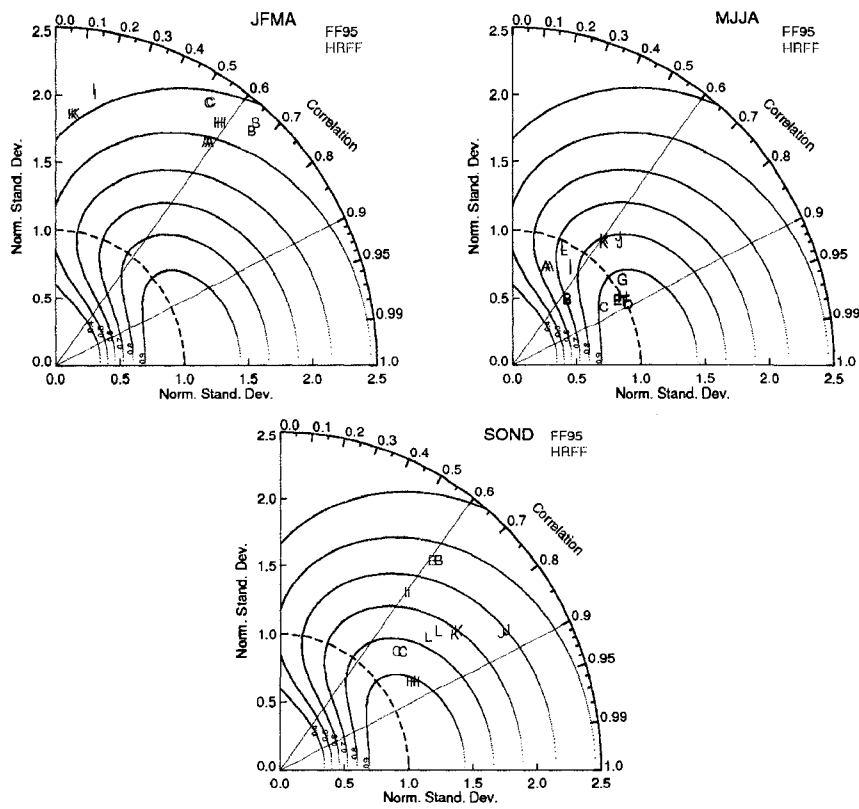


Figure 7.3: Taylor diagrams of the daytime minimum concentrations for the FF95 (blue) and HRFF (red) cases. The towers are labeled A-K as in Table 7.1. The missing towers during both JFMA and SOND are due to missing data.

heavily impacted by biology but not by fossil fuel emissions. The Vulcan inventory will likely have a more significant impact in regions more dominantly affected by anthropogenic emissions, and should be evaluated more thoroughly at towers located closer to metropolitan areas.

As a side-note, the poor performance of the model during the winter months is due to large offsets between the model and the observations. The concentrations in the model are too high and the respiration from the biology is too strong. In addition to causing large offsets, the incorrect biological fluxes over-amplify the synoptic-scale variability.

7.3.2 Annual Mean CO₂ Distribution

The annual mean CO₂ contribution from fossil fuel emissions for the HRFF case is displayed in Figure 7.4. Fossil fuel emissions significantly contribute to CO₂ concentrations over the eastern half of the U. S. and over California. Atmospheric CO₂ concentrations are increased by more than 6 ppm over the entire eastern half of the country, with concentrations of over 20 ppm seen due to the combustion of fossil fuels. The highest concentrations from anthropogenic emissions occur over large cities, such as San Francisco, Los Angeles (LA), Chicago, and New York City. A line of high fossil fuel CO₂ can be seen over northern Kentucky and West Virginia due to point sources. Higher CO₂ concentrations due to fossil fuel emissions are advected northward from the Gulf of Mexico and accumulate as they travel northeastward off the continent. Strong wind currents also occur along the

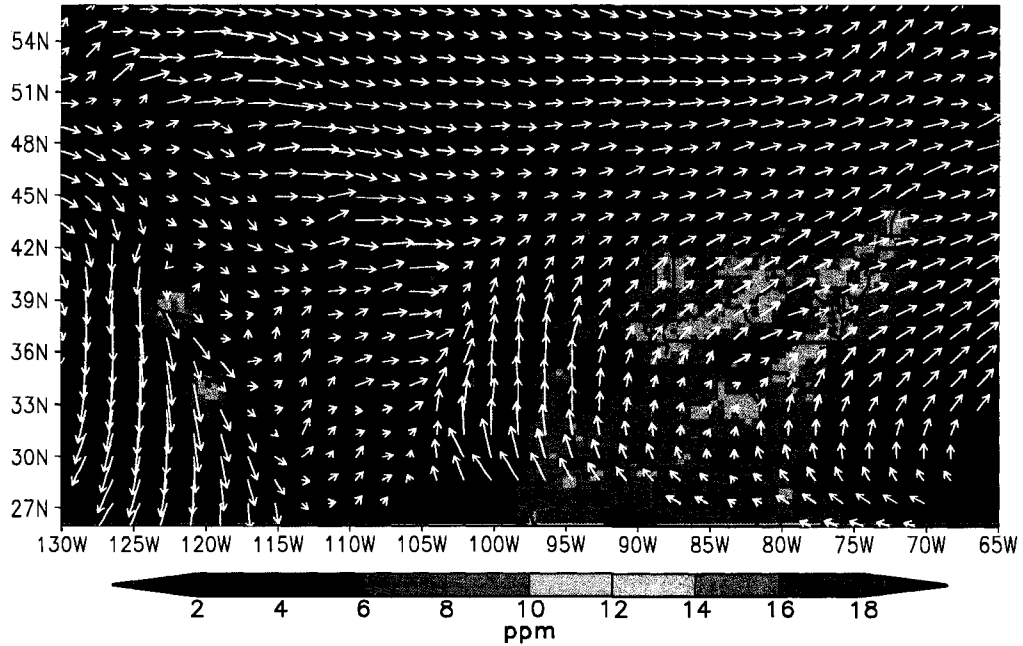


Figure 7.4: Annual mean 30 m CO₂ concentrations due only to fossil fuel emissions for the HRFF case. Annual mean wind vectors at 396 m are overlaid.

Pacific coast, where emissions from LA are advected southeastward into the Pacific Ocean.

The fossil fuel contribution to atmospheric CO₂ concentrations over the central and western U. S. is low, and on average less than 4 ppm of the total atmospheric CO₂ concentrations over this region comes from fossil fuel emissions. Throughout the northern portion of the U. S. and Canada the wind is primarily zonal, and the influence of fossil fuel emissions over these regions thus remains low as atmospheric CO₂ concentrations are advected across the country.

7.3.3 Impacts of Spatial Redistribution

To isolate the impact of altering the spatial distribution of fossil fuel emissions, we investigated differences in the annual mean. To highlight the differences in the spatial distribution between the Andres et al. (1996) and Gurney et al. (2008) emissions estimates, Figure 7.5 shows the differences in the annual mean fluxes. Distributing the fossil fuel emissions using data and a process-based model rather than using population density redistributes the emissions. In general, the emissions are reduced over broad areas in the Vulcan inventory. To compensate for this reduction, individual grid cells have much higher emissions. The individual pixels that have high emissions correspond to power plants or industries that are high polluters. In the central U. S., changes can also be seen due to traffic patterns: higher emissions through central Kansas and Nebraska correspond to the major interstates that run through these states. In the northeast, higher emissions are found in the northern-most states, while the emissions are reduced over New York state and northern Pennsylvania. The increase over Massachusetts is likely the cause of the slightly higher concentrations seen at the tower locations in this region.

The annual mean change in CO₂ concentration at 30 m is displayed in Figure 7.6. The changes in annual mean concentration reflect the redistribution of the fossil fuel emissions, with changes up to ~ 6 ppm near the surface in some locations. The most significant changes occur in California, where the region surrounding San Francisco has higher concentrations while the regions downwind of LA have con-

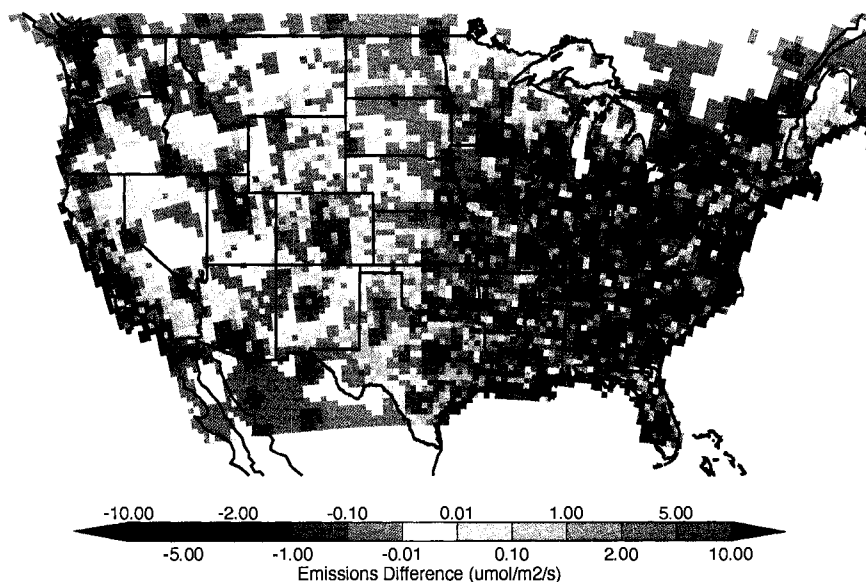


Figure 7.5: Difference between the annual mean fossil fuel emissions estimates by Andres et al. (1996) and Gurney et al. (2008), calculated by subtracting the Andres et al. (1996) emissions from the annual mean flux in the Vulcan inventory.

siderably lower concentrations, with differences over 6 ppm. The lower emissions near the coastline of LA are being advected to the southwest by the strong wind currents down the coast. To the north of California, lower concentrations occur in the HRFF case over Oregon and Washington, despite the higher emissions seen in the central regions of both states. One potential cause for the reduced near-surface concentrations may be the timing of the emissions combined with vertical mixing. Lower concentrations in the HRFF case also occur over Colorado and New Mexico, while higher concentrations are seen over eastern Montana and North Dakota.

Changes in the atmospheric CO_2 concentration due to spatial redistribution are more frequent in Texas and throughout the eastern U. S. In eastern Texas, a

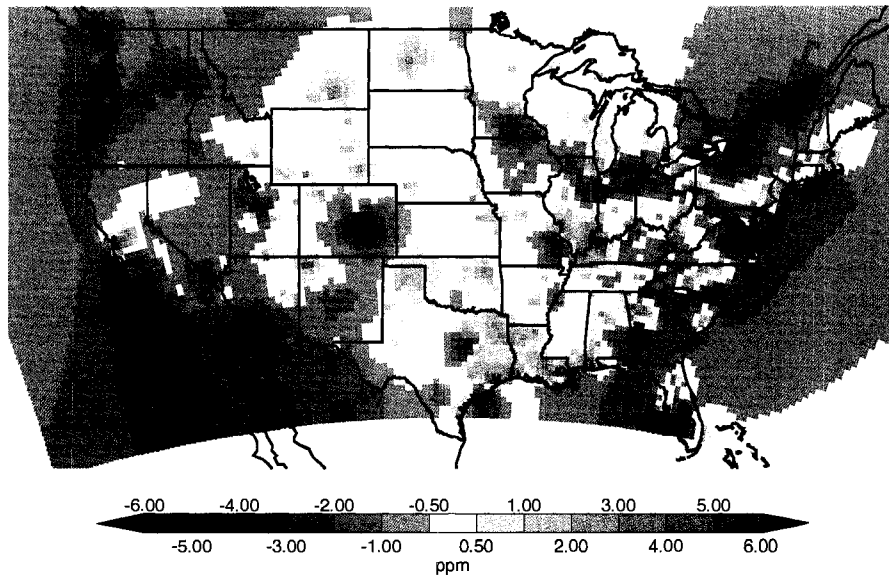


Figure 7.6: Annual mean CO₂ concentration differences at 30 m between the FF95 and HRFF cases (HRFF - FF95).

gradient of over 10 ppm in the annual mean occurs due to lower concentrations between Dallas and Austin and higher concentrations along the Louisiana border. The high concentrations are caused by several high polluting gridcells rather than by high emissions throughout the entire region. Several other dipoles of higher and lower concentrations can be seen throughout the eastern U. S.

7.3.4 Impacts of Temporal Redistribution

Monthly total fossil fuel emissions over the U. S. in the Vulcan inventory are displayed in Figure 7.7. The total emissions have a seasonal cycle, with maximum emissions in July and August and lower emissions during the spring and fall. A

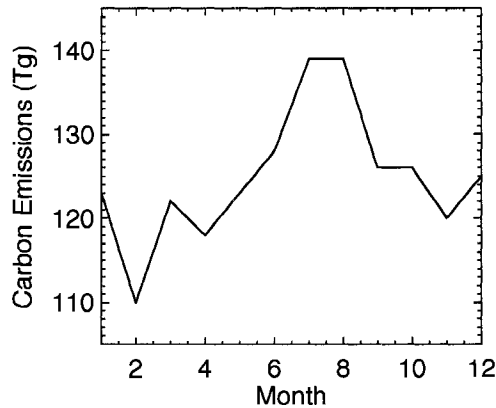


Figure 7.7: Monthly total fossil fuel emissions over the United States from the Vulcan inventory.

small secondary maximum occurs in January. This seasonal cycle differs from the mean seasonal cycles for 1981-1985 and for 1998-2002 reported in Blasing et al. (2005). In Blasing et al. (2005), maximum emissions occurred in January and the secondary maximum in the summer was smaller than the January emissions; however, the magnitude of the summer maximum substantially increased between the 1980s and the 1990s. It should also be noted that the seasonality in the residential and commercial sectors have not yet been included in the Vulcan inventory (Gurney et al., 2008). These emissions make up $\sim 11\%$ of the total emissions, and thus including their seasonality may alter the seasonal cycle.

Maps of the monthly distribution of the Vulcan emissions aggregated to the SiB3-RAMS domain are displayed in Figure 7.8. Consistent with the total seasonal cycle, broad-scale increases in fossil fuel emissions occur in early spring through the summer. Lower emissions are seen in February and in the fall (SOND). These

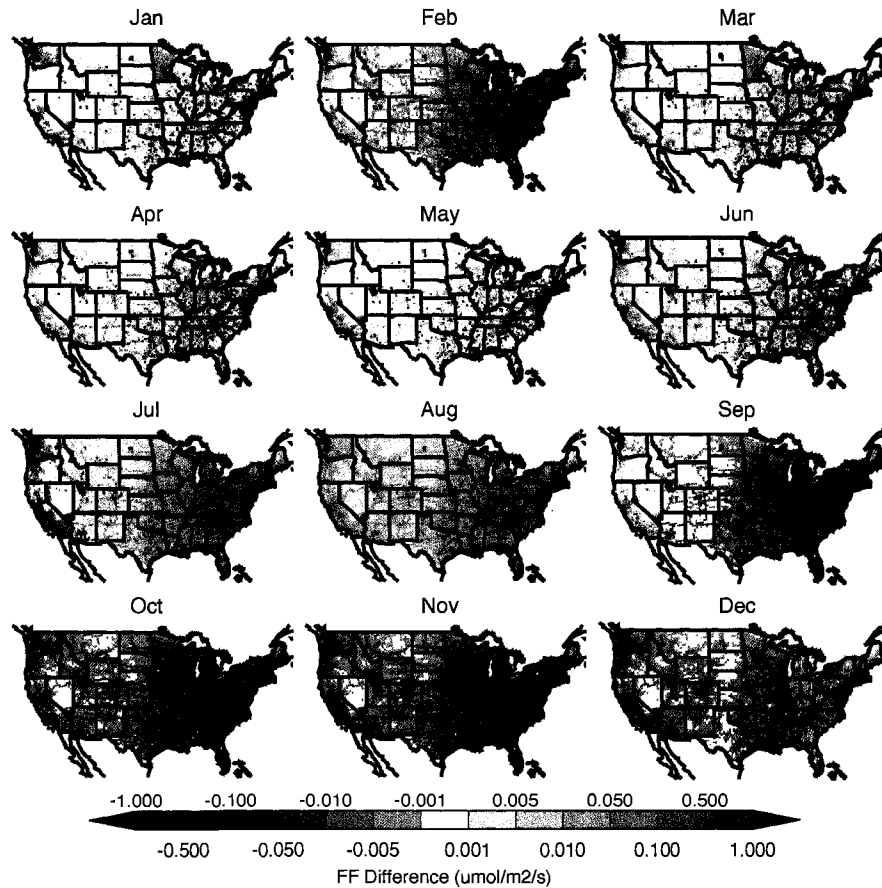


Figure 7.8: Seasonal cycle of the Vulcan fossil fuel emissions estimates. The fluxes shown are the differences between the monthly mean emissions and the annual mean emissions.

broad-scale changes are relatively small in magnitude ($< 1 \mu\text{mol m}^{-2} \text{s}^{-1}$), but are persistent over large areas. In general, the point sources follow a similar seasonal cycle as well; however, the seasonal cycle at several of the point sources does vary. For example, in Texas individual gridcells with emissions higher than the annual mean can be seen in September and October, with lower emissions during January and February. Both the broad-scale seasonality and the seasonality at smaller, individual gridcells will impact the atmospheric CO_2 concentrations.

Including seasonality in fossil fuel emissions impacts regional CO₂ concentrations on monthly timescales. Monthly differences in CO₂ concentrations at 30 m are shown in Figure 7.9. Differences due to including a seasonal cycle in the fossil fuel emissions can clearly be seen in the eastern half of the country. During the spring, concentrations over the east coast in the HRFF case are lower compared to the concentrations in the FF95 case, with changes of a few ppm. Moving to summer, concentrations over the eastern U. S. are higher in the HRFF case, and the magnitude of the differences increases. The largest differences between the two cases occur in August, where near-surface CO₂ is more than 15 ppm lower in the HRFF case at individual grid cells. On average, differences between 3-6 ppm are seen over the entire region. In the fall when the emissions decrease, the concentrations in the HRFF case also decrease, and broad-scale differences of 4-6 ppm on average occur in the southeast, with maximum differences in November. Between lower concentrations in the fall and higher concentrations in the summer, the amplitude of the seasonal differences is more than 20 ppm at some locations. The seasonality in the concentrations is less dramatic over the central and western United States, where the contribution of fossil fuel emissions to the total CO₂ concentrations is smaller.

In certain locations, the sign of the differences remain the same throughout the year, but the magnitude of the differences changes from month to month. Over Texas, the region of lower CO₂ between Dallas and Austin persists year-round, but the magnitude of the difference varies from ~ 1 ppm in the fall to

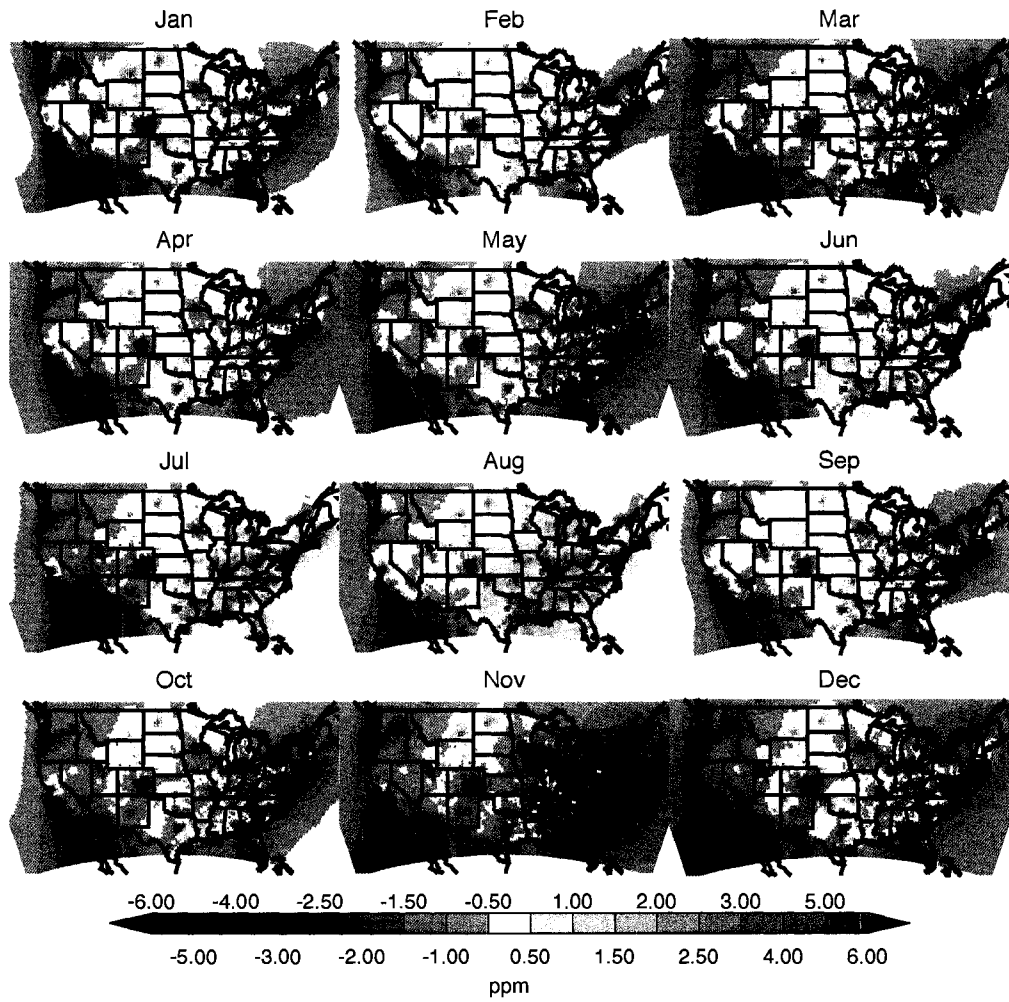


Figure 7.9: Monthly differences in the 30 m concentrations between the FF95 and the HRFF cases (HRFF - FF95).

over 3 ppm in the spring. Similar features can be seen over Montana and North Dakota, with differences between FF95 and HRFF varying from less than 1 ppm in September to more than 4 ppm in January. Over California, the changes due to spatial redistribution dominate over the seasonality in emissions, as the plume of low CO₂ concentration from the southern coastline persists throughout the year; however, differences of more than 15 ppm occur in November and December. Lower concentrations are also seen over Oregon and Washington year-round in the HRFF run, with a seasonal amplitude of ~ 2 -3 ppm.

7.4 Conclusions and Future Work

Although fossil fuel emissions are considered to be well known on national and annual scales, the emissions on finer spatial and temporal resolutions have high uncertainties. To improve these emissions estimates, Gurney et al. (2008) created the Vulcan database: a high-resolution fossil fuel emissions inventory over the United States with ~ 10 km horizontal grid spacing and a 1 hour timestep. The Vulcan inventory will be used in a variety of applications to advance our knowledge of the carbon cycle; thus it is essential to understand the impact these emissions have on CO₂ concentrations. In this study we investigated the effects of spatial and temporal redistribution of fossil fuel emissions on atmospheric CO₂ concentrations using a coupled ecosystem-atmosphere model.

This study showed that changes in the distribution and timing of fossil fuel emissions alter near-surface CO₂ concentrations on regional scales, particularly in

California and in the southern and eastern U. S. Comparisons between two simulations, one with coarse fossil fuel emissions (FF95, Andres et al. (1996)) and one with high-resolution emissions (HRFF, Gurney et al. (2008)) revealed minimal differences at 11 towers that measure CO₂ concentrations across the United States; however, these towers were all located in relatively remote regions. Larger differences in atmospheric CO₂ concentrations were seen on regional scales. Redistributing the fossil fuel emissions using a process-based model rather than scaling the estimates with population decreased the emissions over broad regions and increased the emissions in individual grid cells due to point sources. The resulting impact on the CO₂ concentrations was to create patterns of alternating high and low concentrations, particularly in the southern and eastern regions of the country, compared to concentrations from the coarse estimates. Differences of over 10 ppm on regional scales were seen near the surface, with the greatest differences over southern California, where the HRFF concentrations were much lower.

Including temporal resolution in fossil fuel emissions impacted regional CO₂ concentrations on monthly timescales. Monthly differences of 3-6 ppm on average occurred in the eastern United States. Compared to the FF95 case, the concentrations from the HRFF case were higher during the summer and lower the rest of the year in this region, and the amplitude of the seasonal differences was more than 20 ppm for many locations. Large differences were also seen over California, where the HRFF concentrations were consistently lower by more than 15 ppm during the winter.

The CO₂ concentration differences seen in this study indicate that redistributing fossil fuel emissions will impact atmospheric inversions. The differences between the FF95 and HRF cases were spatially coherent over large regions and were persistent on monthly timescales. This study demonstrated that using coarse spatial distributions and unaccounting for temporal variability created biases in the concentrations and thus may cause significant errors in source and sink estimates from atmospheric inversions.

Future work needs to be done to further investigate the Vulcan inventory. Comparisons of CO₂ concentrations at sites located closer to metropolitan areas should be performed to evaluate the database, and comparisons of atmospheric CO concentrations could also be conducted to help evaluate Vulcan. Case studies may highlight changes seen on local scales, including the effects of both seasonal changes in emissions as well as diurnal changes.

The diurnal cycle in Vulcan changes day-to-day and exhibits a distinct seasonality, with a maximum amplitude in the diurnal cycle during the winter. Future work should be done to investigate the impact of this variability on CO₂ concentrations. For this study, we calculated differences in the amplitude of monthly mean CO₂ diurnal cycles; but rather than reflecting the seasonal cycle of the diurnal amplitudes, the patterns matched the distributions of the monthly mean differences. Since analysis of the diurnal CO₂ cycle is difficult due to the strong covariance with the boundary layer depth, we conducted the same analysis using column concentrations and found that the differences were minimal (< 0.5 ppm).

These two analyses suggest the impact of the diurnal cycle in fossil fuel emissions is minimal compared with the seasonal changes; however, the diurnal cycle may have a large impact on local scales and should be investigated further.

Acknowledgements

Thank you to Kevin Gurney and Chris Miller at Purdue University for the Vulcan inventory and for help processing the dataset. Thanks also to all the data providers. This research was funded by NASA under subcontract 521-0438-01 from Purdue University.

8 Conclusions and Recommendations

8.1 Conclusions

Since the Industrial Revolution, atmospheric CO₂ concentrations are rapidly increasing from the combustion of fossil fuels and biomass burning; however, only about half of the anthropogenic CO₂ emissions accumulates in the atmosphere. The oceans and terrestrial biosphere must be taking up the remainder of the emissions, but the mechanism and location of this sink remains uncertain. A variety of approaches are used to investigate the missing sink of carbon, including bottom-up flux estimates from inventory data, regional extrapolation of local flux measurements, and top-down inverse modeling studies that use atmospheric CO₂ concentrations to estimate sources and sinks.

In order to advance our knowledge on carbon fluxes, it is important to understand the variability in atmospheric CO₂ concentrations. Originally, studies investigated the annual and diurnal cycles of CO₂ concentrations and the latitudinal gradient between the poles. As our understanding of the carbon cycle improved, focus began shifting from global scales down to regional scales; and synoptic-scale variability, which was once considered noise, is now being analyzed.

This study investigated causes of the variability in atmospheric CO₂ concentrations, focusing on the relationship between CO₂ concentrations and clouds, the impact of heterogeneous land cover and agricultural production, and the effect of redistributing fossil fuel emissions. The covariance of clouds and CO₂ concentrations, the productivity of agricultural crops, and the temporal variability in fossil fuel inventories all cause significant changes in atmospheric CO₂ concentrations. Knowledge that concentrations systematically vary with cloud cover on regional scales will help modelers optimally utilize satellite data; knowledge that concentrations are dramatically impacted by crops, which are large sinks of CO₂ during the growing season, as well as understanding the phenology driving this productivity, will help improve model estimates of both CO₂ fluxes and concentrations; and knowledge that the spatial and temporal distribution of fossil fuel emissions causes significant regional CO₂ concentration differences and thus must be properly accounted for will help improve source and sink estimates from atmospheric inversions.

Due to global sampling and sheer data volume, satellite total column CO₂ concentrations will be used in inverse modeling to improve estimates of CO₂ sources and sinks; however, satellite CO₂ concentrations, which have a footprint much smaller than typical model grid cells, will only be sampled in clear conditions. In order to optimally utilize these data, it is important to understand the regional variability of CO₂ concentrations between the satellite footprint and the model grid increment, and also the variability in concentrations due to cloud cover. An-

alyzing in situ continuous concentrations showed that atmospheric CO₂ concentrations were systematically lower on clear days than on average, likely due to advection rather than local fluxes. On a regional scale, simulations using a coupled ecosystem-atmosphere cloud-resolving model over both the mid-latitudes and the tropics revealed that the temporal variability of atmospheric total column CO₂ concentrations was much greater than the spatial variability over regions equivalent to model grid cells and that a single measurement collected in clear-sky conditions did not represent time-averages. Similar to the results from the local analysis, CO₂ concentrations over the mid-latitudes were systematically lower than the mean. Higher concentrations were due to frontal systems that covaried with cloud cover, causing these events not to be sampled. Expanding the analysis to the global scale showed similar results: regional differences in clear-sky concentrations compared to the mean occurred and varied with location and season.

Since CO₂ variability is related to cloud cover, which varies depending on meteorology, clear-sky measurements cannot be used to represent time-averages. To avoid introducing large errors, models must be sampled at the same time and in the same synoptic conditions, making model transport a priority to accurately capture the winds, clouds, fronts, and frontal timing. In contrast to the temporal errors, spatial differences were smaller than the expected spectroscopy errors, indicating that using satellite measurements sampled consistently in the model only over a smaller area will be representative of a model grid cell.

Just as CO₂ concentrations vary with sky conditions, CO₂ variability is also caused by surface fluxes. Using a coupled ecosystem-atmosphere model, SiB3-RAMS, we investigated the impacts of land cover heterogeneity and agricultural crops on the atmospheric CO₂ concentrations. Including sub-grid scale land cover heterogeneity and C4 vegetation improved the modeled concentrations by ~ 1 ppm; however, one of the deficiencies of the model was underestimating photosynthetic drawdown in agricultural ecosystems.

Including a crop phenological model for both corn and soybeans dramatically altered both CO₂ fluxes and concentrations. Compared with flux tower measurements, using the crop phenology model improved both the magnitude and the timing of the assimilation during the growing season. Using atmospheric CO₂ concentrations collected during the Mid-Continent Intensive (MCI) Campaign showed that including crops reduced the root mean square errors in the model by nearly 50% over the region. Simulating both corn and soybeans explicitly also improved the synoptic variability in the model.

The dramatic improvement in SiB3-RAMS showed that crops have a significant impact on atmospheric CO₂ concentrations. Both measured and modeled concentrations reached as low as 340 ppm over the mid-continent region during the summer of 2007. Combined with mesoscale meteorological variability, the intense uptake from crops lowered CO₂ concentrations and contributed to gradients of over 30 ppm near the surface over only ~ 200 km. Since crops influence both CO₂ fluxes and concentrations, it is important to model them accurately.

In addition to biological surface fluxes, surface emissions due to fossil fuel combustion also cause variability in regional atmospheric CO₂ concentrations. Using the coupled ecosystem-atmosphere model SiB3-RAMS, we performed a preliminary analysis of the effects of changes in the spatial and temporal distribution of fossil fuel emissions on atmospheric CO₂ concentrations. Using data combined with a process-based model to distribute the fossil fuel emissions rather than scaling the estimates with population caused differences of over 10 ppm near the surface, with the largest changes in California and in the eastern half of the United States. Including seasonality in the emissions impacted regional CO₂ concentrations on monthly timescales. Monthly differences of 3-6 ppm on average occurred in the eastern United States. Compared to the FF95 case, the concentrations from the HRFF case were higher during the summer and lower the rest of the year in this region, and the magnitude of the seasonal changes was more than 20 ppm at some locations. Large differences were also seen over California, where the HRFF concentrations were consistently lower by more than 15 ppm during the winter. Using coarse spatial distributions and unaccounting for temporal variability in fossil fuel emissions created biases in the atmospheric CO₂ concentrations and thus may cause significant errors in source and sink estimates from atmospheric inversions.

All three causes of variability investigated in this study significantly impacted regional CO₂ concentrations. Maximum total column CO₂ concentration differences for all three studies are displayed in Table 8.1. Including agricultural production by using a crop phenology model for corn and soybean had the greatest

Cause of Variability	Regional Difference (ppm)	
Satellite Clear-Sky	Spatial	0.8
	Temporal	2.2
Agricultural Production		4.
Fossil Fuel Redistribution	Spatial	0.9
	Temporal	2.3

Table 8.1: Total column variability due to the three causes investigated in this study: clear-sky concentrations from satellites, agricultural production, and fossil fuel redistribution. The values shown are the maximum total column differences, in ppm.

impact on CO₂ concentrations, causing regional changes of up to 4 ppm in the total column. The magnitudes of the differences caused by both clear-sky sampling and redistributing fossil fuel emissions are roughly half the magnitude of the changes from agricultural production. The differences due to temporal averaging of clear-sky conditions and temporally redistributing fossil fuel emissions are both ~ 2 ppm. The temporal differences are much greater than the spatial differences, which alter total column concentrations by < 1 ppm.

8.2 Recommendations for Future Work

While this study identified three important causes of atmospheric CO₂ variability, it is important to continue investigating causes of CO₂ variability and to continue improving models of both fluxes and concentrations. Regional differences between clear-sky concentrations and the mean occur globally and vary with both time and location; however, we did not investigate the mechanisms causing these differences.

The regional simulation and work by Parazoo et al. (2008) and Wang et al. (2007) show that in the mid-latitudes frontal systems combine and reorganize large-scale flux anomalies into narrow bands of high CO₂ associated with cloud cover via deformational flow. Further work into the mechanisms in other regions, particularly in the tropics and high northern latitudes, would help elucidate the causes of the clear-sky differences.

This research also showed that using clear-sky total column CO₂ measurements to represent time averages would cause significant errors in atmospheric CO₂ inversions. Future work could be done to determine the utility of satellite concentrations in inversions, focusing on the effects of sampling only in clear conditions. An analysis of an inversion using all possible satellite data (including simulated concentrations under clouds) versus an inversion that include only clear-sky soundings would reveal differences due to the cloud cover and potential under-sampling of the synoptic variability. Although several studies have investigated the usefulness of satellite CO₂ concentrations (e.g. Houweling et al., 2004; Baker et al., 2006a; Chevallier et al., 2007), none has focused on the impacts of sampling concentrations only in clear conditions.

Focusing on the variability driven by agricultural productivity rather than meteorology, future work could be done regarding the impact of agricultural ecosystems on atmospheric concentrations. Since we only included crops over a limited region, future work to determine the impact of crops over the entire U. S. is required. To do this, a necessary first step is to create maps of crop coverage for the

entire U. S. Model simulations using the corn and soybean crop phenology model could also be evaluated against other data collected during the MCI campaign, such as carbon stocks and annual crop yield. Evaluating the model against additional independent data would help to identify shortcomings and lead to model improvement. Other crops could also be simulated using a phenological submodel, such as wheat and rice.

Several different analyses into the model behavior would help to improve the model performance and our understanding of various processes. The model evaluation in this study showed that the fluxes over northeastern forested regions underestimated the drawdown. While this was likely due to these regions being strong sinks of carbon not included in the model, further investigation into representing forest cover at various stages in development may help improve the fluxes for this biome type. The simulations in the study were very sensitive to vegetation stress, and the stresses in the coupled model were quite different than the stresses in the offline model used for spin-up. A further analysis into the causes of the stress may help reveal the sensitivity of the model to various parameters. One potential cause for the different stress is the meteorological driver data, and an investigation into different options, such as National Centers for Environmental Prediction North American Regional Reanalysis data and meteorological data from the European Center for Medium-Range Weather Forecast may be beneficial. One other problem we noticed while performing this study is that while changes in temperature, pressure, and winds in the model were simulated well, variability

in shortwave radiation seemed to be underestimated and not well correlated with observations. Analysis and further investigation of different radiation parameterizations may help improve simulations. The day-to-day variability in fluxes could also be improved by including shaded and direct fractions of solar radiation.

References

- Amiro, B. D., A. G. Barr, T. A. Black, H. Iwashita, N. Kljun, J. H. McCaughey, K. Morgenstern, S. Murayama, Z. Nesie, A. L. Orchansky, and N. Saigusa, 2006: Carbon, energy, and water fluxes at mature and disturbed forest sites, saskatchewan, canada. *Agric. For. Meteorol.*, **136**, 237–251.
- Andres, R. J., G. Marland, I. Fung, and E. Matthews, 1996: A $1^\circ \times 1^\circ$ distribution of carbon dioxide emissions from fossil fuel consumption and cement manufacture. *Global Biogeochem. Cycles*, **10**, 419–429.
- Arrhenius, S., 1896: On the influence of carbonic acid upon temperature at the ground. *Phil. Mag.*, **41**, 327.
- Aubinet, M., A. Grelle, A. Ibrom, U. Rannik, J. Moncrieff, T. Foken, A. S. Kowalski, P. H. Martin, P. Berbigier, C. Bernhofer, R. Clement, J. Elbers, A. Granier, T. Grunwald, K. Morgenstern, K. Pilegaard, C. Rebmann, W. Snijders, R. Valentini, and T. Vesala, 2000: Estimates of the annual net carbon and water exchange of forests: The euroflux methodology. *Adv. Eco. Res.*, **30**, 113–175.
- Aumann, H. H., M. T. Chahine, C. Gautier, M. D. Goldberg, E. Kalnay, L. M. McMillin, H. Revercomb, P. W. Rosenkranz, W. L. Smith, D. H. Staelin, L. L. Strow, and J. Susskind, 2003: Airs/amsu/hsb on the aqua mission: Design, science objectives, data products and processing systems. *IEEE Trans. Geosci. Remote Sens.*, **41**, 253–264.
- Avissar, R. and R. A. Pielke, 1989: A parameterization of heterogeneous land-surface for atmospheric numerical models and its impact on regional meteorology. *Monthly Weather Review*, **117**, 2113–2136.
- Bacastow, R. B., 1976: Modulation of atmospheric carbon dioxide by the southern oscillation. *Nature*, **261**, 116–118.

- Bach, W., A. J. Crane, A. L. Berger, and A. Longhetto, 1983: Carbon dioxide: Current views and developments in energy/climate research, D. Reidel Publishing Company, Dordrecht, Holland.
- Baker, D. R., S. C. Doney, and D. S. Schimel, 2006a: Variational data assimilation for atmospheric CO_2 . *Tellus Ser. B*, **58**, 359–365.
- Baker, D. R., R. M. Law, K. R. Gurney, P. Rayner, P. Peylin, A. S. Denning, P. Bousquet, L. Bruhwiler, Y. H. Chen, P. Ciais, I. Y. Fung, M. Heimann, J. John, T. Maki, S. Maksyutov, K. Masarie, M. Prather, B. Pak, S. Taguchi, and Z. Zhu, 2006b: Transcom 3 inversion intercomparison: Impact of transport model errors on the interannual variability of regional CO_2 fluxes, 1988–2003. *Global Biogeochem. Cycles*, **20**, GB1002, doi:10.1029/2004GB002439.
- Baker, I. T., A. S. Denning, N. Hanan, L. Prihodko, M. Uliasz, P. L. Vidale, K. Davis, and P. Bakwin, 2003: Simulated and observed fluxes of sensible and latent heat at the wlef-tv tower using sib 2.5. *Global Change Biol.*, **9**, doi:10.1046/j.13652486.2003.00671.
- Baker, I. T., A. S. Denning, L. Prihodko, K. Schaefer, J. A. Berry, G. J. Collatz, N. S. Suits, R. Stockli, A. Philpott, and O. Leonard, 2007: Global net ecosystem exchange (nee) of CO_2 , Oak Ridge National Laboratory Distributed Active Archive Center, Oak Ridge, Tennessee, USA, available at <http://www.daac.ornl.gov>.
- Baker, I. T., D. Zupanski, L. Prihodko, K. Schaefer, J. Berry, and A. S. Denning, 2005: Leaf-to-canopy scaling of carbon, energy, and moisture fluxes in the simple biosphere model (sib). *EOS Trans. AGU*, **86**, Fall Meet. Suppl., Abstract B51C–0228.
- Bakwin, P. S., K. J. Davis, C. Yi, S. C. Wosfy, J. W. Munger, L. Haszpra, and Z. Barcza, 2004: Regional carbon dioxide fluxes from mixing ratio data. *Tellus Ser. B*, **56**, 301–311.
- Bakwin, P. S., P. P. Tans, D. F. Hurst, and C. Zhao, 1998: Measurements of carbon dioxide on very tall towers: Results of the noaa/cmdl program. *Tellus Ser. B*, **50**, 401–415.
- Baldocchi, D., 2006: Fluxnet: A global network measuring and assessing spatial-temporal variability of carbon dioxide, water vapor, and energy fluxes between

- the terrestrial biosphere and the atmosphere, National Science Foundation Research Coordination Networks in Biological Sciences, Report NSF 06–567.
- Baldocchi, D., E. Falge, L. H. Gu, and R. Olson, 2001: Fluxnet: A new tool to study the temporal and spatial variability of ecosystem-scale carbon dioxide, water, and energy flux densities. *Bull. Amer. Meteor. Soc.*, **82**, 2415–2434.
- Ball, J. T., 1988: An analysis of stomatal conductance, Ph.D. Diss., Stanford University, 89 pp.
- Barnston, A. G. and R. G. Livezey, 1987: Classification, seasonality, and persistence of low-frequency atmospheric circulation patterns. *Monthly Weather Review*, **115**, 1083–1126.
- Battle, M., M. L. Bender, P. Tans, J. W. C. White, J. T. Ellis, T. Conway, and R. J. Francey, 2000: Global carbon sinks and their variability inferred from atmospheric O_2 and $\delta^{13}\text{C}$. *Science*, **287**, 2467–2470.
- Blasing, T. J., C. T. Broniak, and G. Marland, 2005: The annual cycle of fossil-fuel carbon dioxide emissions in the united states. *Tellus Ser. B*, **57**, 107–115.
- Bloom, S., A. da Silva, D. Dee, M. Bosilovich, J. D. Chern, S. Pawson, S. Schubert, M. Sienkiewicz, I. Stajner, W. W. Tan, and M. L. Wu, 2005: Documentation and validation of the goddard earth observing system (geos) data assimilation system - version 4, Tech. Rep. 1046066, V26, NASA.
- Bolin, B. and W. Bischof, 1970: Variations of the carbon dioxide content of the atmosphere in the northern hemisphere. *Tellus Ser. B*, **22**, 431.
- Bolin, B. and C. D. Keeling, 1963: Large scale atmospheric mixing as deduced from the seasonal and meridional variations in carbon dioxide. *J. Geophys. Res.*, **68**, 3899.
- Broecker, W. S., T. Takahashi, H. J. Simpson, and T. H. Peng, 1979: Fate of fossil fuel carbon dioxide and the global carbon budget. *Science*, **206**, 409–417.
- Buchwitz, M., R. de Beek, S. Noël, P. Burrows, H. Bovensmann, H. Bremer, P. Bergamaschi, S. Körner, and M. Heimann, 2005: Carbon monoxide, methane and carbon dioxide columns retrieved from sciamachy by wfm-doas: Year 2003 initial data set. *Atmos. Chem. Phys.*, **5**, 3313–3329.

- Callendar, G. S., 1940: Variation of the amount of CO_2 in various air currents. *Quat. Journ. Roy. Met. Soc.*, **66**, 395.
- 1958: On the amount of carbon dioxide in the atmosphere. *Tellus Ser. B*, **10**, 243.
- Chamberlain, T. C., 1899: An attempt to form a working hypothesis of the cause of glacial periods on an atmospheric basis. *J. Geology*, **6**, 545.
- Chan, D., W. Y. Chiu, K. Higuchi, A. Shashkov, J. Liu, J. Chen, and D. Worthy, 2004: On the CO_2 exchange between the atmosphere and the biosphere: The role of synoptic and mesoscale processes. *Tellus Ser. B*, **56**, 194–212.
- Chang, J., M. C. Hansen, K. Pittman, M. Carroll, and C. DiMiceli, 2007: Corn and soybean mapping in the united states using modis time-series data sets. *Agron. J.*, **99**, 1654–1664, doi:10.2134/agronj2007.0170.
- Chen, J. Q., K. T. P. U, S. L. Ustin, T. H. Suchanek, B. J. Bond, K. D. Brosofske, and M. Falk, 2004: Net ecosystem exchange of carbon, water, and energy in young and old growth douglas-fir forests. *Ecosystems*, **7**, 534–544.
- Chevallier, F., F. M. Bréon, and P. J. Rayner, 2007: Contribution of the orbiting carbon observatory to the estimation of CO_2 sources and sinks: Theoretical study in a variational data assimilation framework. *J. Geophys. Res.*, **112**, D09307, doi:10.1029/2006JD007375.
- Chevallier, F., R. J. Engelen, and P. Peylin, 2005: The contribution of airs data to the estimation of CO_2 sources and sinks. *Geophys. Res. Letters*, **32**, L23801, doi:10.1029/2005GL024229.
- Clark, T. L. and R. D. Farley, 1984: Severe downslope windstorm calculations in two and three spial dimensions using anelastic interactive grid nesteing: A possible mechanism for gustiness. *J. Atmos. Sci*, **41**, 329–350.
- Cohen, W. B., T. K. Maersperger, Z. Yang, S. T. Gower, D. P. Turner, W. D. Ritts, M. Berterretche, and S. W. Running, 2003: Comparisons of land cover and lai estimates derived from etm and modis for four sites in north america: a quality assessment of 2000/2001 provisional modis products. *Rem. Sens. Env.*, **88**, 221–362.

- Collatz, G. J., J. T. Ball, C. Grivet, and J. A. Berry, 1991: Physiological and environmental regulation of stomatal conductance, photosynthesis and transpiration: A model that includes a laminar boundary layer. *Agric. For. Meteorol.*, **54**, 107–136.
- Collatz, G. J., M. Ribas-Carbo, and J. A. Berry, 1992: Coupled photosynthesis-stomatal conductance model for leaves of c4 plants. *Aus. J. Plant Phys.*, **19**, 519–538.
- Conway, T. J., P. P. Tans, L. S. Waterman, and K. W. Thoning, 1994: Evidence for interannual variability of the carbon cycle from the national oceanic and atmospheric administration climate monitoring and diagnostics laboratory global air sampling network. *J. Geophys. Res.*, **99**, 22831.
- Conway, T. J., P. P. Tans, L. S. Waterman, K. W. Thoning, K. A. Masarie, and R. H. Gammon, 1988: Atmospheric carbon dioxide measurements in the remote global troposphere. *Tellus Ser. B*, **40**, 81–115.
- Corbin, K. D. and A. S. Denning, 2006: Using continuous data to estimate clear-sky errors in inversions of satellite CO_2 measurements. *Geophys. Res. Letters*, **33**, L12810, doi:10.1029/2006GL025910.
- Corbin, K. D., A. S. Denning, L. Lu, J. W. Wang, and I. T. Baker, 2008: Using a high-resolution coupled ecosystem-atmosphere model to estimate representation errors in inversions of satellite CO_2 retrievals. *J. Geophys. Res.*, **113**, D02301, doi:10.1029/2007JD008716.
- Cotton, W. R., R. A. Pielke, R. L. Walko, G. E. Liston, C. J. Tremback, H. Jiang, R. L. McAnelly, J. Y. Harrington, M. E. Nicholls, C. G. Carrio, and J. P. McFadden, 2002: Rams 2001: Current status and future directions. *Meteorol. Atmos. Phys.*, **82**, doi:10.1007/s00703-001-0584-9.
- Crisp, D., R. M. Atlas, F. M. Breon, L. R. Brown, J. P. Burrows, P. Ciais, B. J. Connor, S. C. Doney, I. Y. Fung, D. J. Jacob, C. E. Miller, D. O'Brien, S. Pawson, J. T. Randerson, P. Rayner, R. J. Salawitch, S. P. Sander, B. Sen, G. L. Stephens, P. P. Tans, G. C. Toon, P. O. Wennberg, S. C. Wofsy, Y. L. Yung, Z. Kuang, B. Chudasama, G. Sprague, B. Weiss, R. Pollock, D. Kenyon, and S. Schroll, 2004: The orbiting carbon observatory (oco) mission. *Adv. Space Res.*, **34**, 700–709.

- Dai, Y., X. Zeng, R. E. Dickinson, I. Baker, G. B. Bonan, M. G. Bosilovich, A. S. Denning, P. A. Dirmeyer, P. R. Houser, G. Niu, K. W. Oleson, C. A. Schlosser, and Z. L. Yang, 2003: The common land model. *Bull. Amer. Meteor. Soc.*, **84**, 1013–1023.
- Dargaville, R., D. Baker, C. Rodenbeck, P. Rayner, and P. Ciais, 2005: Estimating high latitude carbon fluxes with inversions of atmospheric CO_2 . *Mitigation and Adaptation Strategies for Global Change*, **11**, 769–782.
- Davis, K. J., P. S. Bakwin, C. Yi, W. Berger, C. Zhao, R. M. Teclaw, and J. S. Isebrands, 2003: The annual cycle of CO_2 and H_2O exchange over a northern mixed forest as observed from a very tall tower. *Global Change Biol.*, **9**, 1278–1293.
- Davis, K. J., D. H. Lenschow, S. P. Oneley, C. Kiemle, G. Ehret, A. Giez, and J. Mann, 1997: Role of entrainment in surface-atmosphere interactions over the boreal forest. *J. Geophys. Res.*, **102**, 29219–29230.
- Denman, K. L., G. Brasseur, A. Chidthaisong, P. Ciais, P. M. Cox, R. E. Dickinson, D. Hauglustaine, C. Heinze, E. Holland, D. Jacob, U. Lohmann, S. Ramachandran, P. L. da Silva Dias, S. C. Wofsy, and X. Zhang, 2007: Couplings between changes in the climate system and biogeochemistry. *Climate Change 2007: The Physical Science Basis. Contribution of Working Group I to the Fourth Assessment Report of the Intergovernmental Panel on Climate Change*, [Solomon, S., D. Qin, M. Manning, Z. Chen, M. Marquis, K. B. Averyt, M. Tignor and H. L. Miller (eds.)]. Cambridge University Press, Cambridge, United Kingdom and New York, NY USA.
- Denning, A. S., J. G. Collatz, C. Zhang, D. A. Randall, and J. A. Berry, 1996a: Simulations of terrestrial carbon metabolism and atmospheric CO_2 in a general circulation model. part 1: Surface carbon fluxes. *Tellus Ser. B*, **48**, 521–542.
- Denning, A. S., S. Doney, D. Zupanski, R. Kawa, J. Collatz, and S. Pawson, 2007: Current capabilities and future directions for carbon cycle data assimilation, AMS annual meeting, January 15–18, San Antonio, TX, USA.
- Denning, A. S., M. Nicholls, L. Prihodko, I. Baker, P. L. Vidale, K. Davis, and P. Bakwin, 2003: Simulated variations in atmospheric CO_2 over a wisconsin forest using a coupled ecosystem-atmosphere model. *Global Change Biol.*, **9**, 1–10.

- Denning, A. S., D. A. Randall, G. J. Collatz, and P. J. Sellers, 1996b: Simulations of terrestrial carbon metabolism and atmospheric CO_2 in a general circulation model. part 2: Spatial and temporal variations of atmospheric CO_2 . *Tellus Ser. B*, **48**, 453–567.
- Desai, A. R., P. V. Bolstad, B. D. Cook, K. J. Davis, and E. V. Carey, 2005: Comparing net ecosystem exchange of carbon dioxide between an old-growth and mature forest in the upper midwest, usa. *Agric. For. Meteorol.*, **128**, 33–55.
- Dickinson, R. E., M. Shaikh, R. Bryant, and L. Graumlich, 1998: Interactive canopies for a climate model. *J. Climate*, **11**, 2823–2836.
- Dixon, R. K., S. Brown, R. A. H. and dA. M. Solomon and dM. C. Trexler, and J. Wisniewski, 1994: Carbon pools and flux of global forest ecosystems. *Science*, **263**, 185–190.
- Dunn, A. L., C. C. Barford, S. C. Wofsy, M. L. Goulden, and B. C. Daube, 2007: A long-term record of carbon exchange in a boreal black spruce forest: means, responses to interannual variability and decadal trends. *Global Change Biol.*, **13**, 577–590.
- EIA, 2007: Emissions of greenhouse gases report. *Report DOE/EIA 0573*, Office of Integrated Analysis and Forecasting, U. S. Department of Energy, Energy Information Administration, Washington, D. C.
- Engelen, R. J., E. Andersson, F. Chevallier, A. Hollingsworth, M. Matricardi, A. P. McNally, J. N. Thepaut, and P. D. Watts, 2004: Estimating atmospheric CO_2 from advanced infrared satellite radiances within an operational 4d-var data assimilation system: Methodology and first results. *J. Geophys. Res.*, **109**, D19309, doi:10.1029/2004JD004777.
- Engelen, R. J., A. S. Denning, and K. R. Gurney, 2002: On error estimation in atmospheric CO_2 inversions. *J. Geophys. Res.*, **107**, doi:10.1029/2002JD002195.
- Enting, I. G., C. M. Trudinger, and R. J. Francey, 1995: A synthesis inversion of the concentration and ^{13}C of atmospheric CO_2 . *Tellus Ser. B*, **47**, 35–52.
- Essery, R. L. H., M. J. Best, R. A. Betts, and P. M. Cox, 2002: Explicit representation of subgrid heterogeneity in a gcm land surface scheme. *J. Hydrometeorol.*, **4**, 530–543.

- Eugster, W. and F. Siegrist, 2000: The influence of nocturnal CO_2 advection on CO_2 flux measurements. *Basic Appl. Ecol.*, **1**, 177–188.
- Falge, E., D. Baldocchi, R. Olson, P. Anthoni, M. Aubinet, C. Bernhofer, G. Burba, R. Ceulemans, R. Clement, H. Dolman, A. Granier, P. Gross, T. Grunwald, D. Hollinger, H.-O. Jensen, G. Katul, P. Keronen, A. Kowalski, C. T. Lai, B. E. Law, T. Meyers, J. Moncrieff, E. Moors, J. W. Munger, K. Pilegaard, U. Rannik, C. Rebmann, A. Suyker, J. Tenhunen, K. Tu, S. Verma, T. Vesela, K. Wilson, and S. Wofsy, 2001: Gap filling strategies for defensible annual sums of net ecosystem exchange. *Agric. For. Meteorol.*, **107**, 43–69.
- Falge, E., J. Tenhunen, D. Baldocchi, M. Aubinet, P. Bakwin, P. Berbigier, C. Bernhofer, J. M. Bonnefond, G. Burba, R. Clement, K. J. Davis, J. A. Elbers, M. Falk, A. H. Goldstein, A. Grelle, A. Granier, T. Grunwald, J. Gudmundsson, D. Hollinger, I. A. Janssens, P. Keronen, A. S. Kowalski, G. Katul, B. E. Law, Y. Malhi, T. Meyers, R. K. Monson, E. Moors, J. W. Munger, W. U. K. T. P. Oechel, K. Pilegaard, U. Rannik, C. Rebmann, A. Suyker, H. Thorgeirsson, G. Tirone, A. Turnipseed, K. Wilson, and S. Wofsy, 2002: Phase and amplitude of ecosystem carbon release and uptake potential as derived from fluxnet measurements. *Agric. For. Meteorol.*, **113**, 75–95.
- Farquhar, G. D., S. von Caemmerer, and J. A. Berry, 1980: A biochemical model of photosynthetic CO_2 fixation in leaves of C_3 species. *Planta*, **149**, 78–90.
- Fischer, M. L., D. P. Billesbach, W. J. Riley, J. A. Berry, and M. S. Torn, 2007: Spatiotemporal variations in growing season exchanges of CO_2 , H_2O , and sensible heat in agricultural fields of the southern great plains. *Earth Interactions*, **11**, Paper 17, 21 pp.
- Flanagan, L. B. and B. G. Johnson, 2005: Interacting effects of temperature, soil moisture and plant biomass production on ecosystem respiration in a northern temperate grassland. *Agric. For. Meteorol.*, **130**, 237–253.
- Flanagan, L. B., L. A. Wever, and P. J. Carlson, 2002: Seasonal and interannual variation in carbon dioxide exchange and carbon balance in a northern temperate grassland. *Global Change Biol.*, **8**, 599–615.
- Freedman, J. M., D. R. Fitzjarrald, K. E. Moore, and R. K. Sakai, 2001: Boundary layer clouds and vegetation-atmosphere feedbacks. *J. Climate*, **14**, 180–197.

- Frietas, S. R., K. Longo, M. S. Dias, P. S. Dias, R. Chatfield, Á. Fazenda, and L. F. Rodrigues, 2006: The coupled aerosol and tracer transport model to the barzilian developments on the regional atmospheric modeling system: Validation using direct and remote sensing observations. *Am. Meteorol. Soc.*, paper presented at 8th International Conference on Southern Hemisphere Meteorology and Oceanography, Foz do Iguacu, Brazil.
- Gamnitzer, U., U. Karstens, B. Kromer, R. E. M. Neubert, H. A. J. Meijer, H. Schroeder, and I. Levin, 2006: Carbon monoxide: A quantitative tracer for fossil fuel CO_2 ? *J. Geophys. Res.*, **111**, D22302, doi:10.1029/2005JD006966.
- Geels, C., S. C. Doney, R. Dargaville, J. Brandt, and J. H. Christensen, 2004: Investigating the sources of synoptic variability in atmospheric CO_2 measurements over the northern hemisphere continents: a regional model study. *Tellus Ser. B*, **56**, 35–50.
- Gerbig, C., J. C. Lin, S. C. Wofsy, B. C. Daube, A. E. Andrews, B. B. Stephens, P. S. Bakwin, and C. A. Grainger, 2004: Toward constraining regional-scale fluxes of CO_2 with atmospheric observations over a continent: 1. observed spatial variability from airborne platforms. *J. Geophys. Res.*, **108**, 4756, doi:10.1029/2002JD003018.
- Gilmanov, T. G., L. L. Tieszen, B. K. Wylie, L. B. Flanagan, A. B. Frank, M. R. Haferkamp, T. P. Meyers, and J. A. Morgan, 2005: Integration of CO_2 flux and remotely-sensed data for primary production and ecosystem respiration analyses in the northern great plains: potential for quantitative spatial extrapolation. *Global Ecol. Biogeogr.*, **14**, 271–292.
- Giorgi, F. and R. Avissar, 1997: Representation of heterogeneity effects in earth system modeling: Experience from land surface modeling. *Rev. Geophys.*, **35**, 413–438.
- Goodale, C. L., M. J. Apps, R. A. Birdsey, C. B. Field, L. S. Heath, R. A. Houghton, J. C. Jenkins, G. H. Kohlmaier, W. A. Kurz, S. Liu, G. J. Naburs, and S. N. and A. Z. Shvidenko, 2002: Forest carbon sinks in the northern hemisphere. *Ecol. Appl.*, **12**, 891–899.
- Goulden, M. L., B. C. Daube, S. M. Fan, D. Sutton, A. Bazzaz, J. Munger, and

- S. Wofsy, 1997: Physiological responses of a black spruce forest to weather. *J. Geophys. Res.*, **102**, (D24), 28987–28996.
- Goulden, M. L., J. M. Munger, S. M. Fan, B. C. Daube, and S. C. Wofsy, 1996: Exchange of carbon dioxide by a deciduous forest: Response to interannual climate variability. *Science*, **271**, 1576–1578.
- Grell, G. A., 1993: Prognostic evaluation of assumptions used by cumulus parameterizations. *Monthly Weather Review*, **119**, 5–31.
- Grell, G. A. and D. Devenyi, 2002: A generalized approach to parameterizing convection combining ensemble and data assimilation techniques. *Geophys. Res. Letters*, **29**, 1693–1704.
- Gu, L., D. Baldocchi, S. B. Verma, T. A. Black, T. Vesala, E. M. Falge, and P. R. Dowty, 2002: Advantages of diffuse radiation for terrestrial ecosystem productivity. *J. Geophys. Res.*, **107**, 4050, doi:10.1029/2001JD001242.
- Gurney, K. R., W. Ansley, D. Mendoza, G. Petron, G. Frost, J. Gregg, M. Fischer, D. Pataki, K. Ackerman, S. Houweling, K. Corbin, R. Andres, and T. J. Blasing, 2007: Research needs for finely resolved fossil carbon emissions. *EOS Trans. AGU*, **88**, 542–543.
- Gurney, K. R., Y. H. Chen, T. Maki, S. R. Kawa, A. Andrews, and Z. Zhu, 2005: Sensitivity of atmospheric CO₂ inversions to seasonal and interannual variations in fossil fuel emissions. *J. Geophys. Res.*, **110**, D10308, doi:10.1029/2004JD005373.
- Gurney, K. R., R. M. Law, A. S. Denning, P. J. Rayner, D. Baker, P. Bousquet, L. Bruhwiler, Y. H. Chen, P. Ciais, S. Fan, I. Y. Fung, M. Gloor, M. Heimann, K. Higuchi, J. John, E. Kowalczyk, T. Maki, S. Maksyutov, P. Peylin, M. Prather, B. C. Pak, J. Sarmiento, S. Taguchi, T. Takashi, and C. W. Yuen, 2003: Transcom 3 CO₂ inversion intercomparison: 1. annual mean control results and sensitivity to transport and prior flux information. *Tellus Ser. B*, **55**, 555–579.
- Gurney, K. R., R. M. Law, A. S. Denning, P. J. Rayner, D. Baker, P. Bousquet, L. Bruhwiler, Y. H. Chen, P. Ciais, S. Fan, I. Y. Fung, M. Gloor, M. Heimann, K. Higuchi, J. John, T. Maki, S. Maksyutov, K. Masarie, P. Peylin, M. Prather, B. C. Pak, J. Randerson, J. Sarmiento, S. Taguchi, T. Takahashi, and C. W.

- Yuen, 2002: Towards robust regional estimates of CO₂ sources and sinks using atmospheric transport models. *Nature*, **415**, 626–630.
- Gurney, K. R., B. Seib, W. Ansley, D. Mendoza, M. Fischer, C. Miller, and S. Murtishaw, 2008: The vulcan inventory, version 1.0, Purdue University, <http://www.purdue.edu/eas/carbon/vulcan/research.html>.
- Hansen, M., 2008: Corn and soybean mapping in the united states using modis time-series data sets. *Agron. J.*, Accepted.
- Hansen, M., R. DeFries, J. R. G. Townshend, and R. Sohlberg, 2000: Global land cover classification at 1 km resolution using a decision tree classifier. *Int. J. Remote Sensing*, **21**, 1331–1365.
- Harrington, J. Y., 1997: The effects of radiative and microphysical processes on simulated warm and transition season arctic stratus. *Atmos. Sci. Pap.*, **637**, 289 pp., Dep. of Atmos. Sci., Colo. State Univ., Fort Collins, Colo.
- Heimann, M., 2001: The carbon cycle and atmospheric CO₂. *Atmospheric Inversion Calculations Performed for IPCC Third Assessment Report*, chap. 3, Max-Planck Inst. Biogeochem., Jena, Germany.
- Hollinger, D. Y., J. Aber, B. Dail, A. Davidson, S. M. Goltz, H. Hughes, M. Y. Leclerc, J. T. Lee, A. D. Richardson, C. Rodrigues, N. A. Scott, D. Achuatavrier, and J. Walsh, 2004: Spatial and temporal variability in forest-atmosphere CO₂ exchange. *Global Change Biol.*, **10**, 1689–1706.
- Houghton, R. A., 1999: The annual net flux of carbon to the atmosphere from changes in land use 1850-1990. *Tellus Ser. B*, **51**, 298–313.
- House, J. I., I. C. Prentice, N. Ramankutty, R. A. Houghton, and M. Heimann, 2003: Reconciling apparent inconsistencies in estimates of terrestrial CO₂ sources and sinks. *Tellus Ser. B*, **55**, 345–363.
- Houweling, S., F. M. Breon, I. Aben, C. Rödenbeck, M. Gloor, M. Heimann, and P. Ciais, 2004: Inverse modeling of CO₂ sources and sinks using satellite data: A synthetic inter-comparison of measurement techniques and their performance as a function of space and time. *Atmos. Chem. Phys.*, **4**, 523–538.

- Howell, T. A., S. R. Evett, J. A. Tolk, A. D. Schneider, and J. L. Steiner, 1996: Evapotranspiration of corn – southern high plains. *Evapotranspiration and Irrigation Scheduling*, Proceedings of the International Conference, Nov. 3–6, San Antonio, TX, American Society of Agricultural Engineers, St. Joseph, MI.
- Humphreys, E. R., T. A. Black, G. J. Ethier, G. B. Drewitt, D. L. Sipplehouse, E. M. Jork, Z. Nesie, and N. J. Livingston, 2003: Annual and seasonal variability of sensible and latent heat fluxes above a coastal douglas-fir forest, british columbia, canada. *Agric. For. Meteorol.*, **115**, 109–125.
- IGBP, 2000: Global soil data products cd-rom (igbp-dis) [cd-rom]. *Int. Geosphere-Biosphere Programme*, Global Soil Data Task, Int. Geosphere-Biosphere Programme, Data and Inf. Syst., Potsdam, Germany. (Available from Oak Ridge Natl. Lab. Distrib. Active Arch. Cent., Oak Ridge, Tenn., <http://www.daac.ornl.gov>).
- Jacobson, A. R., S. E. Mikaloff-Fletcher, N. Gruber, J. L. Sarmiento, and M. Gloor, 2007: A joint atmosphere-ocean inversion for surface fluxes of carbon dioxide: 2. regional results. *Global Biogeochem. Cycles*, **21**, doi:10.1029/2006GB002703.
- Janssens, I. A., A. Freibauer, P. Ciais, P. Smith, G. J. Nabuurs, G. Folberth, B. Schlamadinger, R. W. A. Hutjes, R. Ceulemans, E. D. Schulze, R. Valentini, and A. J. Dolman, 2003: Europe's terrestrial biosphere absorbs 7 to 12% of european anthropogenic co₂ emissions. *Science*, **300**, 1538–1542.
- Jones, B. P., D. L. Holshouser, M. M. Alley, J. K. F. Roygard, and C. M. Anderson-Cook, 2003: Double-crop soybean leaf area and yield responses to mid-atlantic soils and cropping systems. *Agron. J.*, **95**, 436–445.
- Jones, C. D. and P. M. Cox, 2001: Modeling the volcanic signal in the atmospheric co₂ record. *Global Biogeochem. Cycles*, **15**, 453–465.
- Kalnay, E., M. Kanamitsu, R. Kistler, W. Collins, D. Deaven, L. Gandin, M. Iredell, S. Saha, G. White, J. Woollen, Y. Zhu, M. Chelliah, W. Ebisuzaki, W. Higgins, J. Janowiak, K. C. Mo, C. Ropelewski, J. Wang, A. Leetmaa, R. Reynolds, R. Jenne, and D. Joseph, 1996: The ncep/ncar 40-year reanalysis project. *Bull. Amer. Meteor. Soc.*, **77**, 437–471.

- Kawa, S. R., D. J. E. III, S. Pawson, and Z. Zhu, 2004: Global CO_2 transport simulations using meteorological data from the nasa data assimilation system. *J. Geophys. Res.*, **109**, D18312, doi:10.1029/2004JD004554.
- Keeling, C. D., R. B. Bacastow, A. E. Bainbridge, C. A. Ekdahl, P. R. Guenther, and L. S. Waterman, 1976: Atmospheric carbon dioxide variations at mauna loa observatory hawaii. *Tellus Ser. B*, **28**, 538.
- Keeling, C. D., R. B. Bacastow, A. F. Carter, S. C. Piper, T. P. Whorf, M. Heimann, M. G. Mook, and H. Roeloffzen, 1989: A three-dimensional model of atmospheric CO_2 transport based on observed winds: I. analysis of observational data. *Aspects of Climate Variability in the Pacific and the Western Americas*, **55**, chap. 15, AGU, Washington, D.C., 165–236.
- Klemp, J. B. and R. B. Wilhelmson, 1978: The simulation of three-dimensional convective storm dynamics. *J. Atmos. Sci.*, **35**, 1070–1096.
- Law, R. M., P. J. Rayner, L. P. Steele, and I. G. Enting, 2002: Using high temporal frequency data for CO_2 inversions. *Global Biogeochem. Cycles*, **16**, doi:10.1029/2001GB001593.
- 2003: Data and modelling requirements for CO_2 inversions using high-frequency data. *Tellus Ser. B*, **55**, 512–521.
- Lee, X., 1998: On micrometeorological observations of surface-air exchange over tall vegetation. *Agric. For. Meteorol.*, **91**, 39–49.
- Leff, B., N. Ramankutty, and J. A. Foley, 2004: Geographic distribution of major crops across the world. *Global Biogeochem. Cycles*, **18**, GB1009, doi:10.1029/2003GB002108.
- Lin, J. C., C. Gerbig, B. C. Daube, S. C. Wofsy, A. E. Andrews, S. A. Vay, and B. E. Anderson, 2004: An empirical analysis of the spatial variability of atmospheric CO_2 : Implications for inverse analyses and space-borne sensors. *Geophys. Res. Letters*, **31**, L23104, doi:10.1029/2004GL020957.
- Lin, S. J. and R. B. Rood, 1996: Multidimensional flux-form semi-lagrangian transport scheme. *Monthly Weather Review*, **124**, 2046–2070.

- Lokupitiya, E., A. S. Denning, K. Paustian, I. T. Baker, K. Schaefer, S. Verma, T. Meyers, and C. Bernacchi, 2008: Incorporation of crop phenology in the simple biosphere model (sibcrop) to improve land-atmosphere carbon exchanges from croplands. *J. Geophys. Res.*, submitted.
- Lotsch, A., Y. Tian, M. A. Friedl, and R. B. Myneni, 2003: Land cover mapping in support of lai and fpar retrievals from eos-modis and misr: classification methods and sensitivities to errors. *Int. J. Remote Sensing*, **24**, 1997–2016.
- Lu, L., A. S. Denning, M. A. Silva-Dias, P. Silva-Dias, M. Longo, S. R. Freitas, and S. Saatchi, 2005: Mesoscale circulations and atmospheric CO_2 variations in the tapajos region, para, brazil. *J. Geophys. Res.*, **110**, D21102, doi:10.1029/2004JD005757.
- Maddonni, G. A., A. G. Cirilo, and M. E. Otegui, 2006: Row width and maize grain yield. *Agron. J.*, **98**, 1532–1543.
- Malone, S., 2001: Assessment of soybean leaf area for redefining management strategies for leaf-feeding insects, PhD Dissertation, Virginia Tech, Blacksburg, VA, USA, 104 pgs.
- Margolis, H. A., L. B. Flanagan, and B. D. Amiro, 2006: The fluxnet-canada research network: Influence of climate and disturbance on carbon cycling in forests and peatlands. *Agric. For. Meteorol.*, **140**, 268–279.
- Marland, G., T. A. Boden, and R. J. Andres, 2005: Global, regional, and national CO_2 emissions. *Trends: A Compendium of Data on Global Change*, Carbon Dioxide Inf. Anal. Cent., Oak Ridge Natl. Lab, U.S. Dep. of Energy, Oak Ridge, Tenn. (Available at http://cdiac.ornl.gov/trends/emis/em_cont.htm).
- Marland, G. and R. M. Rotty, 1984: Carbon dioxide emissions from fossil fuels: a procedure for estimation and results for 1950-1982. *Tellus Ser. B*, **36**, 232–261.
- Mellor, G. L. and T. Yamada, 1982: Development of a turbulence closure model for geophysical fluid problems. *Rev. Geophys.*, **20**, 851–875.
- Meyers, M. P., R. L. Walko, J. Y. Harrington, and W. R. Cotton, 1997: New rams cloud microphysics parameterization, part ii: The two-moment scheme. *Atmos. Res.*, **45**, 3–39.

- Miller, C. E., D. Crisp, P. L. DeCola, S. C. Olsen, J. T. Randerson, A. M. Michalak, A. Alkhaled, P. R. Anderson, J. Jacob, P. Suntharalingam, D. B. A. Jones, A. S. Denning, M. E. Nicholls, S. C. Doney, S. Pawson, H. Boesch, B. J. Connor, I. Y. Fung, D. O'Brien, R. J. Salawitch, S. P. Sander, B. Sen, P. Tans, G. C. Toon, P. O. Wennberg, S. C. Wofsy, Y. L. Yung, and R. M. Law, 2007: Precision requirements for space-based x_{CO_2} data. *J. Geophys. Res.*, **112**, D10314, doi:10.1029/2006JD007659.
- Miller, J. B., P. P. Tans, J. W. C. White, and T. J. Conway, 2003: The atmospheric signal of terrestrial carbon isotopic discrimination and its implication for partitioning carbon fluxes. *Tellus Ser. B*, **55**, 197–206.
- Monson, R. K., J. P. Sparks, T. N. Rosentiel, L. E. Scott-Denton, T. E. Huxman, P. C. Harley, A. A. Turnipseed, S. P. Burns, B. Backlund, and J. Hu, 2005: Climatic influences on net ecosystem exchange CO_2 exchange during the transition from wintertime carbon source to springtime carbon sink in a high-elevation, subalpine forest. *Oecologia*, **146**, 130–147.
- Mu, Q., F. A. Heinsch, M. Zhao, and S. W. Running, 2007: Development of a global evapotranspiration algorithm based on modis and global meteorology data. *Rem. Sens. Env.*, **111**, 519–536.
- Munger, J. W. and H. W. Loescher, 2006: Guidelines for making eddy covariance flux measurements, FLUXNET measurement guidelines, available on-line at <http://public.ornl.gov/ameriflux/sop.shtml>.
- Myneni, R. B., S. Hoffman, Y. Knyazikhin, J. L. Privette, J. Glassy, Y. Tian, Y. Wang, X. Song, Y. Zhang, G. R. Smith, A. Lotsch, M. Friedl, J. T. Morisette, P. Votava, R. R. Nemani, and S. W. Running, 2002: Global products of vegetation leaf area and fraction absorbed par from year one of modis data. *Rem. Sens. Env.*, **83**, 214–231.
- Nabuurs, G. J., T. Karjalainen, A. Pussinen, M. J. Schelhaas, G. M. J. Mohren, and C. B. Field, 2003: Temporal evaluation of the carbon sink in european forests. *Global Change Biol.*, **9**, 152–160.
- Nicholls, M. E., A. S. Denning, L. Prihodko, P. L. Vidale, I. Baker, K. Davis, and P. Bakwin, 2004: A multiple-scale simulation of variations in atmospheric

- carbon dioxide using a coupled biosphere-atmospheric model. *J. Geophys. Res.*, **109**, D18117, doi:10.1029/2003JD00482.
- NIES, 2006: National institute for environmental studies gosat pamphlet, Greenhouse Gases Obs. Satell. Proj., Cent. for Global Environ. Res., Natl. Inst. for Environ. Stud., Tsukuba, Japan.
- NRC, 1977: Carbon dioxide and climate: a scientific assessment by the national research council, National Academy Press, Washington D.C.
- Ogle, S., K. Davis, A. Andrews, K. Gurney, T. West, R. Cook, T. Parkin, J. Morisette, S. Verma, and S. Wofsy, 2006: Mid-continent intensive campaign of the north american carbon program, Science Plan, prepared by the Mid-Continent Intensive Campaign Task Force.
- Olsen, R. J., S. K. Holladay, R. B. Cook, E. Falge, D. Baldocchi, and L. Gu, 2004: Fluxnet: Database of fluxes, site characteristics, and flux-community information, ORNL/TM-2003/204. Oak Ridge National Laboratory, Oak Ridge, Tennessee. Available on-line at <http://www.fluxnet.ornl.gov>.
- Olsen, S. C. and J. T. Randerson, 2004: Differences between surface and column atmospheric CO_2 and implications for carbon cycle research. *J. Geophys. Res.*, **109**, D02301, doi:10.1029/2003JD003968.
- Overgaard, J., D. Rosbjerg, and M. B. Butts, 2006: Land-surface modeling in hydrological perspective - a review. *Biogeosciences*, **3**, 229–241.
- Pacala, S. W., G. C. Hurtt, D. Baker, P. Peylin, R. A. Houghton, R. A. Birdsey, L. Heath, E. T. Sundquist, R. F. Stallard, P. Ciais, P. Moorcroft, J. P. Caspersen, E. Shevliakova, B. Moore, G. Kohlmaier, E. Holland, M. Gloor, M. E. Harmon, S. M. Fan, J. L. Sarmiento, C. L. Goodale, D. Schimel, and C. B. Field, 2001a: Consistent land- and atmosphere-based u. s. carbon sink estimates. *Science*, **292**, 2316–2319.
- Pacala, S. W., G. C. Hurtt, P. R. Moorcroft, and J. P. Caspersen, 2001b: Carbon storage in the u.s. caused by land use change. *The present and Future of Modeling Global Environmental Change*, Terra Scientific Publishing, Tokyo, Japan, 145–172.

- Pachta, C. J., 2007: Improving irrigated cropping systems on the high plains using crop simulation models, Master of Science Thesis, Kansas State University, Manhattan, KS, USA, 139 pgs.
- Palmer, P. I., D. J. Jacob, D. B. A. Jones, C. L. Heald, R. M. Yantosca, J. A. Logan, G. W. Sachse, and D. G. Streets, 2003: Inverting for emissions of carbon monoxide from asia using aircraft observations over the western pacific. *J. Geophys. Res.*, **108**, 8828, doi:10.1029/2003JD003397.
- Papale, D., M. Reichstein, E. Canfora, M. Aubinet, C. Bernhofer, B. Longdoz, W. Kutsch, S. Rambal, R. Valentini, and D. Yakir, 2006: Towards a more harmonized processing of eddy covariance CO_2 fluxes: Algorithms and uncertainty estimation. *Biogeosciences Discuss.*, **3**, 961–992.
- Parazoo, N. C., A. S. Denning, S. R. Kawa, K. D. Corbin, R. Lokupitiya, and I. T. Baker, 2008: Mechanisms for synoptic transport of CO_2 in the midlatitudes and tropics. *Atmos. Chem. Phys.*, submitted.
- Peters, W., A. R. Jacobson, C. Sweeney, A. E. Andrews, T. J. Conway, K. Masarie, J. B. Miller, L. M. P. Bruhwiler, G. Petron, A. I. Hirsch, D. E. J. Worthy, G. R. van der Werf, J. T. Randerson, P. O. Wennberg, M. C. Krol, and P. P. Tans, 2007: An atmospheric perspective on north american carbon dioxide exchange: Carbontracker. *Proc. Nat. Acad. Sci.*, **104**, 18925–18930.
- Peylin, P., P. J. Rayner, C. Carouge, F. Hourdin, P. Heinrich, and P. Ciais, 2005: Daily CO_2 flux estimates over europe from continuous atmospheric measurements: 1. inverse methodology. *Atmos. Chem. Phys.*, **5**, 3173–3186.
- Philpott, A. W., 2006: Surface fluxes of water, energy, and carbon dioxide as simulated by the simple biosphere model version 3 in the southern great plains of north america, and their effect on the simulated boundary layer hydrology, Master's Thesis, Colorado State University, Fort Collins, CO, USA.
- Pielke, R. A., W. R. Cotton, R. L. Walko, C. J. Tremback, W. A. Lyons, L. D. Grasso, M. E. Nicholls, M. D. Moran, D. A. Wesley, T. J. Lee, and J. H. Copeland, 1992: A comprehensive meteorological modeling system rams. *Meteorol. Atmos. Phys.*, **49**, 69–91.
- Plass, G. N., 1956: The carbon dioxide theory of climatic change. *Tellus Ser. B*, **8**, 140.

- Ponton, S., L. B. Flanagan, K. P. Alstad, B. G. Johnson, K. Morgenstern, N. Kljun, T. A. Black, and A. G. Barr, 2006: Comparison of ecosystem water-use efficiency among douglas-fir forest, aspen forest and grassland using eddy covariance and carbon isotope techniques. *Global Change Biol.*, **12**, 294–310.
- Rayner, P. J., R. M. Law, D. M. O'Brien, T. M. Butler, and A. C. Dilley, 2002: Global observations of the carbon budget: 3. initial assessment of the impact of satellite orbit, scan geometry, and cloud on measuring CO_2 from space. *J. Geophys. Res.*, **107**, 4557, doi:10.1029/2001JD000618.
- Rayner, P. J. and D. M. O'Brien, 2001: The utility of remotely sensed CO_2 concentration data in surface source inversions. *Geophys. Res. Letters*, **28**, 175–178.
- Rayner, P. J., M. Scholze, W. Knorr, T. Kaminski, R. Giering, and H. Widmann, 2005: Two decades of terrestrial carbon fluxes from a carbon cycle data assimilation system (ccdas). *Global Biogeochem. Cycles*, **19**, GB2026, doi:10.1029/2004GB002254.
- Revelle, R. and H. E. Suess, 1957: Carbon dioxide exchange between atmosphere and oceans and the question of an increase in atmospheric CO_2 in the past decades. *Tellus Ser. B*, **9**, 18.
- Ricciuto, D. M., M. P. Butler, K. J. Davis, B. D. Cook, P. S. Bakwin, A. E. Andrews, and R. M. Teclaw, 2007: Causes of interannual variability in ecosystem-atmosphere CO_2 exchange in a northern wisconsin forest using a bayesian synthesis inversion. *Agric. For. Meteorol.*, **148**, 309–327.
- Rodenbeck, C., S. Houweling, M. Gloor, and M. Heimann, 2003: CO_2 flux history 1982-2001 inferred from atmospheric data using a global inversion of atmospheric transport. *Atmos. Chem. Phys.*, **3**, 1919–1964.
- Russell, J. L. and J. M. Wallace, 2004: Annual carbon dioxide drawdown and the northern annular mode. *Global Biogeochem. Cycles*, **18**, GB1012, doi:10.1029/2003GB002044.
- Sacks, W. J., D. S. Schimel, R. K. Monson, and B. H. Braswell, 2006: Model-data synthesis of diurnal and seasonal CO_2 fluxes of niwot ridge, colorado. *Global Change Biol.*, **12**, 240–259.

- Saleska, S. R., S. D. Miller, D. M. Matross, M. L. Goulden, S. C. Wofsy, H. R. da Rocha, P. B. de Camargo, P. Crill, B. C. Daube, H. C. de Freitas, L. Hutyyra, M. Keller, V. Kirchhoff, M. Menton, J. W. Munger, E. H. Pyle, A. H. Rice, and H. Silva, 2003: Carbon in amazon forests: Unexpected seasonal fluxes and disturbance-induced losses. *Science*, **302**, 1554–1557.
- Sarmiento, J. L., 1993: Atmospheric CO_2 stalled. *Nature*, **365**, 697–698.
- Sarmiento, J. L. and N. Gruber, 2002: Sinks for anthropogenic carbon. *Physics Today*, **8**, 30–36.
- Schuh, A. E., A. S. Denning, M. Uliasz, and K. D. Corbin, 2008: Seeing the forest through the trees: recovering large scale carbon flux biases in the midst of small scale variability. *Geophys. Res. Letters*, In Preparation.
- Sellers, P. J., M. D. Heiser, and F. G. Hall, 1992: Relations between surface conductance and spectral vegetation indices at intermediate length scales. *J. Geophys. Res.*, **97**, 19033–19059.
- Sellers, P. J., S. O. Los, C. J. Tucker, C. O. Justice, D. A. Dazlich, G. J. Collatz, and D. A. Randall, 1996a: A revised land surface parameterization (sib2) for atmospheric gcms. part ii: The generation of global fields of terrestrial biophysical parameters from satellite data. *J. Climate*, **9**, 706–737.
- Sellers, P. J., D. A. Randall, G. J. Collatz, J. A. Berry, C. B. Field, D. A. Dazlich, C. Zhang, G. D. Collelo, and L. L. Bounoua, 1996b: A revised land surface parameterization (sib2) for atmospheric gcms. part i: Model formulation. *J. Climate*, **9**, 676–705.
- Siegenthaler, U. and H. Oeschger, 1978: Predicting future atmospheric carbon dioxide levels. *Science*, **199**, 388–398.
- Sims, P. J. and J. A. Bradford, 2001: Carbon dioxide fluxes in a southern plains prairie. *Agric. For. Meteorol.*, **109**, 117–134.
- Smagorinsky, J., 1963: General circulation experiments with the primitive equations. part i: The basic experiment. *Monthly Weather Review*, **91**, 99–164.
- Spivakovsky, C. M., J. A. Logan, S. A. Montzka, Y. J. Balkanski, M. Foreman-Fowler, D. B. A. Jones, L. W. Horowitz, A. C. Fusco, C. A. M. Brenninkmeijer,

- M. J. Prather, S. C. Wofsy, and M. B. McElroy, 2000: Three-dimensional climatological distribution of tropospheric oh: Update and evaluation. *J. Geophys. Res.*, **105**, 8931–8980.
- Steele, S. J., S. T. Gower, J. G. Vogel, and J. M. Norman, 1997: Root mass, net primary production and turnover in aspen, jack pine and black spruce forests in saskatchewan and manitoba, canada. *Tree Physiol.*, **17**, 577–587.
- Stephens, B. B., K. R. Gurney, P. P. Tans, C. Sweeney, W. Peters, L. Bruhwiler, P. Ciais, M. Ramonet, P. Bousquet, T. Nakazawa, S. Aoki, T. Machida, G. Inoue, N. Vinnichenko, J. Lloyd, A. Jordan, M. Heimann, O. Shibistova, R. L. Langenfelds, L. P. Steele, R. J. Francey, and A. S. Denning, 2007: Weak northern and strong tropical land carbon uptake from vertical profiles of atmospheric CO_2 . *Science*, **22**, 1732–1735, doi:10.1126/science.1137004.
- Stephens, G. L., D. G. Vane, R. J. Boain, G. G. Mace, K. Sassen, Z. Wang, A. J. Illingworth, E. J. O'Connor, W. B. Rossow, S. L. Durden, S. D. Miller, R. T. Austin, A. Benedetti, and C. Mitrescu, 2002: The cloudsat mission and the a-train. *Bull. Amer. Meteor. Soc.*, **83**, 1771–1790.
- Still, C. J., J. A. Berry, G. J. Collatz, and R. S. DeFries, 2003: Global distribution of C_3 and C_4 vegetation: Carbon cycle implications. *Global Biogeochem. Cycles*, **17**, doi:10.1029/2001GB001807.
- Stoy, P. C., G. G. Katul, M. B. S. Siqueira, J. Y. Juang, H. R. McCarthy, H. S. Kim, A. C. Oishi, and R. Oren, 2005: Variability in net ecosystem exchange from hourly to inter-annual time scales at adjacent pine and hardwood forests: A wavelet analysis. *Tree Physiol.*, **25**, 887–902.
- Stoy, P. C., S. Palmroth, A. C. Oishi, M. B. S. Siqueira, J. Y. Juang, K. A. Novick, E. J. Ward, G. G. Katul, and R. Oren, 2007: Are ecosystem carbon inputs and outputs coupled at short time scales? a case study from adjacent pine and hardwood forests using impulse-response analysis. *Plant Cell Environ.*, **30**, 700–710.
- Suntharalingam, P., D. J. Jacob, P. I. Palmer, J. A. Logan, R. M. Yantosca, Y. Xiao, M. J. Evans, D. G. Streets, S. L. Vay, and G. W. Sachse, 2004: Improved quantifications of chinese carbon fluxes using CO_2/CO correlations in asian outflow. *J. Geophys. Res.*, **109**, D18S18, doi:10.1029/2003JD004362.

- Suyker, A. E., S. B. Verma, G. G. Burba, and T. J. Arkebauer, 2005: Gross primary production and ecosystem respiration of irrigated maize and irrigated soybean during a growing season. *Agric. For. Meteorol.*, **131**, 180–190.
- Syed, K. H., L. B. Flanagan, P. J. Carlson, A. J. Glenn, and K. E. V. Gaalen, 2006: Environmental control of net ecosystem CO_2 exchange in a treed, moderately rich fen in northern Alberta. *Agric. For. Meteorol.*, **140**, 97–114.
- Takahashi, T., S. C. Sutherland, C. Sweeney, A. Poisson, N. Metzl, B. Tillbrook, N. Bates, R. Wanninkhof, R. A. Feely, C. Sabine, J. Olafsson, and Y. Nojiri, 2002: Global sea-air CO_2 flux based on climatological surface ocean pCO_2 , and seasonal, biological, and temperature effects. *Deep Sea Res., Part II*, **49**, 1601–1622.
- Tans, P. P. and et. al., 1996: Carbon cycle (group report), climate monitoring and diagnostics laboratory, no. 23, summary report 1994-1995, D. J. Hoffman, J. T. Peterson and R. M. Rosson, eds, US Department of Commerce, Boulder, Colorado.
- Tans, P. P., I. Y. Fung, and T. Takahashi, 1990: Observational constraints on the global atmospheric CO_2 budget. *Science*, **247**, 1431–1438.
- Taylor, K. E., 2001: Summarizing multiple aspects of model performance in a single diagram. *J. Geophys. Res.*, **106**, 7183–7192.
- Tolk, L. F., A. G. C. A. Meesters, A. J. Dolman, and W. Peters, 2008: Modelling representation errors of atmospheric CO_2 concentrations at a regional scale. *Atmos. Chem. Phys. Dis.*, **8**, 3287–3312.
- Trabalka, J. R., 1985: Atmospheric carbon dioxide and the global carbon cycle, United State Department of Energy Report DOE/ER-0239, Washington D.C., USA.
- Turner, D. P., M. Zhao, S. W. Running, S. C. Wofsy, S. Urbanski, A. L. Dunn, J. W. Munger, W. D. Ritts, W. B. Cohen, and S. T. Gower, 2003: Scaling gross primary production (gpp) over boreal and deciduous forest landscapes in support of modis gpp product validation. *Rem. Sens. Env.*, **88**, 256–270.
- U, K. T. P., M. Falk, T. H. Suchanek, S. L. Ustin, J. Q. Chen, Y. S. Park, W. E. Winner, S. C. Thomas, T. C. Hsiao, R. H. Shaw, T. S. King, R. D. Pyles,

- M. Schroeder, and A. A. Matista, 2004: Carbon dioxide exchange between an old growth forest and the atmosphere. *Ecosystems*, **7**, 513–524.
- UN-ECE/FAO, 2000: Forest resources of europe, cis, north america, australia, japan and new zealand. *UN-ECE/FAO contribution to the global forest resources assessment 2000*, United Nations, New York and Geneva, 445 p.
- van der Molen, M. K. and A. J. Dolman, 2007: Regional carbon fluxes and the effect of topography on the variability of atmospheric CO_2 . *J. Geophys. Res.*, **112**, (D01104), doi:10.1029/2006JD007649.
- van der Werf, G. R., J. T. Randerson, L. Giglio, G. J. Collatz, and P. S. Kasibhatla, 2006: Interannual variability in global biomass burning emissions from 1997–2004. *Atmos. Chem. Phys. Dis.*, **6**, 3175–3226. SRef-ID: 1680-7375/acpd/2006-6-3175. Available on-line from <http://www.copernicus.org/EGU/acp/acpd/6/3175/acpd-6-3175.htm>.
- Verma, S. B., A. Dobermann, K. G. Cassmann, D. T. Walters, J. M. Knops, T. J. Arkebauer, A. E. Suyker, G. C. Burba, B. Amos, and H. Yang, 2005: Annual carbon dioxide exchange in irrigated and rainfed maize-based agroecosystems. *Agric. For. Meteorol.*, **131**, 77–96.
- Vidale, P. L. and R. Stockli, 2005: Prognostic canopy air space solutions for land surface exchanges. *Theor. Appl. Climatol.*, **80**, 245–257.
- Walko, R. L., W. R. Cotton, M. P. Meyers, and J. Y. Harrington, 1995: New rams cloud microphysics parameterization: Part i. the single moment scheme. *Atmos. Res.*, **38**, 29–62.
- Walko, R. L. and C. J. Tremback, 2002: 2002: Rams version 5.0 model input namelist parameters.
- Wang, F., C. W. Fraisse, N. R. Kitchen, and K. A. Sudduth, 2003: Site-specific evaluation of the cropgro-soybean model on missouri claypan soils. *Ag. Sys.*, **76**, 985–1005.
- Wang, J. W., A. S. Denning, L. Lu, I. T. Baker, K. D. Corbin, and K. J. Davis, 2007: Observations and simulations of synoptic, regional, and local variations in atmospheric CO_2 . *J. Geophys. Res.*, **112**, D04108, doi:10.1029/2006JD007410.

- Washenfelder, R. A., G. C. Toon, J. F. Blavier, Z. Yang, N. T. Allen, P. O. Wennberg, S. A. Vay, D. M. Matross, and B. C. Daube, 2006: Carbon dioxide column abundances at the wisconsin tall tower site. *J. Geophys. Res.*, **111**, D22305, doi:10.1029/2006JD007154.
- Williams, M. M. and J. L. Lindquist, 2007: Influence of planting date and weed interference on sweet corn growth and development. *Agron. J.*, **99**, 1066–1072.
- Wofsy, S. C., M. L. Goulden, J. W. Munger, S. M. Fan, P. S. Bakwin, B. C. Daube, S. L. Bassow, and F. A. Bazzaz, 1993: Net exchange of CO₂ in a midlatitude forest. *Science*, **260**, 1314–1317.
- Wofsy, S. C. and R. C. Harriss, 2002: The north american carbon program (nacp), U. S. Global Change Res. Program, Washington, D. C.
- Zhao, C., P. S. Bakwin, and P. P. Tans, 1997: A design for unattended monitoring of trace gases on a tall tower. *J. Atmos. Ocean. Tech.*, **14**, 1139–1145.
- Zhao, M., F. A. Heinsch, R. R. Nemani, and S. W. Running, 2005: Improvements of the modis terrestrial gross and net primary production global data set. *Rem. Sens. Env.*, **95**, 164–176.
- Zupanski, D., A. S. Denning, M. Uliasz, A. E. Schuh, P. J. Rayner, W. Peters, and K. D. Corbin, 2007: Carbon flux bias estimation employing maximum likelihood ensemble filter (mlef). *J. Geophys. Res.*, **112**, doi:10.1029/2006JD008371.